12-2008

Mechanical Behavior of a Ni-based Crystalline and a Zr-based Amorphous Materials Subjected to Surface Severe Plastic Deformation

Jiawan Tian
University of Tennessee - Knoxville

To the Graduate Council:

I am submitting herewith a dissertation written by Jiawan Tian entitled "Mechanical Behavior of a Ni-based Crystalline and a Zr-based Amorphous Materials Subjected to Surface Severe Plastic Deformation." I have examined the final electronic copy of this dissertation for form and content and recommend that it be accepted in partial fulfillment of the requirements for the degree of Doctor of Philosophy, with a major in Materials Science and Engineering.

Peter K. Liaw, Major Professor

We have read this dissertation and recommend its acceptance:

Yanfei Gao, Hahn Choo, Hamparsum Bozdogan

Accepted for the Council:
Carolyn R. Hodges

Vice Provost and Dean of the Graduate School

(Original signatures are on file with official student records.)

To the Graduate Council:

I am submitting herewith a dissertation written by Jiawan Tian entitled "Mechanical Behavior of a Ni-based Crystalline and a Zr-based Amorphous Materials Subjected to Surface Severe Plastic Deformation". I have examined the final electronic copy of this dissertation for form and content and recommend that it be accepted in partial fulfillment of the requirements for the degree of Doctor of Philosophy, with a major in Material Science and Engineering.

Peter K. Liaw
Major Professor

We have read this dissertation
and recommend its acceptance:

Yanfei Gao

Hahn Choo

Hamparsum Bozdogan

Accepted for the Council:

Carolyn R. Hodges

Vice Provost and Dean of the Graduate School

(Original signatures are on file with official student records.)

MECHANICAL BEHAVIOR OF A Ni-BASED CRYSTALLINE AND A Zr-BASED AMORPHOUS MATERIALS SUBJECTED TO SURFACE SEVERE PLASTIC DEFORMATION

A Dissertation Presented for the
Doctor of Philosophy Degree
The University of Tennessee, Knoxville

Jiawan Tian
December 2008

Dedication

$\cdots$ dedicated to my dear wife, parents, and brothers

Acknowledgments

First and foremost, I would like to thank my advisor, Dr. Peter K. Liaw. His generous supports and essential guidance throughout my studies have made it possible for me to finish my PhD study at the University of Tennessee. I thank him for providing me a friendly environment where I could develop my capabilities in research, communication, and presentation. I would also like to thank Dr. Leon L. Shaw from the University of Connecticut for his great help with my research over the years. His unreserved advice, counsel, and instruction are of great importance to me, and I will never be grateful to him too much. I would further like to thank the other members of my committee: Dr. Yanfei Gao, Dr. Hahn Choo, and Dr. Hamparsum Bozdogan. I greatly appreciate their kind agreement to be on my Doctoral Committee, as well as the precious time they spent on my proposal and dissertation.

I am grateful to those people who have kindly provided the materials for my experiments. Dr. Dwaine L. Klarstrom from the Haynes International, Inc. has provided all the C-2000 Superalloy samples, and gave instructive advice and suggestions on my research. Dr. Yoshihiko Yokoyama from Tohoku University has sent me many high-quality bulk-metallic-glass samples. Without their willingness and generousness, my research work would be an impossible mission. Mr. Douglas E. Fielden in the UT mechanical shop is always a great help whenever sample-cutting is needed. His expertise in the equipment design and machining techniques has been the accelerator in making progress in this project.

I am also indebted to those who have helped me on my experiments. I thank Mr. Jones Greg and Dr. Xiaoyun Lin for helping me on the operation of Scanning-Electron Microscopy and X-ray diffractometer. I am also thankful to Dr. Joseph E. Spruiell for his kind instruction on the X-ray technique. Special thanks to our administration specialists, Ms. Sandra P. Maples and Carla Lawrence, accounting specialist, Mr. W. Frank Holiway, and administration support assistant, Mr. Randy D. Stooksbury.

Within this large group, I owe many thanks to my team members and also friends, Dr. Wenhui Jiang, Dr. Yandong Wang, Dr. Bing Yang, Dr. Yulin Lu, Dr. Migri Stoica, Dr. Hongbo Tian, Dr. Gongyao Wang, Dr. Guojiang Fan, Dr. Cang Fan, Dr. Kaixiang Tao, Dr. Yinan Sun, Dr. Lan Huang, Dr. Rajanah Steward, Dr. Brandice Green, Dr. Michael Benson, Ms. Dongchun Qiao, Ms. Shenyan Huang, Ms. Li Li, Ms. Lu Huang, Mr. Wei Yuan, Mr. Fengxiao Liu, Mr. Liang Wu, Mr. Feng Jiang, Mr. Zhengke Teng, Mr. E-wen Huang, Mr. Matthew Freels, Mr. Sooyel Lee, Ms. Carol Winn, and other group members. Thank your guys for your help, and for the great time we enjoyed together at UT.

Acknowledgements are also due to the financial support for this research by the National Science Foundation with the program on "the Novel Surface Nanocrystallization and Hardening (SNH) Process for Improved Fatigue and Wear Resistance" under Grant No. DMR-0207729, the NSF Combined Research-Curriculum Development (CRCD) Program, under EEC-9527527 and EEC-0203415, the NSF Integrative Graduate Education and Research Training (IGERT) Program under DGE-9987548, and Haynes International, Inc., with Ms. M. Poats, Dr. C.J. Van Hartesveldt, Dr. P.W. Jennings, Dr. L.S. Goldberg, and Dr. D.L. Klarstrom as contract monitors, respectively.

Last but not the least, I am deeply indebted to my family. My parents, Chuanbiao Tian and Huilan Qiu, both over sixty-year old, haven't seen me for more than four years because of my PhD study. However, they never complain for that but rather continuously encourage me to concentrate on my study. My wife, Lefei Liu, who is always my supporter and source of strength. My parents-in-law, Huashou Liu and Heying Chen, who care for us all the time, and my brothers, Jiacai Tian and Jiachang Tian, who unreservedly supported me both financially and spiritually during all my hard times.

Abstract

A surface-treatment process, surface-severe-plastic deformation (S^2PD), is developed and applied on both crystalline and amorphous materials to introduce the plastic deformation in the near-surface layer. A S^2PD-processed crystalline component is expected to have enhanced fatigue properties because the refined grains in the near-surface layer and the coarse grains in the interior have good resistance to the crack initiation and propagation, respectively.

The near-surface structures of the processed specimens were characterized by means of the optical microscopy, scanning-electron microscopy (SEM), X-ray diffraction (XRD), and transmission-electron microscopy (TEM). Mechanical properties, such as the microhardness, yield strength, and four-point-bend fatigue, were systematically investigated. It is shown that the S^2PD process has the capability of simultaneously creating (a) a work-hardened surface layer, (b) a nanocrystalline (nc) surface layer, (c) a surface region with compressive-residual stresses, and (d) a grain-size gradient with a nc surface and a coarse-grained interior for the polycrystalline superalloy. Improved fatigue properties were found after the process. However, excessive treatments deteriorate the fatigue properties, and the possible reasons are discussed.

For the amorphous material, thermal properties of the processed near-surface layer were characterized by means of the differential-scanning calorimetry (DSC). Effects of the treatment on the microhardness were studied by the nanoindentation. After the treatment, the plastic-flow deformation in the unconstrained sample edge was observed. In the sub-surface layer, the impact-induced shear-band operations generate the extrusion and intrusion marks on the side face. DSC shows that the free volumes of the deformed BMG have increased, and possible crystallization may occur during the process. XRD and high-energy synchrotron diffraction techniques were used to inspect the possible crystalline phase. A nanoindentation test shows that on the side surface, the hardness increases and, then, decreases with the distance from the processed surface. Four-point-bending-fatigue behavior has been studied and related to the modified surface structure and the compressive-residual stress induced by the process.

Table of Contents

List of Tables

List of Figures

CHAPTER 1

Introduction

1.1 Background of Fatigue

The fatigue life, N_f, is defined by the American Society for Testing and Materials (ASTM) as the number of stress cycles of a specified character that a specimen sustains before the failure of a specified nature occurs [1]. When a cyclic loading, with the stress amplitude much lower than the yield strength of the material, is applied on a component, the damage can be accumulated gradually and finally causes the catastrophic failure, which is referred as fatigue fracture. The fatigue fracture can usually be divided into two consecutive processes, crack initiation (or nucleation) and crack growth (or propagation). Both of them are closely related to the microstructural characteristics of the component, such as defects, grain sizes, strength particles, etc.

The fatigue fracture of engineering components has been found as early as in 1837 by Wilhelm Albert, though the earliest systematic fatigue studies were performed by Sir William Fairbairn and August Wöhler in 1860 [2, 3]. Wöhler stated the stress amplitude to be the most important parameter for the fatigue life. When the stress decreases to a certain level, the fatigue life tends to approach the infinity. The maximum stress under which the material will not fail regardless of the fatigue cycles is usually referred as the fatigue strength. In high-cycle fatigue situations (where the fatigue life is between 10^3 to 10^8 cycles), fatigue behavior is usually characterized by an S-N curve (i.e., stress vs. number of cycles to failure), which is also known as a Wöhler curve. In this curve, the abscissa is the number of cycles to failure on a logarithmic scale, and the ordinate is the stress. In many cases, an S-N curve can be analyzed using a linear-regression technique because of the probabilistic nature of fatigue (i.e., fatigue data are usually quite scattered even in controlled environments).

Two of the most important empirical equations, which are frequently used to describe the fatigue behavior of a component, are the Miner's rule and the Paris' law. A fatigue experiment is often conducted in a constant loading or constant strain condition, both of which belong to a simple loading mode. However, in reality, the loading mode could be complex, i.e., the load can be a function of the time rather than a constant. In this situation, the Miner's rule, also called the Palmgren-Miner linear-damage hypothesis, states that where there are k different stress magnitudes, each contributing n_i cycles, then if N_i is the number of cycles to failure of the corresponding stress magnitude, failure occurs when:

$$\sum_{i=1}^{k} \frac{n_i}{N_i} = C \tag{1.1}$$

C is experimentally found to be between 0.7 and 2.2. Usually for design purposes, C is assumed to be 1. This equation can be thought of as assessing what proportion of the life is consumed by the stress at each magnitude, then forming a linear combination of their aggregate. It can also be used to estimate the fatigue life of a component when various stress magnitudes are applied.

Different from the Miner's rule, the Paris' law concerns only the fatigue-crack-growth rate rather than the fatigue life. More specifically, it relates the crack-growth rate, da/dN, to the stress-intensity factor and material constants. i.e.,

$$\frac{da}{dN} = c(\Delta K)^m \tag{1.2}$$

where m is an empirical material constant, $c \approx \sigma_U K_{IC}$ is a function of the ultimate tensile stress, σ_U, and the fracture toughness, K_{IC}. ΔK is the stress-intensity-factor range and is a function of the cyclic loading, crack length, and sample geometry [4, 5].

Although the stress level is the most intuitionistic parameter in affecting the fatigue life, many other factors actually play more realistic roles when the purpose is to improve the fatigue performance under a desired stress level. For example, surface notches may easily cause stress concentration and, thus, crack initiation. Therefore, a notched sample usually has a lower fatigue strength than an unnotched one. It

can be deduced from this result that the fatigue property should be sensitive to the surface roughness. A polished sample may have a higher fatigue strength than an unpolished one, which actually has been confirmed by the experiments [6].

Other factors, such as the material type, internal defects, residual stress, grain size, environment, temperature, etc., also affect the crack initiation and crack propagation in different ways, and each of them has been systematically discussed in many fatigue books [4, 7]. Among those parameters, three of the most important ones are the yield strength (or hardness), the surface quality (roughness, defects, etc.), and the residual stresses. So far, many different processes have been developed to optimize those factors so as to improve the fatigue property of the component.

The yield strength is affected not only by the material type, but also by the microstructures, such as the grain size. The Hall-Petch equation described the relation between the yield strength and the grain size as shown below:

$$\sigma_y = \sigma_0 + \frac{k_y}{\sqrt{d}} \tag{1.3}$$

where k_y is the strengthening coefficient (a constant unique to each material), σ_0 is a material constant for the starting stress for the dislocation movement (or the resistance of the lattice to the dislocation motion), d is the grain diameter, and σ_y is the yield stress. Since crack initiation usually begins with dislocation movements, any strength mechanism, which can inhibit the dislocation movement, may also be helpful to improve the fatigue strength. In this study, we are trying to refine the grain size in the near-surface layer of the sample to improve its fatigue resistance.

Since any surface defects could become the potential sources of crack-initiation sites because of the stress-concentration effect, the surface quality is very important to fatigue properties in a high-cycle-fatigue range. Because in this range, the fatigue crack almost always initiates from the sample surface. Actually, this trend is true even for a well-polished sample, since the surface itself sometimes is also considered as a defect.

Residual stresses affect the fatigue performance in a quite straightforward way. That is, the compressive-residual stress could counteract part of the exerted loading stress so as to increase the fatigue strength, while the tensile-residual stress will do the contrary. A component with residual stresses can be considered as a pre-deformed material. When the applied stress is on the same direction of the pre-deformation (a tensile-residual-stress situation), the material is easy to deform, and the component has a low strength. When the applied stress is on the reversed direction of the pre-deformation (a compressive-residual-stress situation), the material is difficult to deform, and the component has a high strength [7].

1.2 Improvement of Fatigue Behavior

As stated in the first section, there are many different ways to improve the fatigue performance of a component. Improving the yield strength by a grain-refinement process seems to be a simple and effective method. A nano-structured material, however, does not necessarily have a good fatigue performance. Because the fatigue properties are affected by both the yield strength and the grain size of the materials. Though high yield strength enhances the fatigue-crack-initiation threshold, the small grain size may accerelate the crack-growth rate.

To be more specific, the fatigue strength is not a monotonic function of the grain size. It is known that small grains could effectively increase the yield strength so as to enhance the fatigue-crack-initiation threshold. Meanwhile, a small grain size has an adverse effect on the resistance to the fatigue-crack growth, since cracks can easily propagate along grain boundaries. On the contrary, coarse grains may deflect the propagation paths of fatigue cracks by grain boundaries, thus introducing crack closure and decreasing the rate of crack growth. However, coarse grains are not effective in preventing the initiation of the fatigue crack [8].

Figure 1.1 shows a schematic illustration that crack propagation can be deflected by large grains but not by small ones. Because of the co-existed competitive effects, it is not surprising to found that in the literature there are no good agreements

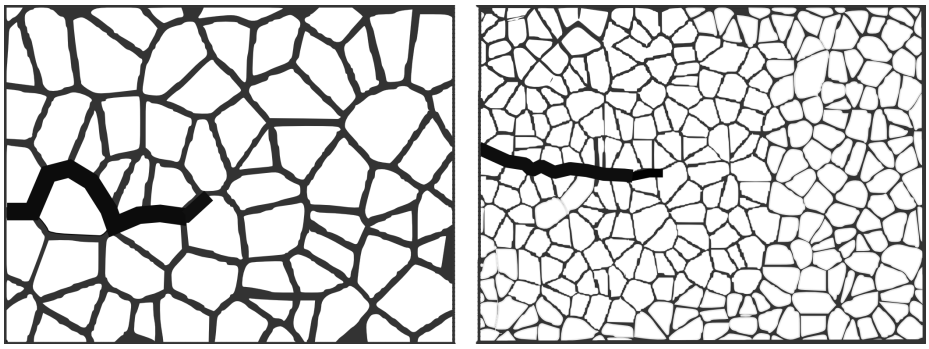

Figure 1.1: A fatigue crack propagates along the grain boundaries. The figure shows that coarse grains can deflect the propagation path more effectively than fine grains do.

on the relationships between the fatigue properties and grain sizes. For example, in Vinogradov et al.'s [9] investigation of an ultra-fine grained titanium obtained by the severe-plastic deformation through equal-channel-angular pressing (ECAP), it was shown that when the grain size changed from 100, 32, to 9 μm, the fatigue strength pronouncedly increased accordingly. However, in the ultra-fine crystalline 6061 Al alloys subjected to the equal-channel-angular pressing, though significant improvement in the fatigue strength was found after one ECAP pass, no improvement was observed at all after further grain refinement [10].

Theoretical explanations for the effects of grain sizes on crack growth can be found in Eq. (1.2), where the grain size hides its effects within the material constant, c (which is a function of the ultimate tensile stress). Large grains may deflect the crack-propagation path and, thus, prolong the crack-growth time. When the crack initiates along a slip band, the effect of grain size can be revealed by the following equation [11]:

$$N_f = \frac{8\mu W_s}{(\Delta\tau - 2k)^2 \pi d} \tag{1.4}$$

where N_f is the number of cycles to failure (failure can be defined as the final fricture or crack growing to a certain crack length), μ is the shear modulus, W_s is the specific fracture energy per unit area along the slip band, $\Delta\tau$ is the shear-stress range, k is the fraction stress of dislocation, and d is the grain size. From this equation, it can be clearly seen that small grain sizes can prolong the dislocation dipole-accumulation

process, i.e., the crack-initiation process, so as to improve the fatigue life of a component.

Based upon the above-mentioned information, it is believed that a component with a nano-grained surface and a coarse-grained interior should have a good fatigue resistance, because (1) in the surface, the small grains can effectively resist the fatigue-crack initiation, and (2) in the interior, the large grains can deflect the fatigue-crack-propagation path and, thus, increase the fatigue life [12].

Introducing compressive-residual stresses and improving the surface quality are also typical methods, which can be used to enhance the fatigue strength. Shot peening is an excellent and mature process in industry, which can combine these two effects together and remarkably improve the fatigue property of engineer component [12]. Shot peening is a cold-working process that hardens the surface of a metallic component by bombarding it with a stream of small particles called shots. The consequences of a shot-peening process include the roughening of the surface, the increased near-surface dislocation density (strain hardening), and the development of a characteristic profile of residual stresses. For the casted component, the bombardment of shots may also eliminate some of the surface casting defects so as to decrease the stress-concentration effect.

A surface-severe-plastic-deformation (S^2PD) process is a recently-developed process, which is based upon the shot-peening process but using balls with much higher kinetic energy to bombard the sample surface. The most predominant advantage of a S^2PD process lies in the fact that it not only keeps the advantages of the shot-peening process, but introduces a nano-structured near-surface layer at the same time. Specifically, the S^2PD process has been shown to be capable of creating simultaneously (a) a work-hardened surface layer, (b) a nanocrystalline (nc) surface layer, (c) a surface region with compressive residual stresses, and (d) a grain-size gradient with a nc surface and a coarse-grained interior. Engineering components possessing these features are expected to have superior fatigue resistance because the nanograins

at the surface will suppress the formation of fatigue cracks, and the coarse-grained interior will retard the fatigue-crack growth.

The overall goal of this dissertation is to develop a fundamental understanding of the microstructural evolution and the mechanisms controlling the fatigue behavior of a Ni-based polycrystalline superalloy after a S^2PD process, and apply the process on a Zr-based bulk-metallic-glass component.

1.3 Surface Treatment on Bulk-Metallic Glass

Unlike conventional crystalline materials, metallic glasses have a disordered atomic-scale structure and are usually produced directly from the liquid state during cooling without crystal nucleations. In recently years, a number of alloys with critical cooling rates low enough to allow the formation of amorphous structures in thick layers (over 1 mm) had been produced, which are known as bulk-metallic glasses (BMG). With no crystal defects, the BMG materials have some unique properties, such as high strength (twice of that of stainless steels, but lighter), high hardness (for surface coating), high toughness (more fracture resistant than ceramics), and great elasticity [13].

Though the BMG materials have been shown to have good overall mechanical properties, one of the greatest problems, which inhibit the wide applications of BMGs, is their low ductility compared with the conventional metals. Since the potential application of BMG is so closely dependent on their plasticity that extensive research has been conducted to investigate their plastic-deformation performance at room temperature. Some popular experimental setups, such as the indentation, compression, bending, etc., are widely used to exert different loading modes on the amorphous material to generate plastic deformation. According to the results of those studies, it has been established that the inhomogeneous shear-band operation is the characteristic of the deformation in the BMGs at room temperature [14, 15].

In order to improve the ductility of BMGs, both extrinsic and intrinsic methods have been proposed to suppress the propagation of shear bands in recent years.

An example of the former method is to optimize the geometry of the sample so that shear bands would not propagate to the free surface [15, 16], while that of the latter is to introduce reinforcements into the material so as to retard the propagation of the shear band [17, 18]. However, the continuous emergence of papers regarding the plastic deformation of BMGs indicates that this issue is far from clear.

Partially due to the fact that BMGs are easy to fracture before enough plastic deformation could be accumulated within the material, there are few studies on the effects of the plastic deformation on the mechanical properties of BMGs. As seen in the previous section of this chapter, it seems that shot peening is an effective method to introduce plastic deformation into a crystalline specimen. It is of great interest to study the effects of this surface-treatment process on the microstructures and mechanical properties, such as the hardness, ductility, and fatigue strength, of an amorphous material.

1.4 Summary

Improving the fatigue performance of an engineering component through a shot-peening process has been widely used in industry. With the development of nanotechnology, nano-structured materials have shown super global mechanical properties. In order to utilize the advanced properties of the nanomaterials to improve the fatigue performance of a component, a modified shot-peening process, called a surface-severe-plastic-deformation (S^2PD) process, will be developed in this work. Using the S^2PD process, a nano-structured near-surface layer will be introduced into the component, while in the interior of the component, the grain size remains coarse. A component processed with the S^2PD process is expected to have good fatigue resistance.

The surface treatment on the BMG materials is a relative new field in the BMG research. In this study, we are trying to introduce plastic deformation in the surface of a Zr-based BMG by the S^2PD process. After the treatment, both microstructures and the mechanical properties of the materials will be investigated. We

are especially interested in the mechanism of the deformation-induced microstructure changes, such as the crystallization. The fatigue behavior of the processed samples will be studied as well.

CHAPTER 2

Literature Review

2.1 Shot Peening

2.1.1 Overview

Shot peening, originally called "shot blasting" by Zimmerli and later termed as "shot peening" by Almen, is a process, which is used to introduce compressive residual stresses in the near-surface layer of metal components [19]. It is used mainly to increase the resistance of metal parts against fatigue, fretting fatigue, stress corrosion, and corrosion fatigue. It is also used to produce a desired surface topography, to harden surfaces, to close pores, and to test bonds [19].

The application of the procedure of shot peening was first mentioned in 1924 [20]. In 1929, Röchling Stahlwerke received a patent on the procedure of shot peening. However, at that time, it was already used at the automobile factories in the USA [20]. Presently, a typical shot-peening process uses small spherical media called shots (which could be cast-steel shots, cut-wire shots, glass, or ceramic beads) to create small dents in the surface, which are very beneficial in preventing the formation of fatigue cracks. The area below each dent called the plastic zone, typically only 0.5-mm deep, is highly compressed, and this action tends to keep cracks from opening in the surface.

Shot peening is now widely used in automotive and aerospace industries to improve the fatigue strength or working life for many components, including but not limited to transmission gears, axles, turbine-engine disks, and springs, etc. While many of the approaches have been highly empirical and dependent upon large databases,

some optimization procedures based upon a scientific understanding of the process parameters have also been developed [7]. For example, Rodopoulos et al. [21] proposed a fatigue optimisation methodology where the residual-stress profiles, work-hardening profiles, and the surface roughness were treated as the major parameters, which control the final fatigue-life improvements. It is also pointed out that work hardening is expected to increase the flow resistance of the material and, thus, reduce the crack-tip plasticity, while the residual stresses can act as (a) mean-stress modulators – in the case of the onset of crack propagation or (b) closure stresses in the case of crack growth. However, the effect of the surface roughness on the fatigue properties of a component varies with the mechanical properties and the microstructure of the material [21, 22].

In this section, the main features, i.e., the residual-stress profile, work-hardening profile, and the surface roughness induced by a shot-peening process will be reviewed, and the effects of each feature on the fatigue properties will be demonstrated as well.

2.1.2 Residual stresses

Origin of residual stresses

Residual stresses are usually defined as stress fields that exist in the absence of any external loads. Any mechanical processes, which can cause deformation, may lead to residual stresses, and unbalanced thermal deformation may also cause residual stresses. Therefore, the state of a residual stress depends on both the prior processes it has undergone, and the material properties that relate the current mechanical process/environment to deformation [23].

Residual stresses originate from misfits between different regions within a component. In the shot-peening case, these misfits span large distances, and this type of residual stresses is called macrostresses, or type I residual stresses. This is in contrast to residual stresses that vary over the grain scale (type II or intergranular stresses) or the atomic scale (type III). In these cases, the misfitting regions span

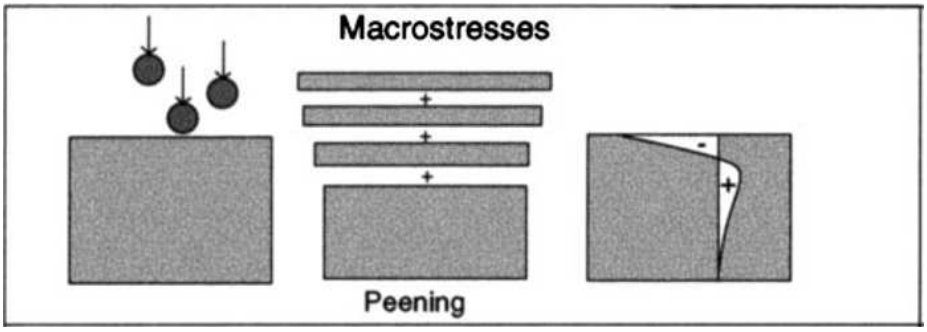

Figure 2.1: Residual stresses arise from misfits between different regions during a shot peening process [24].

microscopic or submicroscopic dimensions [24]. Because type II or type III stresses almost alway exists in polycrystalline materials due to the different grain orientation, in this dissertation, residual stresses always refer to macro-residual stresses except for otherwise explanation.

The formation of compressive-residual stresses during a shot-peening process can be illustrated as follows: Suppose that the peened sample is made up of many thin plate layers, which are stacked together, and there are no friction between adjacent layers. When the very first plate was bombarded by the shots, it will extend in the planar direction but shrink in the thickness direction, since there are no constraints from the adjacent layer. The second layer may extend and shrink the same way but with less degree because the impact intensity is lower here than in the first layer. Now if we do consider the constraints from the bottom layers, these top two layers actually could not extend that much, and compressive-residual stresses, thus, can generate in the surface.

Withers and Bhadeshia [24] use Fig. 2.1 to illustrate the formation of the compressive-residual stress during a shot-peening process. It is easy to understand that in the interior of the component, the residual stress becomes a tensile stress since the overall force within the body needs to maintain an equilibrium. Residual stresses generated by shot peening were investigated by many researchers [25–30]. Though the amplitude and distribution of the residual stress are dependent on the shot-peening

parameters and materials, there is a common accepted overall trend of the residual-stress distribution beneath the shot-peened surface. That is, from the very peened surface to unpeened interior, compressive-residual stresses first increase to a maximum and, then, decrease to 0. As the depth continues to increase, they become tensile stresses, as shown in the right plot of Fig. 2.1. Though there are arguments whether the tensile residual stress is constant inside the component or not, the compressive-residual-stress profiles were confirmed by many experiments. For example, Fuchs [25] summarized 15 different residual-stress-distribution profiles, which were measured on different materials with various shot-peening-process parameters, and it is found that all profiles have similar trends in the near-surface layer.

Measurements of residual stress

Many different techniques, including the curvature measurement [31], hole drilling [32], slitting method [23], X-ray diffraction [33], neutron diffraction [34, 35], magnetic and electrical techniques, ultrasonics, thermoelastic methods, etc., could be used to characterize the residual-stress distributions. Withers et al. [24] briefly summarized those methods and their respective fundamental mechanisms. Among those methods, diffraction, i.e., electron diffraction, conventional X-ray diffraction, hard X-ray diffraction, and neutron diffraction, are the most commonly-used techniques.

As mentioned above, the type I residual stress comes from the misfit between different regions, which means that the lattice is distorted if residual stresses are introduced into the material. When an X-ray beam with a wavelength, λ, incidents upon a crystalline material with a lattice spacing, d, a diffraction pattern with sharp maxima is produced. The positions of the diffracted x-ray will be given by the Bragg's law [36]:

$$2d \sin\theta = n\lambda \tag{2.1}$$

where 2θ is the diffraction angle, $n = 1, 2, \cdots$, is a integer representing different diffraction levels.

For the specimen free of stresses, the lattice spacing is fixed, so as the diffraction angle. However, a small change in the lattice parameter, Δd, will result in a change of $\Delta\theta$ in the Bragg angle so that the lattice elastic strain in the direction of the scattering vector, Q, is given by [28]:

$$\varepsilon = \frac{\Delta d}{d} = -\Delta\theta \cdot \cot\theta \tag{2.2}$$

Typically in order to obtain a resolution in a strain of 10^4 (corresponding to a stress of about 20 MPa in most engineering materials), it is necessary to measure peak shifts to an accuracy of 0.005°. In general, to completely define the stress tensor at a point, measurements of strains in six orientations are required. However, when the principal directions are known, three orientations will suffice [28]. When these orientations coincide with the coordinate directions x, y and z, the principal stresses are given by

$$\sigma_x = \frac{E}{(1+\nu)(1-2\nu)}[(1-\nu)\varepsilon_x + \nu(\varepsilon_y + \varepsilon_z)] \tag{2.3}$$

with corresponding expressions for σ_y and σ_z. In this equation, E is the elastic modulus, and ν is the Poisson's ratio, respectively. The values of those parameters appropriate to the specific (hkl) crystallographic plane on which the strain is being measured are used [37, 38].

The above-mentioned method is applied to materials with any crystallographic structures. In this thesis work, since the material used is a face-centered cubic (fcc) superalloy, another method, which only applied to the fcc material and has a high accuracy, is presented below.

It is well established that twins broaden the X-ray diffraction (XRD) peaks of fcc materials asymmetrically [39, 40]. Thus, in principle, it is possible to calculate twin probabilities (γ) from either the peak-broadening or asymmetry. However, the peak-broadening approach has met with the limited popularity because, apart from twins, the peak-broadening may also be induced by faults, grain-size refinement, dislocation polygonization, crystal-lattice microstrains, and instrumental causes [41, 42]. This phenomenon makes it very difficult to evaluate γ from the peak-broadening, especially

for materials processed via shot peening. This problem becomes more tractable in the peak-asymmetry approach, since the contribution from twins can be isolated more easily. In this context, γ can be readily evaluated from the lower limit of the Fourier sine coefficients (B_n with n being the ordinal of the Fourier coefficients) of the XRD peaks after excluding the instrumental broadening, that is, through the following relation [36]:

$$\gamma = C_t\sqrt{3}(B_n)_{n\to 0} \tag{2.4}$$

where the constant, C_t, adopts the value $4/3, -1, 2, 0, -4/3$, and 1 for the 111, 200, 220, 311, 222, and 400 peaks, respectively.

However, to avoid the calculation of B_n in practice, γ is simply estimated directly from the residual asymmetry of the 200 peak through the following relation [36]:

$$\gamma = \frac{\sqrt{3}\pi 2\theta^r (I^{2\theta_l} - I^{2\theta_r})}{2\beta}\left(1 + \left[\frac{\lambda}{4\pi D_{eff,200}(\sin\theta^r - \sin\theta_{B,200})}\right]^2\right) \tag{2.5}$$

where λ is the radiation wavelength, β and $\theta_{B,200}$ are the integrated intensity, and the Bragg angle of the 200 peak, respectively, $D_{eff,200}$ is the effective crystallite size along the 200 crystallographic direction, $2\theta^r$ is any diffraction angle on the high-angle tail of the 200 peak, $I^{2\theta_r}$ is the intensity at $2\theta^r$, and $I^{2\theta_l}$ is the intensity at the equidistant position of $2\theta_{B,200}$ with respect to $2\theta^r$ at the low-angle tail of the 200 peak.

It is well recognized that faults broaden and shift the XRD peaks of the fcc materials [39, 40]. Thus, in principle, it is feasible to calculate fault probabilities (α) from either the peak-broadening or shifting. Similar to the γ case, α is not easily evaluated from the peak-broadening either, and is typically calculated from the peak shifting. It has been demonstrated that faults shift the peaks from the theoretical positions dictated by the unit-cell dimensions according to the following [36]:

$$\Delta_f(2\theta) = 2\theta_0 - 2\theta_B = \frac{90\sqrt{3}C_f \tan\theta_0}{\pi^2}\alpha \tag{2.6}$$

where $2\theta_B$ and $2\theta_0$ are the peak positions in the absence and presence of faults, respectively, and the constant, C_f, adopts the value of $1/4, -1/2, 1/4, -1/11, -1/8$

and 1/4 for the 111, 200, 220, 311, 222, and 400 peaks, respectively. Equation 2.6 can, thus, be used to evaluate α directly if there are no other sources of peak shifting, which seldom happens in practice. However, this obstacle can be circumvented by examining the shiftings of the neighboring peak pairs with an opposite sign for the constant, C_f. Hence, α can be calculated readily with the aid of the following relation [36]:

$$\alpha = \frac{\pi^2[\Delta_f(2\theta_1 - 2\theta_2)]}{90\sqrt{3}(C_{f,1}\tan\theta_1 - C_{f,2}\tan\theta_2)} \tag{2.7}$$

where the subscripts 1 and 2 are used to distinguish between the two peaks forming the pair.

It is a well-known phenomenon that the unit-cell dimensions dictate the Bragg positions of the XRD peaks [43]. Thus, in the absence of the instrumental peak shifting, the lattice parameter (a) of a fcc material is determined from the experimentally-measured peak positions ($2\theta_0$) using the Bragg law coupled with the plane-spacing equation for the cubic crystal system [43]:

$$a = \frac{\lambda\sqrt{h^2 + k^2 + l^2}}{2\sin(\theta_0 - \frac{\Delta_f(2\theta)}{2})} \tag{2.8}$$

where h, k, and l are the Miller indices of the XRD peaks, and λ is the radiation wavelength. The term, $\Delta_f(2\theta)/2$, in Eq. 2.8 is included to correct the $2\theta_0$ peak positions for the possible fault-induced peak shifting, and is calculated from Eq. 2.6.

It has been demonstrated that the set of plane spacings of a distorted crystal structure (d_0), and, therefore, its corresponding set of peak positions in the XRD pattern, change with respect to the distortion-free reference condition (d_0^R) [41, 43, 44]. In this way, the peak positions also contain the information of the elastic strain of crystallites, which can be calculated for each hkl lattice plane through the following relation [43, 44]:

$$\varepsilon = \frac{d_0 - d_0^R}{d_0^R} = \frac{\sin\theta_0^R - \sin(\theta_0 - \Delta_f(2\theta)/2)}{\sin(\theta_0 - \Delta_f(2\theta)/2)} \tag{2.9}$$

where $2\theta_0$ and $2\theta_0^R$ are the peak positions with and without the elastic strain, respectively, and $\Delta_f(2\theta)/2$ has been defined before. If the cause for such elastic strains

is the existence of macroscopic residual stresses acting on the crystallites, Hooke's law can be used to connect both magnitudes. For the rotationally-symmetric biaxial state of stresses, typical of the surface region of the material subjected to shot-peening processing, the stress perpendicular to the impacted surface is zero ($\sigma_{33} = \sigma_{\perp} = 0$), whereas the stresses parallel to the impacted surface are both non-zero and equal ($\sigma_{11} = \sigma_{22} = \sigma_{\parallel} \neq 0$). The following relation can be derived for such a scenario [43, 44]:

$$\sigma_{\parallel} = -\frac{E}{2\nu}\varepsilon \tag{2.10}$$

where E and ν are the Young's modulus and Poisson's ratio of the workpiece, respectively, and ε can be found from Eq. 2.9.

Equations 2.4 to 2.10 provide another method to characterize the residual stress in the fcc-structured material. It should be pointed out that the residual stress measured according to the above-mentioned two methods is an average value if the diffraction is conducted on the sample surface. However, in a shot-peened sample, it is known that the residual stresses are not evenly distributed along the depth. Therefore, to obtained a residual-stress profile along the depth, some other techniques will be mentioned and used in the next chapter.

Effects of residual stresses

The data available on fatigue as influenced by shot peening provides a great deal of evidence that the major reason for the increase in the fatigue strength lies in the layer of compressive stresses at the surface of the part. In general, fatigue failures are due to a repeated change of the stress in which the maximum stress is tension or involves a tension component. Rarely, if ever, do fatigue failures occur as the result of compressive stresses. This means that the compressive stress at the surface is all to the good [45].

An intuitionistic explanation for the improvement of fatigue by compressive-residual stresses is as follows: The induced compressive-residual stress reduces the

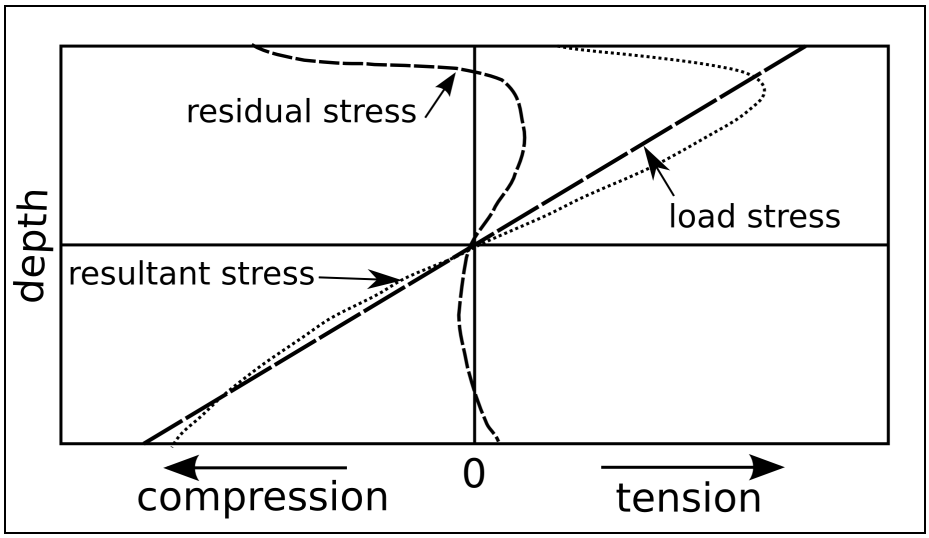

Figure 2.2: Schematic illustration of the effects of compressive-residual stresses on the actually stress amplitude in a bending test

applied stress field near the surface, which results in a reduced stress range, thereby, extending the fatigue life [46]. It should be noted here that the improvement effect of the residual stress is only pronounced when the applied stress amplitude is moderate. When the external applied stress is high, the cyclic-plastic strains introduced may be sufficient to cause the plastic deformation and stress redistribution at the crack tip, which may eliminate the effects of the original compressive-residual-stress field. Furthermore, it has been shown that the relaxation pattern of the residual stress is faster and more severe at high stress levels than in low stress levels [21].

Figure 2.2 schematically shows the stress state of a shot-peened bar under a bending load. This figure is modified based upon Grover's paper [26] for a simpler understanding. In this figure, the top surface was subjected to the shot-peening process, and compressive-residual stresses were introduced. The stress state has been simplified to a uniaxial-longitude stress. The load stress is the external stress applied on the bar sample, and the resultant stress is the actual stress when the external stress was partially counteracted by the residual stress. It is shown that under a bending load (this is also the load mode under a bending-fatigue test), the near-surface compressive-residual stress could effectively reduce the tensile-stress amplitude, thus, inhibit or retard the crack initiation and propagation.

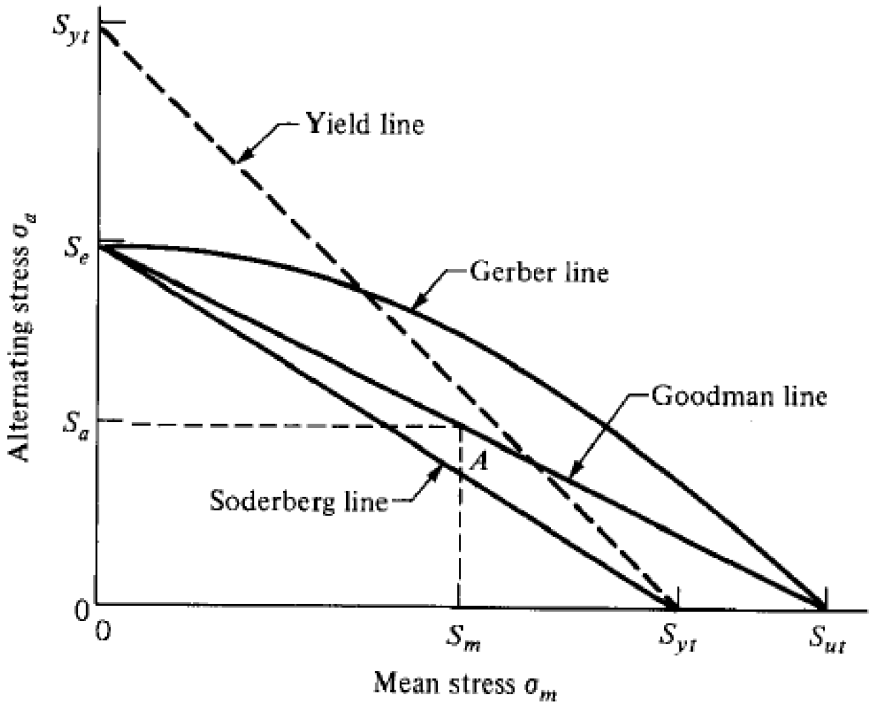

Figure 2.3: Schematic illustration of the effects of mean and alternating stresses on the fatigue limits represented by the Goodman's relation [47].

It is well known that Goodman diagram represents an empirical equation, which relates the mean stress (σ_m) and the alternating stress (σ_a) with the fatigue limits. As shown in Fig. 2.3, any combination of mean and alternating stresses that lie on or below the Goodman interaction line will have an infinite life. The Soderberg interaction line and the Gerber interaction line have a similar trend as the Goodman line. However, because they are based upon different assumptions, the line shapes have some minor differences. For a modified Goodman equation, the line is supposed to never exceed the yield line. That is, the Goodman line located outside the yield line should be replaced by the yield stress line [47].

For the specimen with compressive residual stresses, as shown in Fig. 2.2, it is noted that at the near-surface layer, the amplitude of the applied stress was reduced by whatever the compressive-residual-stress amplitude is, but the alternating stress amplitude does not change. Suppose that the maximum and minimum applied stresses are σ_{max} and σ_{min}, respectively, and the residual stress is σ_r. Then the actual

alternating stress, $\sigma_{a,actual}$, and actual mean stress, $\sigma_{m,actual}$, should be represented as

$$\sigma_{a,actual} = \frac{(\sigma_{max} - \sigma_r) - (\sigma_{min} - \sigma_r)}{2} = \frac{\sigma_{max} - \sigma_{min}}{2} \tag{2.11}$$

$$\sigma_{m,actual} = \frac{(\sigma_{max} - \sigma_r) + (\sigma_{min} - \sigma_r)}{2} = \frac{\sigma_{max} + \sigma_{min}}{2} - \sigma_r \tag{2.12}$$

Surely, it can be concluded from the above equations that the alternating stress amplitude does not change but the mean stress is reduce by σ_r when residual stress is introduced into the specimen. According to Goodman's relation shown in Fig. 2.3, the effect of the compressive residual stress is moving a point horizontally to the left. Since inside the Goodman's line is "fatigue-free" zone, introduction of compressive residual stress will increase the fatigue strength (or fatigue limit) of the specimen. Actually, residual stresses are dealt with in the same way as mean stresses when its effects on the fatigue is considered [48].

Many theoretical models [21, 22, 46, 49–51] have been developed to predict the fatigue life of the specimen with residual stresses. Newman et al. [50] reviewed the capabilities of a plasticity-induced crack-closure model, life-prediction code, FASTRAN, to correlate and to predict small- and large-crack growth rate behavior in several aluminum and titanium alloys under various load histories. A constraint factor, which accounts for three-dimensional state-of-stress effects, was used in determining the effective stress intensity factor range against rate relations. It is found that the predicted results were well within a factor of two of the test data.

Moshier et al. [46] use a probabilistic approach to predict the distribution of fatigue lives of the sing-edge notch tension specimen with compressive residual stress. The fatigue lives were predicted by a modified version of FASTRAN II and conditional probability. It is concluded that compressive residual stresses act as an external closing mechanism, taken into account by breaking the closure mechanism into two part, and the closure mechanism was modelled as the total of a reduced opening stress and the compressive residual stress. The modification to the deterministic life

prediction model to account for the presence of compressive residual stresses were found effective in predicting the variability in the experimental fatigue lives.

Kumar [51] attempted to detect crack initiation and measure crack growth in the heavily deformed surface layers of several aluminum alloys subjected to the shot-peening process using several measurement techniques. Using the closure model and some microstructural features, such as inclusion-particle sizes and cladding-layer thickness, a total fatigue-life prediction method was demonstrated. The results indicate that the effects of peening did not sufficiently retard crack growth for the specimen geometry chosen.

A typical crack-growth rate, da/dN, vs. the stress-intensity-factor range, ΔK, curve is shown in Fig. 2.4 [28]. In the figure, regions A and C are very sensitive to the mean stress, i.e., the fatigue-growth rate is easily affected by the mean stress. Region B is a steady region, where the mean stress shows little influence on the crack-growth rate. It is pointed out that an increase in the load ratio, $R(= K_{min}/K_{max})$ has the effect of moving regions A and C to lower ΔK values. The presence of residual stress can alter both R and ΔK over which the crack remains open. i.e.,

$$R_{eff} = \frac{K_{min} + K_{res}}{K_{max} + K_{res}} \tag{2.13}$$

where K_{res} is the stress-intensity factor due to the residual-stress distribution alone [28]. In a compressive-residual stress case, because R_{eff} is smaller than R, ΔK will be moved to the left accordingly, thus the crack-growth rate will be reduced.

In summary, the effect of compressive residual stresses on the fatigue strength of a shot-peened sample can be illustrated by Fig. 2.5. As the compressive-residual stress in the near-surface layer increases, the fatigue strength of the sample decreases accordingly.

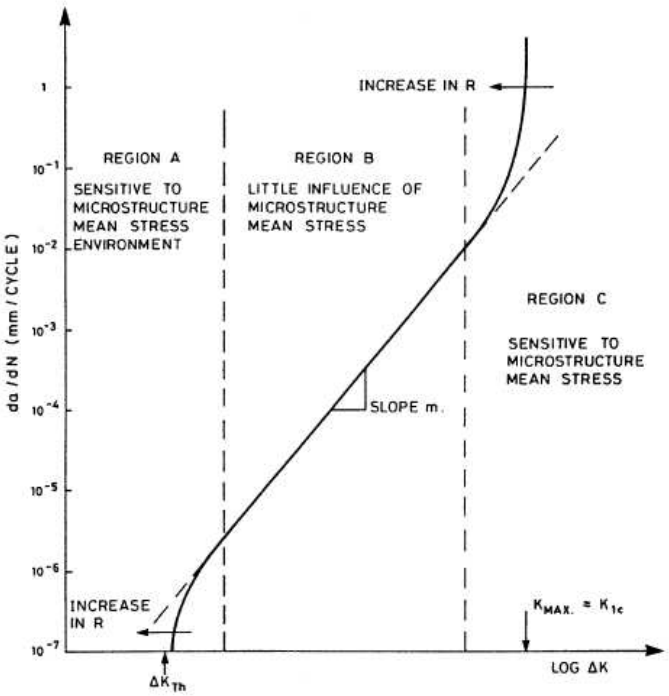

Figure 2.4: Representative fatigue-rack-growth curve [28].

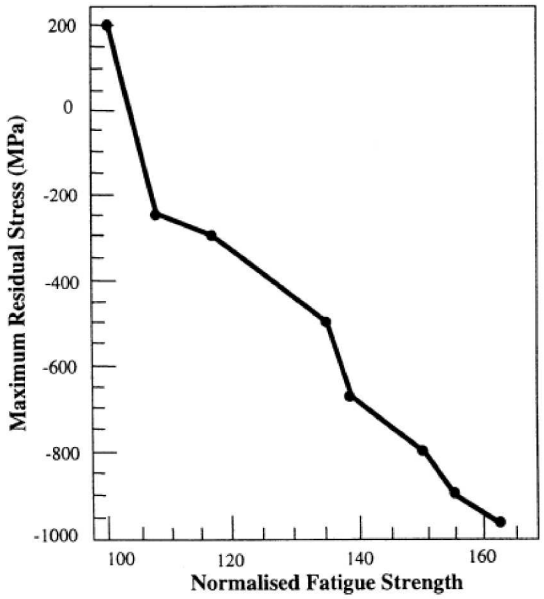

Figure 2.5: Improvement in fatigue strength due to near-surface compression induced by shot peening [28].

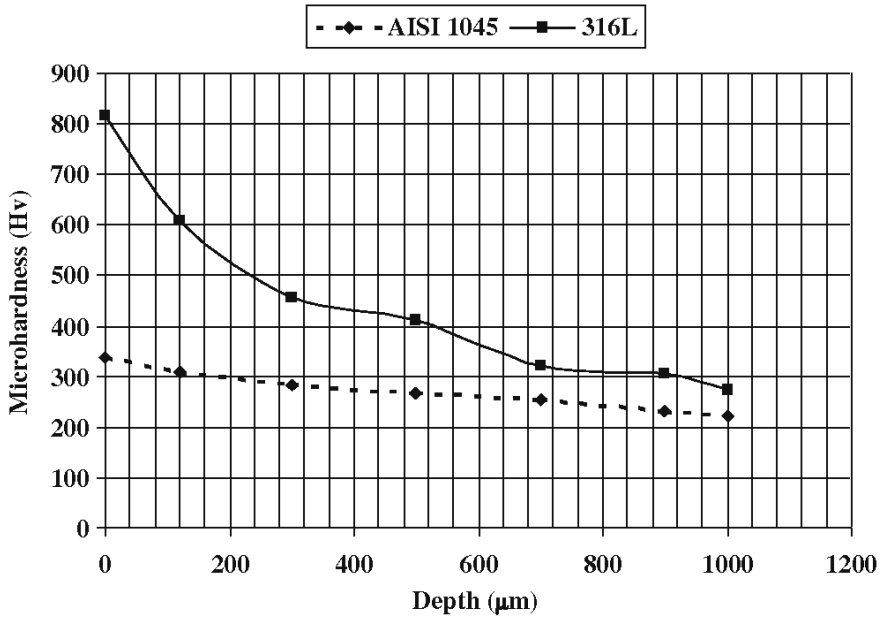

Figure 2.6: Hardness profile of the AISI 1045 and 316L steels subjected to shot peening. Note that the different process parameters are used for these two samples [52].

2.1.3 Work hardening

Work hardening is defined as when a material deforms beyond its yield point, an increasing stress is required to produce additional plastic deformation, and the metal apparently becomes stronger and more difficult to deform. During a shot peening process, due to the high-intensity bombardment of the shots, plastic deformation usually occurs within the surface layer of the component, and, thus, work hardening was introduced in some work-hardenable materials.

Work hardening caused by the shot-peening process was found in many industrial materials, such as medium carbon steels, AISI 1045 and 316L [52], aluminium 2024-T351 alloy [22], cast iron [12], SAE 3415 ductile steel [53], and so on. Though the hardness distribution of a shot-peened component is highly affected by the material and peening parameters, such as pressure, shot size, nozzle distance, etc. [52], the hardness profiles on the side surface have similar trends, as shown in Fig. 2.6. e.g., from the surface to the interior, the hardness decreases gradually until reaching the unaffected hardness value.

Similar to residual stresses, work hardening also plays an important role in affecting the fatigue behavior of a shot-peened specimen. It is believed that work hardening of the peened layer affects the spread of plasticity at the crack tip (a barrier strength) [22, 53], i.e., the plastically-deformed region around the crack tip becomes stronger and its resistance to further plastic deformation was improved by the work-hardening effects.

Actually, in Pariente et al.'s work [54], it is even proposed that work hardening plays a more important role than compressive-residual stresses do in affecting the fatigue resistance. It is found that the fatigue-strength improvement induced by shot peening is mainly related to the hardening of the surface layer of a material and not to the residual-stress field induced, and compared with the residual stresses, work hardening is more stable during the fatigue test. In Rios et al.'s another paper [55], it is also stated that a short crack is not able to produce closure, and the improvement in the crack-growth resistance is assumed due to the distortion and work hardening of the peened layer.

Theoretically, Pariente et al. [54] proposed a model, which combines the work hardening and residual stress, to predict the fatigue stress-intensity-factor-range threshold, ΔK_{th}, as follows:

$$\Delta K_{th} = 3.3 \times 10^{-3}(HV + 120)(\sqrt{area})^{1/3} \left(\frac{1 - R_{\Delta K}}{2}\right) \left(\frac{FWHM_{NSP}}{FWHM_N}\right) \quad (2.14)$$

where HV is the Vicker's hardness value, $\sqrt{area}$ is the projected shape of the initial defect, $R_{\Delta K}$ is the load ratio, which corresponds to the ratio of the minimum load to the maximum load, with the residual stresses taken into account. FWHM is the full width at half maximum of the diffraction peak, and its subscripts corresponding to materials treated with series of nitrided and shot peening (NSP) and series of nitrided specimens. The last term is included for the purpose of considering the distortion caused by the shot-peening process.

Equation 2.14 clearly shows that as the increase of hardness, ΔK_{th} increases accordingly. Since a crack usually initiates from the sample surface during fatigue,

the work-hardened surface layer can obviously increase the fatigue strength based on this equation. Actually, it is shown that it works pretty well in their experiment [54].

Therefore, it can be concluded that when work hardening occurs during a shot-peening process, as the surface hardness increases, the threshold of the stress-intensity-factor range needed for crack growth increases accordingly, and the fatigue strength is, thus, improved.

2.1.4 Surface roughness

One of the interesting features of the shot-peening process is that the fatigue improvement is more pronounced for a component with a rough surface than for one with a smooth surface. In other words, it is more likely to see an improvement in the fatigue strength in a component with a great amount of surface defects, but it may not so obvious in a sample with a well-polished surface. To explain this phenomenon, the effects of shot peening on the sample-surface quality must first be clarified.

Since the shot-peening process is conducted through the repeated bombardment of small shots on the sample surface, the impact may cause plastic deformation when the impact energy is high enough (which is true in most cases). Therefore, a small indent might be left on the sample surface when the shot bounces back. After numerous bombardments, a uniform but not smooth surface might be formed, and this is usually referred as the surface roughening effects of a shot-peening process [52, 56].

The above mentioned phenomenon is true when the original sample surface is smooth. However, for a sample with a rough original surface , the situation is different. During a peening process, the impact not only has the effect of introducing small indents (thus roughening the surface), but also has the capability to remove high surface peaks through deformation-caused materials flows. From this point of view, it could actually “smoothen” the surface.

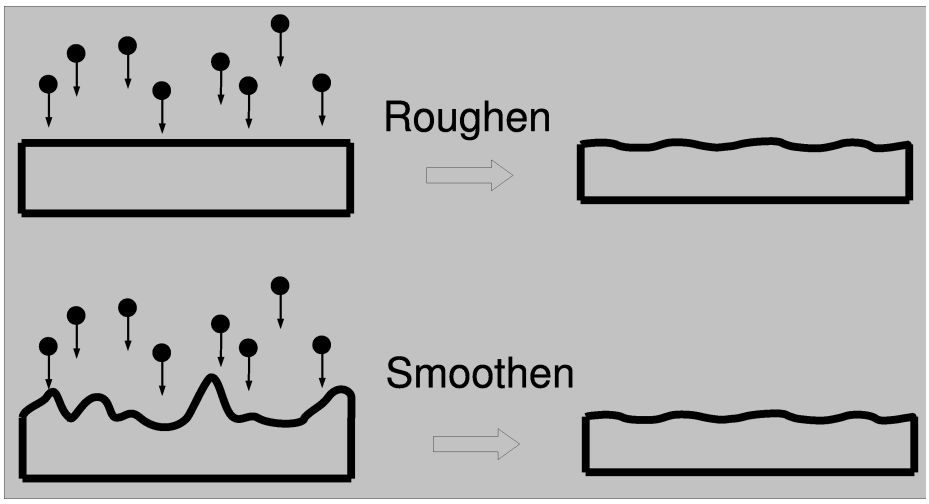

Figure 2.7: Surface roughness could increase or decrease depending on the original surface quality

The above-mentioned statements could be illustrated through Fig. 2.7. Assuming that after the shot-peening process, the surface roughness can always reach a saturation point, i.e., a stable peak-valley distance value can be obtained. Then for an original smooth surface, roughness goes up; while for an original rough surface, surface roughness goes down after the shot-peening process.

It can be concluded from the above illustration that whether the surface becomes more rough or more smooth after the shot-peening process depends on the original surface quality. In terms of fatigue damage, surface roughening will accelerate the nucleation and early propagation of cracks [53, 57]. This is usually because that the uneven surface provides many potential crack-initiation sites due to the stress-concentration effect. In this case, effects of surface roughness can be considered as effects of surface notches, which have been extensively explored in many textbooks [7, 47].

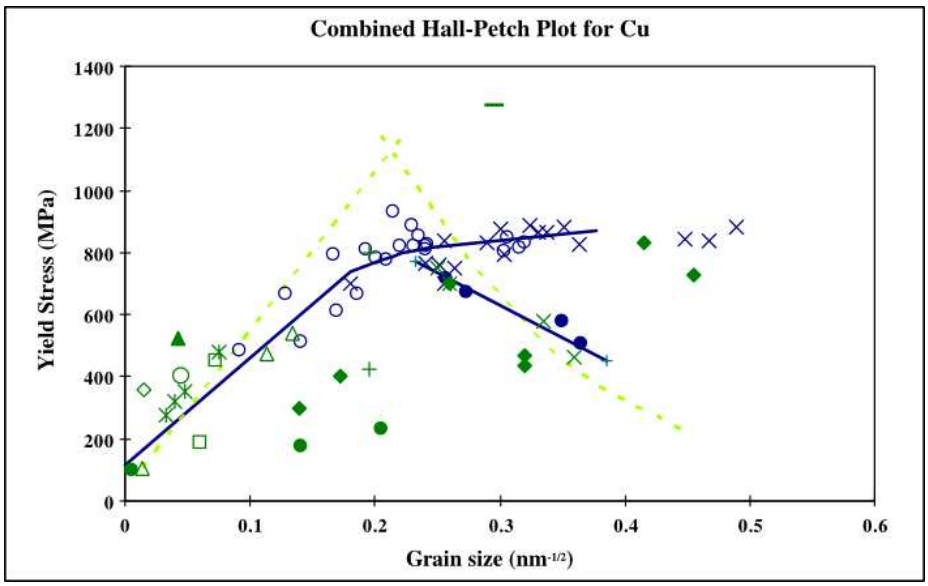

Figure 2.8: Yield-strength changes with grain sizes of pure copper with different synthesis methods. It is shown that the Hall-Petch relation does not hold when the grain size smaller than about 25 nm [8].

2.2 Mechanical Properties of Nanocrystalline Materials

2.2.1 Overview

As is known that a fine-grained material usually has better mechanical properties, which have been widely investigated especially on the constitutive response and the fundamental physical mechanism in the past twenty years [58–66]. The Hall-Petch relation indicates that the yield strength could be improved by decreasing the grain size, which is confirmed in most of the polycrystalline materials and in a wide range of grain sizes. When the grain size decreases to about 25 nm, the yield strength of the material was found to decrease as the grain size decreases. However, reducing the grain size to $250 - 1,000$ nm (an ultra-fine grain size) or $1 - 250$ nm (a nano grain size) through a grain-refinement process is still an effective method to improve the overall properties of the materials [8]. Figure 2.8 shows the relationship between the yield strength and grain size of pure copper from different resources. It is shown that the simple linear relation (determined by the Hall-Petch equation) does not hold when $d^{-1/2}$ decrease to $0.2 - 0.3$ nm$^{-1/2}$, i.e., $d \approx 25 - 10$ nm.

Meyers et al. [8] reviewed the main synthesis methods and the mechanical properties of fine-grained or nanocrystalline materials. The basic idea behind the synthesis methodology is breaking the large grain size down (a top-down method) or consolidating small clusters up (a bottom-up method). One typical example of the former method is the severe-plastic deformation process, such as the equal-channel-angular pressing (ECAP) [67, 68] and high-pressure torsion (HPT) [8, 69], while many other methods, such as the gas condensation, mechanical alloying, chemical/physical vapor deposition, etc., belong to the latter category. It is also pointed out that one shortcoming of the bottom-up strategy is the possibility of the porosity and incomplete bonding among the grains [8].

2.2.2 Mechanical properties

Mechanical properties, in particular, the yield strength, of conventional polycrystalline materials, are pronouncedly affected by the grain size no matter which synthesis strategy is used. Weertman et al. [70] found that in the nanocrystalline Cu and Pd samples synthesized by the inert gas condensation, a great enhancement was observed in their yield strength and hardness. Valiev [61, 71] also reported a high yield strength in the ultrafine-grained Cu sample prepared by the severe-plastic deformation.

Besides the high yield strength, nanocrystalline materials exhibit many other good mechanical properties, such as the good ductility, good corrosion resistance, improved toughness and wear resistance, and enhanced diffusivity [8]. Kumar et al. [62] summarized the mechanical behavior of nanocrystalline alloys and metals, and pointed out that the dislocation motion, void formation/growth at grain boundaries and triple junctions, and the interaction of these features are the main reasons for the improvements. The improved mechanical properties of the nanocrystalline materials are usually attributed to the large volume fraction of grain boundaries and/or twin boundaries, which act as barriers so as to restrict the motions of dislocations. A simple estimation shows that the volume fraction of the interface can reach as high

as 50% for 5-nm grains, and decreases to 30% for 10-nm grains, and about 3% for 100-nm grains [72].

However, as one of the most important mechanical properties of the engineering components, fatigue strength does not obviously benefit as much from the nanocrystallization process as other properties, such as the yield strength does [73]. Actually, it is found that bulk nanocrystallization is not an effective, or at least not an economic process to improve the fatigue property of a component. The reason is that the fatigue strength is not a monotonic function of the grain size. It is known that small grains could effectively increase the yield strength so as to enhance the fatigue crack-initiation threshold [8, 74–76]. Meanwhile, a small grain size also has an adverse effect on the resistance to the fatigue-crack growth, since cracks can easily propagate along grain boundaries.

A comparison plot of the crack-growth rate among components with different grain sizes is shown in Fig. 2.9. It can be seen that when the stress-intensity-factor range, ΔK, is relatively small, the crack-growth rate of a component with 30-nm grains can be 10 times faster than that with 300-nm grains. On the contrary, coarse grains may deflect the propagation paths of fatigue cracks by grain boundaries, thus introducing crack closure and decreasing the rate of crack growth. However, coarse grains are not effective in preventing the initiation of the fatigue crack [8]. As shown in Fig. 1.1 in Chapter 1, crack propagation can be effectively deflected by large grains but not by small ones. Because of the co-existed competitive effects, it is not surprising to found in the literature reports that there are no good agreements among different sources.

For example, in Vinogradov's [9] investigation of an ultra-fine grained titanium obtained by the severe-plastic deformation through equal-channel-angular pressing (ECAP), it was shown that when the grain size changed from 100, 32, to 9 μm, the fatigue strength pronouncedly increased. In the ultra-fine crystalline 6061 Al alloys subjected to the equal-channel-angular pressing, significant improvement in the fatigue strength was found after one ECAP pass while no improvement was observed

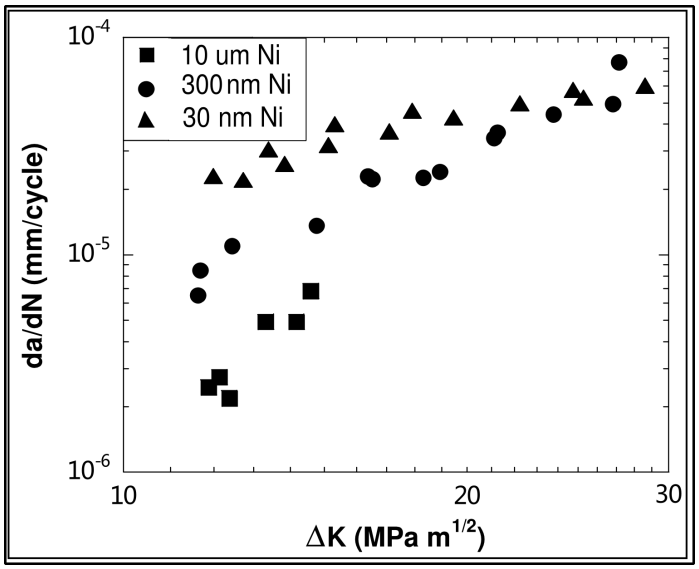

Figure 2.9: Crack-propagation rate, da/dN, changes with the stress-intensity-factor range, ΔK. It is shown that a small-grain sample has a much faster crack-propagation rate than a coarse-grain one especially when ΔK is low [77].

at all after further deformation, though from the point of view of the grain size, in the latter case the grain size is much smaller than the former [10].

Therefore, it is believed that a component with a nano-grained surface and a coarse-grained interior should have a good fatigue resistance, because (1) on the surface, the small grains can effectively resist the fatigue-crack initiation, and (2) in the interior, the large grains can deflect the fatigue-crack propagation and, thus, increase the fatigue life.

2.3 Surface-Severe-Plastic-Deformation Process

2.3.1 Overview

To obtained a component with a nano-grained surface and a coarse-grained interior as stated in the previous section, a modified shot-peening process, which uses a higher bombardment energy than that in a conventional shot peening during the process, was developed recently. The modified shot-peening process could be referred as the surface-severe-plastic-deformation (S^2PD) process. Variants of the

S^2PD process include the surface-mechanical-attrition treatment (SMAT) [78–81], ultrasonic shot peening (USSP) [82–84], high-energy shot peening (HESP) [85], air blast shot peening [86], and surface nanocrystallization and hardening (SNH) [87–89], etc.

The basic ideas behind those different processes are the same: using high-energy balls to impact the sample surface so as to introduce compressive-residual stresses as well as modify the near-surface microstructures. These S^2PD-based techniques have been shown to improve tensile strengths [85], microhardness [87], and wear resistances [84, 90] of the materials. Clearly, these results demonstrate that surface S^2PD-based techniques are alternative approaches to enhance the surface properties and upgrade the global properties of engineering materials without the change of chemical composition, as the physical-vapor-deposition (PVD) and chemical-vapor-deposition (CVD) processes have.

The S^2PD process has been successfully applied on many materials, including metals, steels, and alloys [78, 79, 82, 83, 85]. In those materials, near-surface nanocrystalline layers were observed after the process, and the grain-refinement mechanism has been extensively discussed. However, compared with the grain refinement, or nanocrystallization, mechanism, only a few studies have focused on the effects of the near-surface nanocrystalline layer on the mechanical properties of the component [85, 87, 90].

2.3.2 Comparison with shot peening

It is clear that the S^2PD process is based upon the traditional shot peening process, and both of them can alter the residual stress, work hardening, and surface roughness of the near-surface region of a component. However, the significant difference is the near-surface nanocrystalline formed during a S^2PD process, which may pronouncedly affect the mechanical properties of the material. A detailed comparison in terms of the impact energy simulated by finite-element modeling between the two

processes can be found in the literature [89]. It is shown that a higher impacting energy is more effective in introducing nanocrystlline, and if the impacting energies are the same, small size balls are more favorable for the formation of nanocrystalline layers.

Basically, the main feature for an S^2PD process is the high-energy impact of the work-piece surface by high-velocity balls. The high velocity of balls is typically generated through collision between balls and a vibrating chamber driven by an ultrasonic generator or mechanical vibration, as illustrated in the SMAT, USSP, or SNH process, etc. In some other cases, the velocity of balls can also be generated through a high pressure light-gas gun, which accelerates particles to a desired impact velocity, named as the particle impact processing (PIP) [91]. These S^2PD-based processes can result in a nanocrystalline surface layer up to about 50-μm thick, and have been shown to improve the tensile strength, microhardness, wear resistance, and fatigue strength of materials [89].

Kinetic energies, E_k, of the impacting balls and shots can be estimated through the equation, $E_k = mv^2/2$, where m is the mass of the ball or shot, v is the velocity. Assuming that WC/Co balls are used in the all the process, according to the estimated impacting velocity, the typical kinetic energies of different variants of S^2PD processes and the SP process are summarized in Table 2.1. It can be seen that PIP has the highest kinetic energy, followed by SNH and SMAT, and then HESP. Though there are some differences among different S^2PD processes, the overall kinetic energies of those S^2PD process are obviously higher than that of the SP process. i.e., SP has the lowest kinetic energy which may overlap with the kinetic energy of USSP, depending on the diameter and velocity of balls and shots used. The simulation results also indicate that the SNH process has a higher kinetic energy, produces a thicker work-hardened layer and a thicker surface region with larger residual compressive stresses, and generates higher effective plastic strains than the SP process [89].

Table 2.1: Typical parameters of balls and shots used in SP and various S^2PD processes

Process	Ball Diameter (mm)	Velocity (m/s)	Kinetic Energy (J) *
SP	$0.25 - 1.0$	$20 - 150$	$9.2 \times 10^{-6} - 0.01$
USSP	$0.4 - 3.0$	< 20	$0.0001 - 0.02$
SMAT	$2.0 - 10$	$2 - 5$	< 0.2
HESP	$4.0 - 8.0$	$2 - 3$	< 0.018
SNH	$4.0 - 8.0$	$5 - 15$	$0.0063 - 0.43$
PIP	4.0	120	1.88

*Kinetic energy is also dependent of the density of the ball and shot used. It is assumed that WC balls and shots are used in all of these processes.

It is shown that compared to a typical SP process, the S^2PD process has a much higher kinetic energy. Thus, it may produce a thicker work-hardened layer and a thicker surface region with larger residual compressive stresses, and generate higher effective plastic strains. Consequently, the thickness of the nanocrystalline surface layer formed during the process should also be much thicker in the S^2PD process than in the SP process. Therefore, the formation of the near-surface nanocrystalline layer is deduced to be positively related to the high impact energy, and the factors, which relate to the impact energy and formation of nanocrystallites, should be essential to the process.

2.3.3 Grain refinement

Grain-size measurement

To investigate the plastic-deformation-induced grain-refinement mechanism, it is necessary first to review the grain-size-measurement methods. Though the high-resolution transmission-electron microscopy (HRTEM) is probably one of the most accurate technique in characterizing the grain size of single nanocrystallite, it is surely not the most convenient way in estimating the overall grain size in a component

due to the expensive equipment and the complex sample preparation. In macro-grain-size range, an automatic image-analysis methodology has been applied in many commercial instruments. However, when the grain size goes down to nanometer scale, X-ray diffraction (XRD), on the other hand, is a more simple and common method, which can be used to achieve the goal.

It is a well-known fact that the crystallite smallness and/or the crystal lattice microstrain cause peak-broadening [41, 42, 92, 93]. Thus, the width, integral breadth, variance, and in general any other shape parameters of the peaks carry the direct information of the crystallite dimensions and the abundance of lattice defects. The method of estimating the grain size by XRD through the full width at half maximum (FWHM) is presented below.

When the XRD test is conducted on the deformed sample surface, based on the absorption coefficient of Ni [43], it is estimated that 90% of the XRD signals are from the top 100-m surface layer, which varies slightly with the reflection angle. For a plastically-deformed sample, peak broadening will occur in all the diffraction angel range. It is well known that the peak broadening can be induced by nano-grains, internal strains, and instrumental broadening [36]. The FWHM of the sample peak, $\beta_g(2\theta)$, which excludes instrumental broadening, can be calculated with the following equation [36]

$$\beta_g^2(2\theta) = \beta_h^2(2\theta) - \beta_f^2(2\theta) \tag{2.15}$$

if it is assumed that the instrumental and the sample peak functions are both Gaussian in nature. The $\beta_h(2\theta)$ in Eq. 2.15 is the FWHM measured from the sample with the SNH treatment, $\beta_h(2\theta)$ is the one from the standard, and θ is the Bragg angle. The FWHM of the untreated sample can be used as the standard in this method. Once $\beta_g(2\theta)$ of the low-angle reflections is found from Eq. 2.15, it can be employed to estimate the average grain size, D, of the Ni surface with the aid of the Scherrer formula [94]

$$\beta_g(2\theta) = \frac{0.9\lambda}{D\cos(\theta)} \tag{2.16}$$

where λ is the wave length of the X-ray radiation.

The FWHM of high-angle reflections computed from Eq. 2.15 can even be utilized to estimate the effective internal strain, 2ξ, within the face-centered cubic Ni crystal, using the Stokes and Wilson formula [36]

$$\beta_g(2\theta) = 2\xi \tan\theta \tag{2.17}$$

The estimation of grain sizes and effective internal strains of severely-plastically deformed samples using Eqs. 2.16 and 2.17 can give fairly good approximations, because the broadening at low-angle reflections mainly relates to the grain size, and the broadening at high-angle reflections is predominately determined by the internal strain [95, 96]. Recently, a detailed XRD analysis [97], using the Rietveld method in conjunction with the Levenberg-Marguardt non-linear least-square fit (LM-fit) and line-broadening analysis, demonstrates that this is indeed the case for nanocrystalline Al alloys that have been subjected to severe plastic deformation.

A second method to estimate the grain size is based upon the equations shown in Section 2.1.1, where XRD is used to characterize the residual stress. Actually, it has been theoretically demonstrated that the average values of the surface-weighted effective crystallite size (D_{eff}) and root-mean-square lattice microstrain (e_{RMS}) along each crystallographic direction can be calculated in the framework of the variance method with the aid of the following relations [98]:

$$D_{eff} = \frac{90K_K\lambda}{\pi(\beta_L - \beta_L^R)\cos\theta_0} \tag{2.18}$$

$$e_{RMS} = \frac{\pi}{360\sqrt{2}\tan\theta_0}\left(\beta_G^2 - (\beta_G^R)^2 - \frac{2(\beta_L - \beta_L^R)^2}{\pi}\left(1 - \frac{K_T^2}{K_K^2}\right)\right)^{1/2} \tag{2.19}$$

where K_K and K_T are the variance-slope and variance-intercept Scherrer constants [99], respectively, β_L and β_G are the integral breadths of the Lorentz and Gauss components of the peaks, respectively, and the rest of parameters have been defined above. The superscript, R, refers to the reference material with only instrumental broadening.

It is well recognized that the effective crystallite size reflects the nano-grain size if the grains are single crystals separated by large-angle boundaries, and the sub-grain structure if the grains are polycrystals with cell blocks in their interior separated by small-angle boundaries [100]. In the case that the cell blocks are mainly fault or twin grids originated from fault-fault or twin-twin intersections, respectively, then the true nano-grain size (D) is given by the following relation [36]:

$$D = \frac{K_K D_{eff} a}{K_K a - (1.5\alpha + \gamma) C_D D_{eff}} \tag{2.20}$$

where the constant, C_D, adopts the values of $\sqrt{3}/4$, 1, $1/\sqrt{2}$, $3\sqrt{11}/2$, $\sqrt{3}/4$, and 1 for the 111, 200, 220, 311, 222, and 400 peaks, respectively, and the rest of parameters have the same meaning as defined before.

Mechanism

Similar to the bulk severe-plastic-deformation processes, such as ECAP [67] and high pressure torsion (HPT) [69], the S^{2}PD process may also refine the grains in the near-surface layer due to the plastic deformation. Furthermore, since from the surface to the interior, the degree of plastic deformation decreases gradually, a grain-size gradient from a nano-scale to normal coarse-scale is expected. As pointed out in Chapter 1, a component with a nano-grained surface and a coarse-grained interior should have a good fatigue resistance, because (1) on the surface, the small grains can effectively resist the fatigue-crack initiation, and (2) in the interior, the large grains can deflect the fatigue-crack propagation and, thus, increase the fatigue life.

During a S^{2}PD process, regardless of the difference in materials or the detailed experimental setups, the formation of nanocrystalites is a process where coarse grains were broken down to small ones through the severe plastic deformation. This is the so-called "top-down" method, and ECAP, HPT and S^{2}PD processes are the typical examples of this method.

However, compared with the ECAP and HPT processes, S^2PD has its advantages. Firstly, because only the sample surface is subjected to the deformation, the energy needed to conduct the experiment is much less in the S^2PD process; Secondly, the experimental equipment is much simpler for a S^2PD process; and thirdly, in terms of improving the fatigue behavior of the component, the S^2PD process is more effective than the other two at least in theory.

Lu et al. [59, 78–80, 101] did a large amount of work regarding the naoncrystallization mechanism of a modified shot-peening process, which were given different names, such as SMAT [78, 79], USSP [82, 83], HESP [85], etc. according to the process characteristics. However, as mentioned above, the grain-refinement mechanism by those processes are very similar.

Tao et al. [82] observed the formation of nanocrystallites in a pure Fe sample processed by the USSP process, and the refine mechanism of the nanocrystals was analogous to the mechanism proposed in the ball-milling process. i.e., the surface treatment provides repeated multi-dimensional mechanical loads at high speeds onto the material surface and generate dislocations and/or shear bands. The shear bands were shown to consist of high-density dislocation arrays. Repeated shot peening creates more dislocations which will be annihilated or recombined (rearranged) to form small-angle grain boundaries separating individual grains. Further treatments may induce changes in the orientation of the grains with respect to their neighboring grains, forming crystallites with a completely random orientation.

Wu et al. [83] have successfully introduced a 62-m thick ultrafine near-surface layer in a Al-alloy through the USSP process. It is shown that with increasing strains, the various microstructural features, e.g., the dislocation emission source, elongated microbands, dislocation cells, dislocation-cell blocks, equiaxed submicro-, and nanocrystal grains etc., were successively produced. It is concluded that during plastic straining, the formation of subgrains through grain subdivision occurs in order to accommodate the strain. The highly-misoriented boundaries are generated by the subgrain rotation for accommodating further deformation.

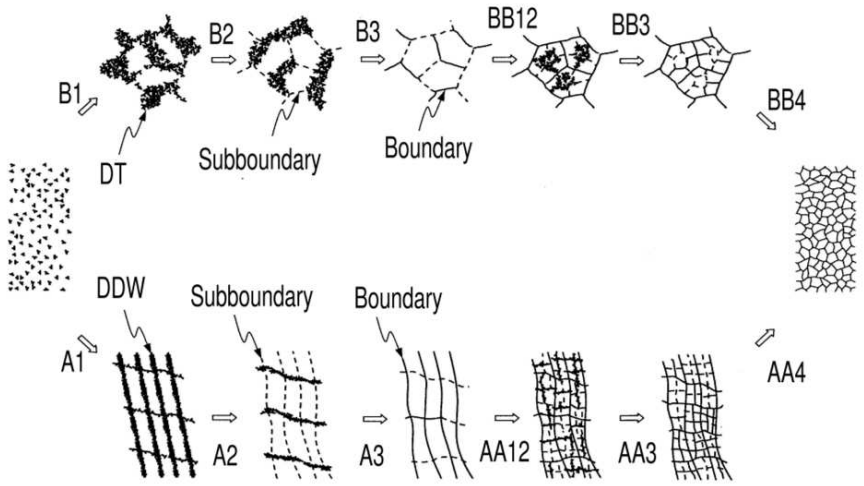

Figure 2.10: Schematic illustration of the main steps of the grain refinement in the S^2PD process. Dislocation tangles (DTs) or dense dislocation walls (DDWs) were first generated by the surface treatment, and then gradually evolves to sub-grain boundaries and grain boundaries. (letter-indicated process B1 to BB4 is corresponding to evolution process of DTs, A1 to AA4 is corresponding to evolution process of DDWs). In the refined grains, this process continues and the grain size then becomes smaller and smaller. As the increase in the processing time and accumulation in the strain, this evolution process also advances from the surface to the interior, and finally a near-surface nanocrystalline layer was formed [80].

In short, it is believed that in the pure Fe and Al-alloy samples, the mechanism of the formation of nanocrystallites has three main steps: (1) the formation of planar dislocation arrays and twins; (2) the grain subdivision and martensite transformation (if any), and (3) the formation of nanocrystallites [78, 79]. Figure 2.10 schematically shows the mains steps of the grain-refinement mechanism. In the figure, due to the different stacking-fault energy, dislocations generated by the impact may form dislocation tangles (DT) or dense dislocation walls (DDT). As the further deformation goes on, the DTs or DDWs can evolve to sub-grain boundaries and grain boundaries gradually, and finally form the nanograins [80].

The stacking-fault energy is one of the most extensively-discussed factors, which affect the grain-refinement mechanism during an S^2PD process. Balogh et al. [102] compared the microstructures of three metal/alloys with different stacking-fault energy subjected to a HPT process. It is shown that negligible twinning in

pure Cu was identitied but the densities of dislocations and twins increased with increasing Zn content. Since the addition of Zn can decrease the stackin-fault energy of the material, it is concluded that for a material with lower stacking-fault energy, twinning or dislocations are easier to be generated in a plastic-deformation process.

Actually, based upon different stacking-fault energies, Lu et al. proposed different nanocrystallization mechanisms for the S^2PD process [80]. The main difference is that the formation mechanism of the grain boundaries. For the high stacking-fault energy Fe, subboundaries were evolved from dense dislocation walls or dislocation tangles, while for the low stacking-fault energy AISI 304 stainless steel, the subboundaries were mainly evolved from planar dislocation arrays and twins. Compareing Balogh's with Lu's conclusions, it seems that there is some discrepancy, though for the latter, the stacking-fault energy spreads in a much wider range than the former.

2.4 Bulk-Metallic Glass

2.4.1 Overview

Metallic glasses usually refer to the specific kind of material, which lacks long-range-order structures on an atomic scale. The first metallic glass of $Au_{75}Si_{25}$ was discovered in 1960 by Duwez at Caltech [103]. At that time, the melting mixture of metal elements must be cooled extremely rapidly (on the order of one megakelvin per second, 10^6 K/s) to avoid the crystallization. Therefore, the first stage of the research on the bulk-metallic glass (BMG) mainly focused on developing new metallic-glass materials with low critical cooling rates and large critical sizes (i.e., good glass-forming ability). When arbitrarily defining the millimeter scale as "bulk", the metallic glass has a millimeter scale in size is often called BMG [104]. Ever since the first bulk PdCuSi-metallic system was prepared by Chen in 1974 [105], BMGs have attracted extensive interests in recent years due to their unique microstructures [106–108], and outstanding mechanical properties, such as high strengths and toughness [14, 109], super hardness [110], and good fatigue strengths [6, 111].

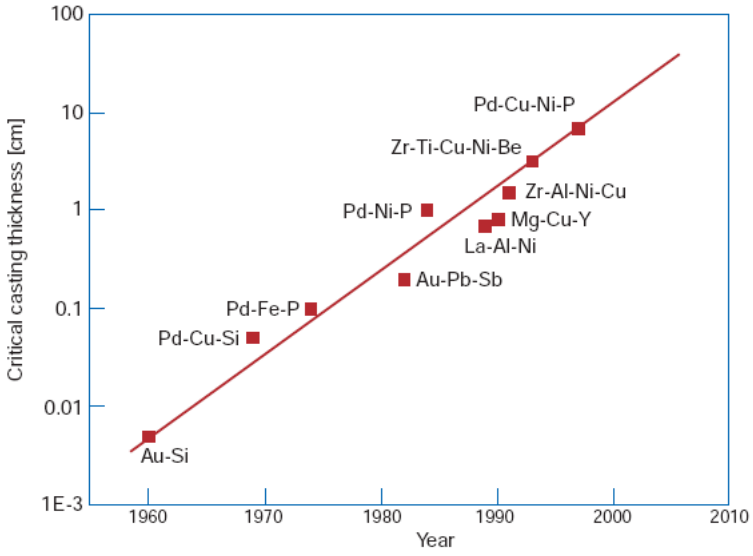

Figure 2.11: Critical casting thickness for glass formation as a function of the year the corresponding alloy has been discovered.

Löffler [112] reviewed the recent research progress on BMG compositions and critical casting thicknesses, and the results were summarized in a plot, which is reprinted below as Fig. 2.11. It is pointed out that the critical-casting thickness tends to increase by one order of magnitude approximately every 12 years. So far, the metallic system, which has the highest glass-forming ability, is the PdCuNiP family. A critical casting thickness of 72 mm was developed in Inoue group in 1997 [112, 113].

In recent years, a considerable amount of theoretical work has been conducted on the microstructures and glass formability for BMG materials. Typical fields include (1) atomistic theory of metallic glasses. e.g., using the atomic pair-density-correlation function (PDF) or free-volume theory to describe the microstructure of the amorphous glasses [111, 114]; (2) atomistic simulations of the microstructures [111, 115]. In contrast, numerous publications have focused on the mechanical properties of the BMGs. Some interesting issues in this field include deformation/crystallization mechanisms, ductility improvement, effects of the residual stresses, and work hardening/softening, etc. Some of the main attractive features of the BMG materials are:

- High strength : $>$ 2000 MPa
- High hardness: 600-1,300 DPH
- High fracture toughness: $>$ 70 MPa·m$^{1/2}$
- High elastic strain: $\sim$ 2% elastic strain
- Good castability and formability: >1000% elongation
- Superior aqueous corrosion resistance
- Good wear resistance
- Excellent soft magnetic properties: Fe-based BMGs
- Other interesting optical and physical properties

In this study, ductility-improvement efforts will be made through the S^{2}PD process, and the microstructural changes induced by this process will also be investigated. Some important issues regarding the plastic deformation of BMGs will first be reviewed in this section.

2.4.2 Plastic deformation and crystallization

Deformation mechanisms of the BMG materials are distinctly different from that of the conventional crystal materials because of their unique "shapeless" structure. In BMGs, since there are no grain boundaries or dislocations, the traditional dislocation theory cannot be used to explain their plastic-deformation behavior. Rather, the deformation of BMGs at room temperature is through the formation of localized shear bands, followed by the rapid propagation of these bands and sudden fracture [111, 116]. After a large amount of work, the inhomogeneous shear-band operation theory has been established and accepted by most researchers [14, 15, 116].

The formation of shear bands has been observed in many deformation processes, such as bending [117], nanoindentation [118, 119], compression [15], and fatigue

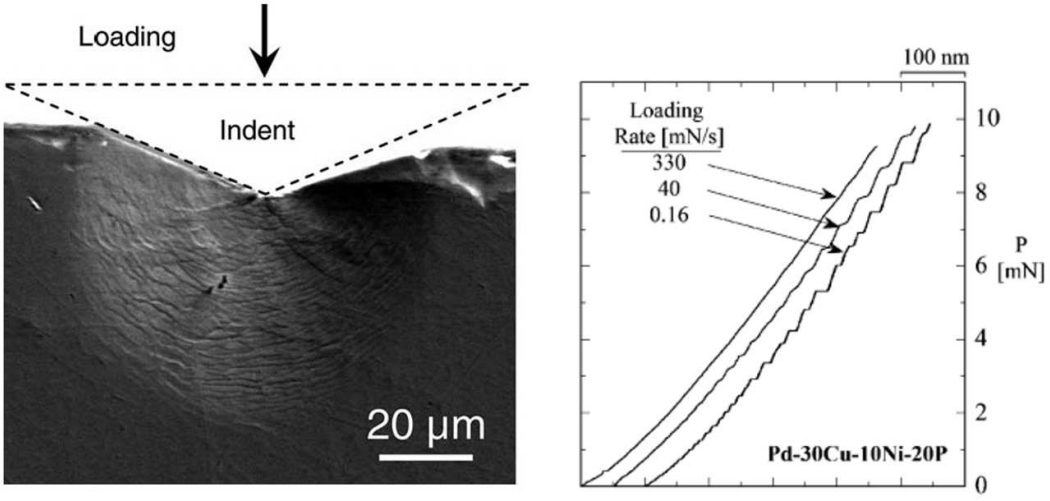

Figure 2.12: Plastic zone and shear-band pattern underneath a Vickers indenter (load = 2000 g) [120]. Plot on the right-hand side is a schematic illustration of the load-displacement curve of a BMG under different load rates.

tests [6]. Figure 2.12 shows the typical shear-band patterns induced by an indentation. It is shown that the shear-band spacing is highly affected by the loading rate, and shear bands are temporally intermittent at the lower strain rate and successive at the higher strain rate. i.e., a low loading rate is corresponding to a smaller shear-band spacing [120]. During the indentation testing, a rate-dependent serrated loading curve is discovered by many researchers, which is also believed to be related to the inhomogeneous shear-band operation [116, 121].

Jiang et al. [120] explained the rate-dependent shear-band behavior in their work, i.e., at the lower strain rate, temporally intermittent shear-banding operations produce a spatially discrete configuration of a few large shear bands, and each shear band may correspond to simultaneous operations of many fine shear bands. However, at the higher strain rate, temporally successive shear-banding operates in front of the plastic zone. A spatially-dense distribution of many fine shear bands takes the place of repeated operations of shear bands at the pre-existing position.

The rate dependence suggests shear banding is a thermally-activated process. Therefore, the formation of shear bands should consist of two consecutive steps: shear-band nucleation and propagation. Schuh et al. [119] proposed that the formation of the shear bands includes the following four steps: (1) activation of single shear-transformation zone (STZ); (2) formation of STZ clusters; (3) shear-band nucleation (nucleus formation); and (4) shear-band propagation.

Detailed TEM observations within the shear bands reveal that during the plastic deformation, the atoms may rearrange themselves and form the ordered nanostructures. For example, Chen et al. and Jiang et al. [122, 123] both observed the crystallization a Al-Fe-Gd system after a bending test, Kim et al. [118] observed nanocrystallites after a nanoindentation test in a Zr-Al-Ti-Cu-Ni system, Chen et al. [124] also reported the crystallization in shear bands in a ZrCu system. It can,, thus, be concluded that in BMGs, one of the consequences of the plastic deformation is nanocrystallization, at least in the systems mentioned above.

However, the operations (including initiation and propagation) of shear bands are usually accompanied by the rise of temperature, which may greatly affect and contribute to the nanocrystallization process. Kim et al. [118] pointed out that very high atomic mobility is required in order to generate nanocrystalines particles within about 10 seconds of indentation. They proposed three possible mechanisms for this transformation, i.e., 1) exchange of atomic positions within shear bands during the large deformation; 2) large rise in the local temperature up to hundreds of degrees; and 3) dynamic flow dilatation (free volumes) in the actively deforming bands attendant dramatic enhancement in the atomic-diffusional mobility. Nevertheless, none of these hypothesis have been confirmed so far, and whether the nanocrystallization is mechanically or thermally induced is still of great interest.

Actually, even for the deformation-induced temperature rise itself (or the temperature within the shear bands), some controversial results were reported. For example, Kim et al. [118] estimated that the temperature is about 0.05 K. Lewandowski et al. [125] believed that the temperature at the center of the shear band is between

3,400 to 8,300 K if the shear band operations are perfectly adiabatic (which can never be the case). Other studies [126–129] reveal that the temperature rise could be between 25 K to 3,175 K. Some authors even asserted that the crystallization process may not be related to the temperature at all. The crystallization in a metallic glass is attributed to the viscous flow rather than the local heating effect [130].

In summary, it seems that only the temperature rise is apparently not enough to cause the nanocrystallization within a very short-time scale (< 0.02 s) determined by a rapid stress drop in serrations. Other factors, such as high shear strains, ultra-high shear strain rates, and excessive free volumes produced by deformation along the shear bands, may also play important roles in the in-situ nanocrystallization [131].

Work hardening and work softening

For crystalline materials, work hardening (or strain hardening) is the strengthening mechanism of a material by plastic deformation, such as tension or cold rolling. From the perspective of microstructures, the plastic deformation has the effect of increasing the dislocation density. The interaction between a large amount of dislocations may, thus, becomes the resistance to the initiation of new dislocations. This resistance to the dislocation formation manifests itself as a resistance to further plastic deformation. In terms of the strength, the materials become stronger after the plastic deformation.

Work softening, on the other hand, occurs under some special conditions: namely, when the plastic deformation in metals or alloys increases to some extent, the strength of the materials no longer increases or even decreases. Since the 1970s, investigations on the mechanisms of work softening of metals and alloys have been reported, and it is believed that the work softening was mainly related to the polygonization recovery at room temperature in a Al-based alloy [132].

For BMG materials, although there are no dislocations, it is interesting to find that work hardening and work softening still exist, i.e., after the plastic deformation,

such as the indentation or compression, it is found that the hardness of the BMG component may increase or decrease. For example, Das et al. [110] developed a new class of metallic glasses, which exhibits a high strength of up to 2,265 MPa together with extensive work hardening and large ductility of 18%, and the work hardening is attributed to the unique structure correlated with the atomic-scale inhomogeneity, leading to an inherent capability of extensive shear-band formations, interactions, and multiplications of shear bands.

Yang et al. [133] also observed the strain hardening and recovery phenomenon in a Zr-Cu-Ni-Al-Ti glassy alloy using a controlled instrumented nanoindentation technique. Within loading rates between 200 and 20,000 μN/s, this phenomenon appears to be independent of the loading rate (or strain rate). Work hardening was explained by the free-volume accumulation and annihilation in amorphous structures.

However, some researchers argued that work hardening of metallic glasses should be interpreted with care, because they actually found that after the plastic deformation, the hardness of the BMG component decreases rather than increases [134]. In Zhang et al.'s [134] work, after a shot-peening process, the hardness along the cross section near the processed surface was found to be decreased, which was attributed to the residual stress. Bei et al. [16] measured the hardness on BMG specimens subjected to different degrees of plastic deformation (in compression tests), it is noted that a systematic strain-induced softening was observed, which contrasts sharply with the hardening typically observed in crystalline metals. A function between the hardness and shear-band spacing is established. Deformation-induced softening leads naturally to the shear localization and brittle fracture.

Work softening was also attributed by some authors to the thermal softening and free-volume-creation softening [135]. It is demonstrated that the free-volume creation and thermal softening can jointly promote the formation of shear bands in BMGs, and the observed post-mortem shear-band width looks more like that governed by the free-volume creation. Figure 2.13 shows the examples of work hardening (left) and work softening (right) in different BMGs from literature.

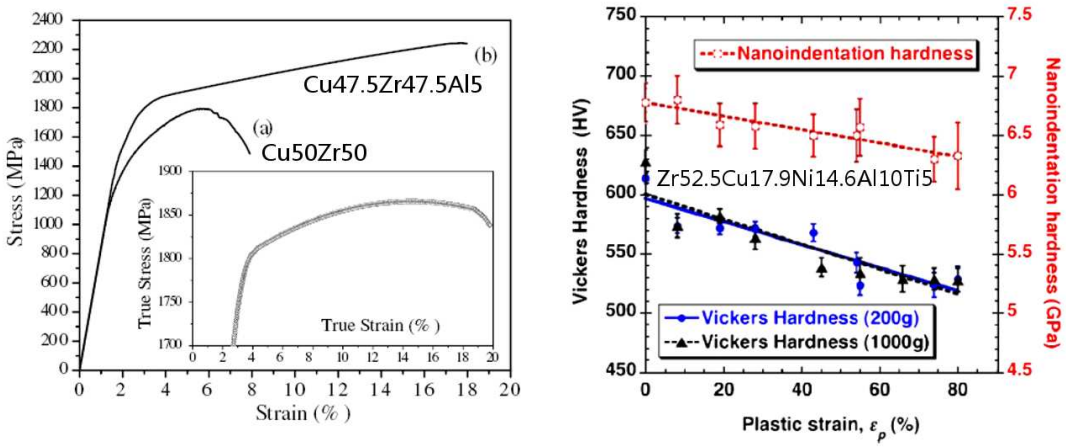

Figure 2.13: Examples of work hardening (left) of $Cu_{47.5}Zr_{47.5}Al_5$ BMG [110] and strain softening (right) of $Zr_{52.5}Cu_{17.9}Ni_{14.6}Al_{10}Ti_5$ BMG [16].

An interesting result is that both work hardening and work softening were observed on the same material. Chen et al. [136] claimed that the nominal hardness could decrease with the pre-existing tensile stress and increase with the pre-existing compressive stress. In other words, the hardness is highly dependent on the status of the residual stress. The finite-element analysis indicates that the strong hardness dependence on the stress results from the large elastic limit of BMGs.

In summary, both work-hardening and work-softening phenomena were observed in metallic-glass components, and preliminary theories have been developed to explain them [136]. For work hardening, the deformation-induced nanocrystals prevent the shear-softening, leading to the arrest of shear bands. To sustain a plastic-deformation rate in a specimen during mechanical testing, new shear bands need to be formed when an active shear band is blocked due to the in-situ nanocrystallization. The nucleation of shear bands prefers to initiate at the weakest sites, such as casting defects (porosities and inclusions) and surface flaws, where highly-concentrated stresses are easily generated. The critical stresses to drive the formation of new shear bands will gradually increase from easy to difficult nucleation sites [131]. For work softening, it is believed that the shear-induced local dilatation may be the source of the observed deformation-induced softening. Due to the coalescence of the excessive free volume, nano-voids may be formed and, in turn, lower the stress required for the

plastic deformation through shear bands, which leads to the observation of reduced hardness [137].

2.4.3 Surface-severe-plastic deformation

Unlike the metals, metallic glasses are usually very brittle, which means that they are easy to fracture before enough plastic deformation could be accumulated. Therefore, there are not many studies, which have focused on the effects of the plastic deformation on the mechanical properties of BMGs. Before the problem can be solved, plastic deformation must be introduced into the BMG component without a fracture failure.

Surface-severe-plastic deformation, such as shot peening, provided an applied way to tackle this problem. A recent work by Zhang et al. [134] showed that the shot-peening process can be successfully applied on a brittle Zr-based BMG component. This surface treatment has been shown to introduce a compressive residual stress into the near-surface layer of the sample, and a decreased hardness on the cross section perpendicular to the processed surface was observed. It is also shown that on the cross section, the residual stress profile and the hardness profile are consistent with each other very well, indicating that the change of hardness might be due to the residual stress.

Raghavan et al. [138] investigated the fatigue behavior of a Zr-based BMG in the as-cast and shot-peened conditions. It is shown that shot peening does not cause a significant enhancement of the fatigue performance of the BMG. Cracks were observed to nucleate in subsurface regions. This trend was attributed to the domination of the compressive residual stress field on the surface over the deformation-induced plastic flow softening that otherwise leads to the easy nucleation of shear bands, which act like microcracks.

Yamamoto et al. [139] conducted the shot-peening treatment on the as-cast $Zr_{55}Al_{10}Ni_5Cu_{30}$ metallic-glass plates for more than 600 s, but no structural evolutions

were induced in the plates according to XRD and TEM experiments. However, a recent work by Méar et al. [140] showed that the shot-peening process may partially relax the structure of the glass, and the peening also increases the atomic mobility.

As a traditional surface-treatment process, shot peening has been developed and applied in industry for over 50 years. However, not many reports have been found regarding the application of this process on the metallic-glasses components. In this thesis work, we are trying to systematically investigate the effects of the surface-severe-plastic-deformation process on the microstructures, thermal properties, and the mechanical properties of a Zr-based BMG component.

CHAPTER 3

Experimental Techniques

3.1 Materials and Equipment

The material used in this work was a Ni-based HASTELLOY® C-2000® superalloy, which was developed to optimize a material for broad applicability. It began with the conceptual idea of adding copper to the well established nickel-chromium-molybdenum (Ni-Cr-Mo) family of alloys. Since its introduction in late 1995, it has gained, and continues to gain, dramatic market acceptance owing to its inherent versatility.

This new material was designed to resist an extensive range of corrosive chemicals, including sulfuric, hydrochloric, and hydrofluoric acids. From an engineering viewpoint, the C-2000 alloy offers significant potential toward the production improvement in plant operations. When used in place of the established Ni-Cr-Mo alloys, the enhanced resistance to corrosion in certain media results in a longer equipment life (for a given thickness of the material), while providing a greater degree of safety during an upset condition.

The main characteristics of the alloy are: (1) tremendous potential industrial applications in automotive, structural, aviation, and storage components; (2) good tensile and fatigue properties compared to stainless steels; (3) a homogeneous face-centered cubic structure with no phase transformation during deformation; (4) outstanding corrosion resistance to many acids (sulfuric acid, hydrochloric acid, hydrofluoric acid, etc.); and (5) low stacking-fault energy, which also means less dislocation mobility.

In this study, the C-2000 alloy was selected because it is expected that the fatigue performance of the material can be improved through the S^2PD process, thus

Table 3.1: Nominal composition of the Hastelloy C-2000 alloy

Nominal chemistry	Ni	Cr	Mo	Cu	C	Si
Weight Percent (wt.%)	balance	23	16	1.6	0.01 Max	0.08 Max

extending its application in a condition where both corrosion and fatigue strength are required. For example, when working as a structure component in the ocean platform, both high corrosion resistance and fatigue resistance of the component are necessary. Another important reason is that this is an alloy with a single-phased face-centered cubic (fcc) structure, and there are no phase transformations during the plastic deformation. Therefore, not like in Lu et al. work [78–80], the effects of new phases introduced by the process can be eliminated and the analysis can be facilitated.

The nominal chemical composition of this alloy is shown in Table 3.1. With the yield strength about 350 $\sim$ 400 MPa, elongation around 60 to 70%, and density about 8.5 g/cm^3, the material was supplied by the Haynes International Inc. in the form of a 3.22-mm-thick sheet (an as-received sheet), which was cold-rolled to the final thickness and followed by annealing at 1,120 $^\circ C$ for a complete recrystallization.

The equipment used to perform the S^{2}PD process is a dual-clamp 8000D Mixer/Mill, as shown in Fig. 3.1. Round disc samples were used as a cover of the cylindrical container, which seals the WC/Co balls inside. The shaking action of a SPEX SamplePrep Mixer/Mill is both complex and forceful. As the vial is swung back and forth in a shallow arc, its ends are displaced laterally in a "figure-8"; this arrangement distributes the ball impact over wide areas of the samples. Because the SPEX SamplePrep Mixer/Mill clamp movement is extremely rapid, the balls develop high G-forces, which, thus, cause high strains and high strain rates in a short time on the near-surface layer of the sample.

The as-received plate was first cut as round discs with a diameter of 50 mm. Before the S^{2}PD process, the discs were first cleaned with acetone and then ethanol. After cleaning, the discs were treated with the S^{2}PD process under an argon

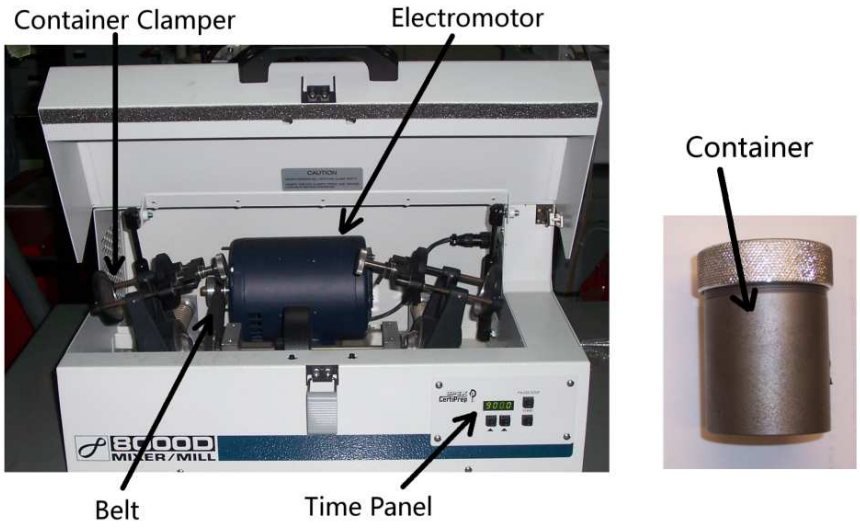

Figure 3.1: SPEX SamplePrep Mixer/Mill was is used to perform the S^2PD process, the right-hand side is the cylindrical container, where the round sample is used as a cover to receive the bombardment of the balls.

atmosphere using a Spex 8000 mill. The disc was held in place via mechanical locking at one end of the cylindrical steel container of the Spex mill and five WC/Co balls (with a composition of 94 wt.% WC + 6 wt.% Co) either 4.9 mm or 7.9 mm in diameter were used to provide the desired impact on the surface of the C-2000 plate. The impact velocity of WC/Co balls induced by shaking the steel container of the Spex mill was about 5 m/s. The processing parameters of the S^2PD treatment are summarized in Table 3.2. During the process, in order to limit the overall temperature of the sample, the bombardment were intermitted every 15 minutes on purpose to cool down the bombardment system.

The second part of this work is to apply the same process on a BMG material. The material selected was a Zr-based $Zr_{50}Cu_{40}Al_{10}$ (in atomic percent) BMG. This is one of the earliest developed BMGs with mechanical and thermal properties being almost thoroughly investigated. The basic properties are: a glass-transition temperature of Tg = 706 K, crystallization temperature of Tx = 792 K, and liquidus temperature of Tl = 1,092 K, yield strength of σ_y =1.86 GPa, Modulus of E = 88 GPa, and Elongation of e = 2.1%.

As shown above, the BMG material has shown super mechanical properties, such as high yield strength, high toughness, and high hardness. However, the ductility of BMGs is not so good, compared to industrial specifications. In this experiment, we are trying to introduce plastic deformation into this brittle material, and seek the possibility of improving the ductility and fatigue behavior of the BMG. The material used in this work is a Zr-based $Zr_{50}Cu_{40}Al_{10}$ BMG, which was prepared by arc-melting mixtures of pure Zr, Cu, and Al metals in an argon atmosphere. A low-oxygen-concentration Zr (< 0.05 at.% oxygen) rod was used to minimize the oxygen content in the alloy. A tilt-casting method was implemented to cast the alloy to its final rod shape of 60 mm in length and 8 mm in diameter [141].

Although the process is the same for both the crystalline and the amorphous specimens, there are some minor differences in details. Firstly, unlike crystalline materials, the BMG sample has a size limit. For example, for the $Zr_{50}Cu_{40}Al_{10}$ sample, the maximum diameter is around 14 mm. Therefore, it is impossible to fabricate the sample disc with a diameter of 50 mm, as does for the C-2000 plate. Secondly, the BMG is much more brittle than the C-2000 alloy, which means it is easy to break the sample if the impact impulse is too high. Therefore, the processing energy must be tuned carefully. Thirdly, since the structure of BMGs is very sensitive to the temperature, controlling the temperature rise during the impact process is much more important for BMG samples than for crystalline samples.

Due to the difficulties mentioned above, an alternative of the sample process design was proposed and successfully applied on the BMG samples. The schematic illustration of the sample fixture is shown in Fig. 3.2. On the original cover of the container, a secondary cover with a rectangle dent is attached mechanically. Five BMG bars, each with dimension of $3 \times 3 \times 25$ mm^3, were put inside the dent, and the BMG bars are fixed by two fasten screws which could push the bars together. The height of the bars is exactly the depth of the dent, and, therefore, the whole surface is still flat.

Table 3.2: Processing parameters for the S^2PD process

Sample ID	Ball Material	Number	Diameter (mm)	Time (min)
L30	WC/Co	5	7.9	30
L60	WC/Co	5	7.9	60
L90	WC/Co	5	7.9	90
L120	WC/Co	5	7.9	120
L180	WC/Co	5	7.9	180
M30	WC/Co	5	4.9	30
M60	WC/Co	5	4.9	60
M90	WC/Co	5	4.9	90
M120	WC/Co	5	4.9	120
M180	WC/Co	5	4.9	180
S30	WC/Co	20	1.6	30
S60	WC/Co	20	1.6	60
S180	WC/Co	20	1.6	180

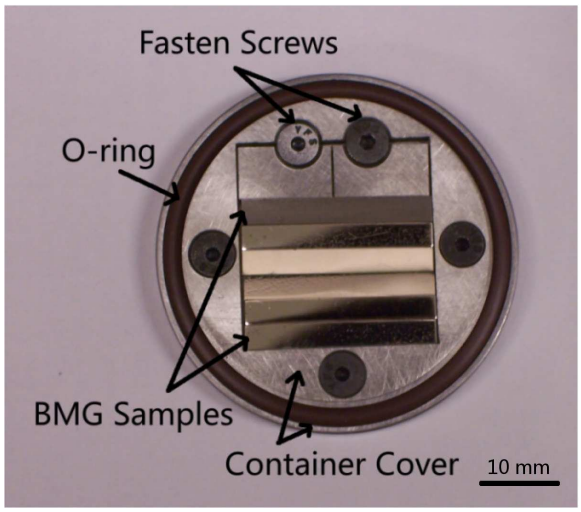

Figure 3.2: Experiment setups for the BMG samples. The BMG bars are fastened together by the screws and the whole surface is flat, so that the WC/Co balls could impact the surface evenly.

3.2 Experimental Procedures

3.2.1 Microstructures and fractography

Grinding and polishing

Before the S^{2}PD process, both the C-2000 (cut to round discs with a diameter of 50 mm) and the $Zr_{50}Cu_{40}Al_{10}$ BMG (cut to rectangular bars with a dimension of $3\times 3\times 25$ mm^3) samples were subjected to the grinding and polishing process, which was conducted on a Buehler Eomet Variable-Speed Grinder-Polisher. The samples were first ground using 180, 240, 360, 400, 600, 1,200, and 2,400 grit papers in succession. Between each step, the sample was rotated 90° to remove the previous scratches. Polishing was performed in two consecutive steps, first using a 6-μm diamond paste on a nylon cloth and, then, a 0.05-μm alumina paste on a micro-cloth.

OM, SEM and TEM

The microstructures of the as-treated surface and fatigue-fracture cross-section were characterized by the optical microscopy (OM), scanning-electron microscopy (SEM), X-ray diffraction (XRD), and transmission-electron microscopy (TEM). TEM samples at certain depths away from the specimen surface were obtained by: (1) first mechanically polishing on two sides until the sample reached a 20-μm thickness, and (2) finally thinning by a two-side jet with a solution of the 5% perchloric acid and 95% ethanol (in vol.%, volume percent) at 10 °C. X-ray diffraction experiments were implemented on a Philips X'pert Diffractometer and Cu K_α ($\lambda_{K_{\alpha 1}} = 0.154056$ nm and $\lambda_{K_{\alpha 2}} = 0.154439$ nm) radiation was used. The as-treated samples were cut to a 20×20 mm^2 square shape, and the surfaces were scanned with a continuous-scanning mode at a rate of 1.5°/min.

To measure the residual stress caused by the S^{2}PD process in the C-2000 sample, a layer-by-layer electro-polishing process was used to remove the sample

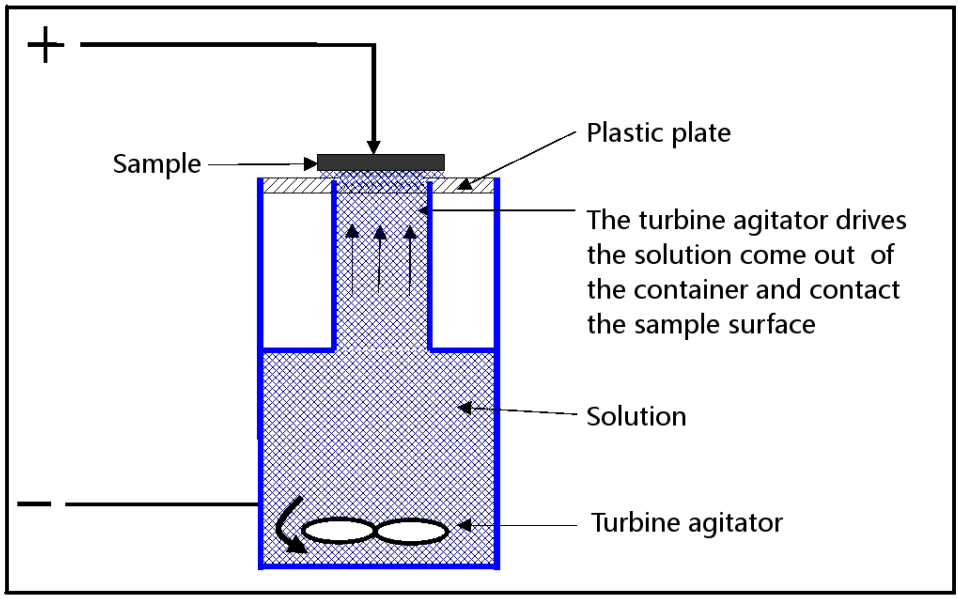

Figure 3.3: Illustration of the electro-polishing process.

surface layer by layer. A schematic illustration of the equipment used in this study is shown in Fig. 3.3. The solution, which has a composition of 7.8% Perchloric Acid, 10% Butyl cellosolve, 73.0 % Ethanol, and 9.2% Distilled water, in volume percent, is ejected out and contacts the sample surface by the rotation of the turbine inside the container. Positive and negative electrodes are connected to the sample and the container wall, respectively. The plastic plate, with a round hole in the center to let out the solutions, were used to support the sample. The whole plate, thus, has a relatively homogeneous polishing rate except for the sample corners. However, since the sample has a dimension of 20×20 mm^2, which is large enough for an XRD experiment, only the center part of the sample will be subjected to the scan, and the effects of the unpolished corners will be ignored in this study.

Synchrotron

A synchrotron high-energy X-ray diffraction experiment was conducted at the 11-ID-C beamline of the Advanced Photon Source (APS), Argonne National Laboratory, for inspecting the minor crystal phase contained in the samples. The beam size used is 400 μm (parallel to the treated surface) $\times$ 20 μm (along the normal direction

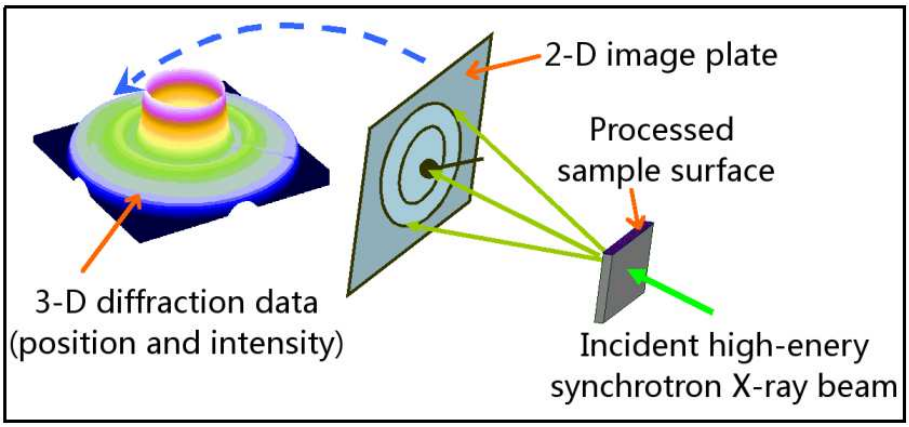

Figure 3.4: Schematic illustration of the synchrotron diffraction, the left-most 3-D image is a typical result from a synchrotron X-ray diffraction, where the height of the peaks is corresponding to the diffraction intensity at that X-Y position, and the colors are arbitrarily selected to represent different intensity ranges.

of the treated surface), and the wavelength is 0.107560 Å. A two-dimensional (2-D) image plate, Mar345, was used as the area detector for collecting the diffraction patterns. The synchrotron sample was cut from the processed bar and had a geometry of $2 \times 2 \times 1.5$ mm^3, with the thickness, 1.5 mm, along the longitude direction of the bar. Diffraction data from the treated surface to the less-affected interior are collected and compared. It should be noted that the high-energy X-ray diffraction technique used in the present investigation provides a very powerful and sensitive tool for characterizing a tiny volume of the crystalline phase among the amorphous matrix, due to the high flux and high resolution of the high-energy X-ray beam produced by a synchrotron source and the 2-D area detector used in the present technique, respectively. A schematic illustration of the synchrotron-diffraction experiment setup is shown in Fig. 3.4.

DSC

For the BMG sample, differential-scanning calorimetry (DSC) is an important method to characterize the thermal property of the material. Sample pieces with a dimension of 2 $\times$ 2 mm^2 and thickness 0.3 mm, which were cut from the treated

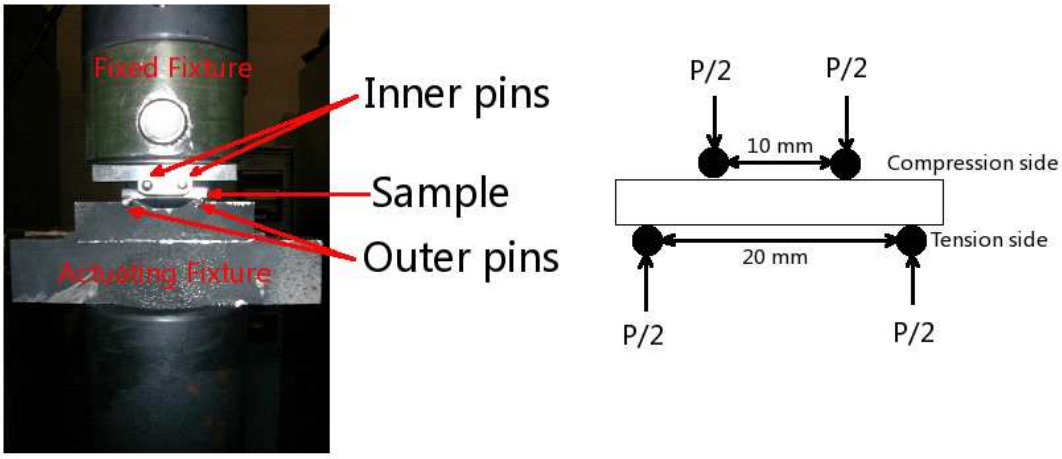

Figure 3.5: Pictures of the four-point-bending-fatigue test equipment and schematic illustration of the four-point-bending test.

surface and carefully polished to its final shape, were used to measure the thermal properties of the deformed specimens in a Perkin-Elmer Diamond DSC at a heating rate of 30 K/min under a constant flow of high-purity argon. XRD analyses were conducted using a Philips's X'pert diffractometer to characterize the near-surface structure of the specimen before and after the S^2PD process.

3.2.2 Mechanical properties

Four-point-bending fatigue

The fatigue behavior of the samples is studied by the four-point-bending test. In this loading mode, the sample surface (bending side) between the two inner pins is subjected to the maximum and constant bending moment, and the fatigue crack usually initiates on this region. Therefore, this test is suitable for testing the surface-crack-initiation resistance. The test equipment and the geometry of the fixture are shown in Fig. 3.5. The distances of the inner and the outer pins are 10 mm and 20 mm, respectively. The specification of the four-point-bending fatigue test can be found on the American Society for Testing and Materials (ASTM) C 1211-92 Standard Test Method for Flexural Strength of Advanced Ceramic at Elevated Temperature [142].

Four-point-bending-fatigue experiments were conducted on a computer-controlled Msterial Test System (MTS) servohydraulic testing machine with a fixed R ratio (where $R = \sigma_{min}/\sigma_{max} = 0.1$, where σ_{min} and σ_{max} are the applied minimum and maximum stresses, respectively) and different stress levels. Using a load-controlled bending-fatigue test, the nominal stress, σ_{nom}, has the following relationship with the applied load:

$$\sigma_{nom} = \frac{3P(L-t)}{2Wh^2} \tag{3.1}$$

where σ_{nom} is the nominal stress, P is the total load applied, L and t are the distance between two outer and two inner pins, respectively; while W and h are the width and height of the rectangular samples, respectively.

Surface roughness

The NewView 5000 was employed to measure the surface roughness. It is based on the scanning white-light interferometry, an innovative technique, in which a pattern of bright and dark lines (fringes) results from an optical-path difference between a reference and a sample beam. Incoming light is split inside an interferometer, one beam going to an internal reference surface and the other to the sample. After the reflection, the beams recombine inside the interferometer, undergoing constructive and destructive interference and producing the light and dark fringe pattern. A precision vertical scanning transducer and camera together generate a three-dimensional (3-D) interferogram of the surface, processed by the computer and transformed by frequency-domain analyses, resulting in a quantitative 3-D image of fracture-surface roughness [143].

Microhardness and nanoindentation

Samples for microhardness measurements were first ground using SiC grit papers. Then, polishing was performed in two consecutive steps, first using a 6-μm

diamond paste on a nylon cloth, and, then, a 0.05-μm alumina paste on a micro-cloth. A Buehler Vickers-hardness tester was used to measure the microhardness distribution along the cross sections from the surfaces to the interiors of the samples. The applied force was 300 gf (i.e., 2.94 N), or 100 gf (i.e., 0.98 N) in some cases. The distance between successive indents was 30 μm.

For the BMG material, a nanoindentation test was conducted to investigate the deformation performance of the processed sample. The tests were conducted on both the processed surface and the side surface. Therefore a hardness profile from the deformed surface to the unaffected interior can be established. The nanoindentation was conducted in a load-controlled mode employing a computer-controlled Nano Indenter® XP system equipped with a Berkovich indenter. Data acquisitions and analyses were done in TestWorks® 4 Software for Nanoindentation Systems (MTS Systems Corporation). The calibration to a polished, single-crystal aluminum standard was performed prior to the measurements. A 10-gf (i.e., 0.098 N) load was applied in each test, and the measurement was along multiple lines beginning approximately 10 μm from the processed surface and extending approximately 1 mm into the center of the material. Additional indents were made in the near-surface region. The average indent depth was approximately 900 nm.

Tensile property

The S^2PD-processed plates were cut into dogbone tensile specimens with a rectangular cross-section (3.3 mm $\times$ 3.2 mm) and a gage length 12.7 mm. Tensile tests were conducted on an MTS 810 test machine with a displacement control, and an extensometer was used in all the tensile tests to measure the strain. The extensometer was installed after the tensile specimen was pre-loaded with a 10 lb force (i.e., 44.48N). After the installation of the extensometer, the sample was deformed at a starting strain rate of 0.05 /min. The geometry of the tensile sample is schematically illustrated in Fig. 3.6. It should be pointed out that in this study, both sides of the

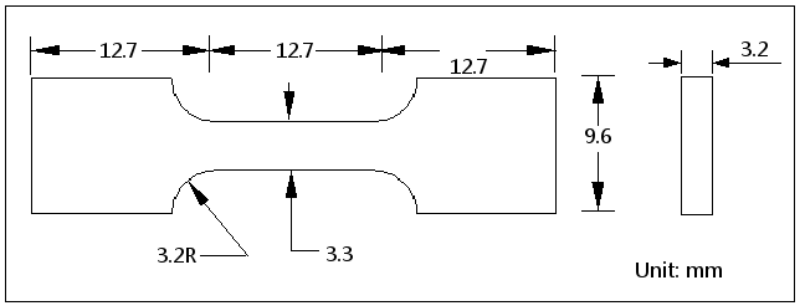

Figure 3.6: Geometry of the tensile sample, please note that in this study, both sides of the sample have been subjected to the S^2PD process.

plate (therefore both sides of the processed tensile samples) were subjected to the S^2PD process.

3.3 Summary

In this chapter, the sample compositions, preparation methods, and the S^2PD process were introduced briefly. The investigation techniques, which were utilized in characterizing the microstructures and the mechanical properties of the specimens, are also described. For the mechanical properties, the study focused on the microhardness, tensile behavior, and fatigue performance. Due to the importance of the residual stress in affecting the mechanical properties, the characterization method of residual stress is presented in detail.

CHAPTER 4

Dependence of Microstructures of a C-2000 Superalloy on the Processing Condition of the S^2PD Process

4.1 Introduction

Nanocrystalline (nc) and ultrafine-grained (UFG) materials have drawn considerable attentions and great interests in recent years because of their superior mechanical properties, such as high strengths and hardness, remarkable superplasticity, and excellent resistances to wear and fatigue-crack initiation, compared to their coarse-grained counterparts [62, 77, 144, 145]. However, an effective fabrication method of ideal bulk nano-structured materials is still a challenge because of the contamination and porosity issues [62, 77, 144–146]. Since most failures of components, including fatigue fractures, fretting fatigue, and wear failures, are very sensitive to the structures and properties of their surfaces, the surface-nanocrystallization process provides a feasible approach to improve the performance of the material and to investigate the formation mechanism of nano-grains near the surface.

Surface-severe-plastic deformation (S^2PD) is an important surface-nanocrystallization process that has recently been developed to introduce nano-grains and grain-size gradients in the surface layer of bulk materials. There are several variants of such S^2PD-based techniques, including the ultrasonic shot peening (USSP) [82, 83], high energy shot peening (HESP) [85], surface mechanical attrition (SMA), or surface mechanical attrition treatment (SMAT) [78, 147, 148], and surface nanocrystallization and hardening (SNH) [87, 149–151]. These S^2PD-based techniques have been shown to improve the tensile strength [85], microhardness [149], and wear resistance [84, 90] of materials. Recently, improvements in the fatigue resistance have been demonstrated

using the SNH process [88]. These results unambiguously indicate that S^2PD-based techniques are alternative approaches to enhance the surface properties and upgrade the global properties of engineering materials with no changes in chemical compositions, as the physical-vapor-deposition (PVD), chemical-vapor- deposition (CVD), or other coating processes do.

In the present research, the fatigue behavior of the HASTELLOY C-2000®* alloy processed under different SNH conditions is investigated in order to find out how sensitive the fatigue resistance of the C-2000® alloy is response to the SNH process. The alternation of the fatigue resistance as a function of the SNH processing condition has been related to the changes in work hardening, nano-grain formation, residual-compressive stresses, surface roughness, and surface contamination. Based on these results, the implications of this study and future work are discussed. The details of this study are presented below.

4.2 Experimental Procedures

4.2.1 Surface-treatment process

The material used in this work was a Ni-based HASTELLOY C-2000® superalloy (cold-rolled and fully annealed at 1,120 $^{\circ}C$) with a nominal chemical composition (in weight percent) of 23Cr, 16Mo, 1.6Cu, 0.01C, 0.08Si, and balanced Ni. After cleaning with the acetone and, then, ethanol, the as-received sample disc with a thickness of 3.2 mm and a diameter of 50 mm was held via mechanical locking at one end of a cylindrical steel container of the Spex mill. Five WC/Co balls, which have a composition (in weight percent) of 94% WC and 6% Co, were subsequently put into the steel container to provide the desired impacts on the surface of the sample. The diameter of the WC/Co balls used in this experiment is either 4.9 mm or 7.9 mm. The impact velocity of WC/Co balls induced by shaking the steel container was about 5 m/s. The processing periods were 30, 60 and 180 min, and 4.9 mm balls were used to treat the 60-min sample while 7.9-mm balls were used for the 30-

*HASTELLOY and C-2000 are registered trademarks of Haynes International, Inc.

and 180-min samples. The samples were, then, given the ID number as L30, L180, and M60, respectively, where L represents "large", and M represents "medium". The whole process was conducted in an argon atmosphere.

4.2.2 Structure characterizations

The energy-dispersive X-ray spectrum (EDS) spectra and EDS mapping were employed to study the distribution of the contaminant, tungsten carbide, induced by the impacts of WC balls on the processed surface. A Philips X'Pert X-ray Diffractometer with a Cu K_α ($\lambda_{K_{\alpha1}} = 0.154056$ nm and $\lambda_{K_{\alpha2}} = 0.154439$ nm) radiation was used to determine the phase constitution on the surface region. Meanwhile, the values of the full width at the half maximum (FWHM) obtained from the X-ray diffraction (XRD) were used to estimate the grain size and micro-strains on the surface of the SNH-processed sample. Specifically, the peak broadening was attributed to nano-grains, internal strains, and instrumental broadening [36]. The FWHM of the sample peak, $\beta_g(2\theta)$, which excludes instrumental broadening, can be calculated with the following equation [36]

$$\beta_g^2(2\theta) = \beta_h^2(2\theta) - \beta_f^2(2\theta) \tag{4.1}$$

if it is assumed that the instrumental and the sample peak functions are both Gaussian in nature. The $\beta_h(2\theta)$ in Eq. 4.1 is the FWHM measured from the sample with the SNH treatment, $\beta_h(2\theta)$ is the one from the standard, and θ is the Bragg angle. The FWHM of the untreated sample can be used as the standard in this method. Once $\beta_g(2\theta)$ of the low-angle reflections is found from Eq. 4.1, it can be employed to estimate the average grain size, D, of the Ni surface with the aid of the Scherrer formula [94]

$$\beta_g(2\theta) = \frac{0.9\lambda}{D\cos(\theta)} \tag{4.2}$$

where λ is the wave length of the X-ray radiation.

Similarly, the FWHM of high-angle reflections computed from Eq. 4.1 was utilized to estimate the effective internal strain, 2ξ, within the face-centered cubic Ni

crystal, using the Stokes and Wilson formula [36]

$$\beta_g(2\theta) = 2\xi \tan\theta \tag{4.3}$$

The estimation of grain sizes and effective internal strains of severely-plastically deformed samples using Eqs. 4.2 and 4.3 can give fairly good approximations, because the broadening at low-angle reflections mainly relates to the grain size, and the broadening at high-angle reflections is predominately determined by the internal strain [95, 96]. Recently, a detailed XRD analysis [97], using the Rietveld method in conjunction with the Levenberg-Marguardt non-linear least-square fit (LM-fit) and line-broadening analysis, demonstrates that this is indeed the case for nanocrystalline Al alloys that have been subjected to severe-plastic deformation.

A NewView 5000 interferometer was employed to measure the surface roughness of the samples. It utilized the scanning white-light interferometry, an innovative technique, in which a pattern of bright and dark lines (fringes) results from an optical-path difference between a reference and a sample beam. The incoming light was split inside an interferometer, one beam going to an internal reference surface and the other to the sample. After the reflection, the beams recombined inside the interferometer, undergoing the constructive and destructive interference and producing the light and dark fringe pattern. A precision vertical scanning transducer and camera together generated a three-dimensional (3-D) interferogram of the surface, which was processed by the computer and transformed by frequency-domain analyses, resulting in a quantitative 3-D image of the fracture-surface roughness.

In the characterization methods mentioned above, Ra represents the arithmetic-mean value, which is the average value of the departure of the profile from the center line throughout the sampling length. It should be pointed out that the Ra value over one sampling length represents the average roughness. Therefore, the effect of a single spurious non-typical peak or valley within the profiles trace will be averaged out and, as such, has only a small influence on the Ra value. Ra also offers no distinctions between peaks and valleys on the surface trace. On the other hand,

the root-mean square (rms) is another method, which uses the statistical method to calculate the average roughness. The rms can be obtained by squaring each value, then taking the square root of the mean. When compared to the arithmetic average, rms has the effect of giving extra weight to higher values. The PV value represents the average peak-to-valley height (maximum roughness), which does not consider the overall profile changes, i.e., there is no center line. A detailed descriptions of the roughness can be found in literature [152], and the equation used for the calculation of the roughness is presented here:

$$R_a = \frac{1}{l_m} \int_{x=0}^{x=l_m} |Z(x)|\, dx \tag{4.4}$$

$$rms = \sqrt{\frac{1}{l_m} \int_{x=0}^{x=l_m} Z^2(x) dx} \tag{4.5}$$

$$PV = \frac{1}{n}(Z_1 + Z_2 + Z_3 + \cdot + Z_n) \tag{4.6}$$

where l_m is the length that measured for roughness, Z_x is the height of a certain point on the surface to the reference point, and n is the number of peak-valley pairs in the indicated length, l_m.

Microstructures of the as-received and processed samples were investigated, using Optical Microscopy (OM), scanning-electron microscopy (SEM), and transmission electron microscopy (TEM). The cross-sectional OM specimens were first mechanically ground and polished, and, then, electrolytically etched at room temperature in a solution composed of 5 g oxalic acid and 95 ml hydrochloric acid with a d.c. voltage of 6 V. TEM samples at different depths away from the surface were obtained by: (1) first mechanically polishing on one or two sides of the sample until the sample reached a 20-m thickness, and (2) finally thinning using a two-side jet with a solution of the 5% perchloric acid and 95% ethanol (in volume percent) at 10 $^{\circ}C$.

4.2.3 Characterization of macroscopic residual stresses and mechanical properties

The sign of macroscopic residual in-plane stresses parallel to the plane of the C-2000 plate was qualitatively determined via the bending direction of the plate after the SNH process. To achieve this, only one side of the plate was SNH-processed. After processing, the processed plate was unclamped from the Spex mill, and its radius of curvature was measured using a Gage Master Series Twenty optical comparator coupled with a Gage Master GMX electronic processing unit (Gage Master Corporation, Rancho California, CA). This instrument projects the silhouette of the plate onto a screen along with a coordinate system that permits the measurement of (x, y) points along that silhouette. The radius of curvature of the SNH-processed plate was calculated by fitting the (x, y) points to a circle. Three such estimates were made for the specimen by rotating the plate about its symmetry axis with a 60-degree increment between two adjacent measurements. The average of these three estimates was reported as the radius of curvature.

A Buehler Vickers-hardness tester was used to determine the microhardness distribution along the polished cross sections from the surfaces to the interiors of the samples. The distance between two successive indents was 30 μm, and the applied force was 300 g with a dwell time of 15 seconds. Each microhardness value reported was the average of 5 indentations. The C-2000 plates with the SNH treatment on both sides of the plates were used for the measurement of the fatigue resistance. The dimensions of the fatigue samples were $25 \times 3.2 \times 3.2\text{mm}^3$ so as to conform to the American Society for Testing and Materials (ASTM) C1211-92 Standard Test Method for Flexural Strength of Advanced Ceramics at Elevated Temperature.

Four-point-bend fatigue experiments were conducted on an MTS 810 electro-hydraulic machine at room temperature. The distance between the two inner pins and two outer pins are 10 and 20 mm, respectively. The tests were performed with a fixed R ratio (where $R = \sigma_{min}/\sigma_{max} = 0.1$, σ_{min} and σ_{max} are the applied minimum and maximum stresses, respectively) and different stress levels. Using a load-controlled

bending-fatigue test, the nominal stress, σ_{nom}, has the following relationship with the applied load:

$$\sigma_{nom} = \frac{3P(L-t)}{2Wh^2} \tag{4.7}$$

where σ_{nom} is the nominal stress , P is the total load applied, L and t are the distances between two outer and two inner pins, respectively; while W and h are the width and height of the rectangular sample, respectively. The fatigue test was terminated if the sample survived 5×10^6 cycles, and the corresponding maximum stress was taken as the fatigue strength.

4.3 Results

4.3.1 Surface contamination and surface roughness

Figure 4.1 shows the XRD spectra of the as-received and SNH-treated specimens. On the spectrum of the as-received sample, there are no other peaks except those of the Ni alloy itself, since no treatments were carried out. While on the surfaces of the treated samples, some diffraction peaks other than face-centered-cubic (fcc) Ni alloy appear, which are shown to belong to the hexagonal-structured tungsten carbide (WC). Furthermore, with the increase of the treatment time and/or ball size, the intensities of these peaks increase evidently. This result illustrates that the surface WC contamination becomes severe with the increase of the process time and/or ball size. Therefore, it can be deduced that during the SNH treatment, cold welding and fretting fracture between the sample surface and the WC balls occurred. When the balls bounced away from the surface, some of the material on the ball surface was left on the sample surface. A larger ball size and a longer treatment time made this effect more pronounced.

The surface morphology and element constitutions measured by the SEM/EDS mapping, and EDS spectra are shown in Fig. 4.2. Obviously, the S^2PD process roughed the polished surfaces regardless of the process time. From the SEM picture of Fig. 4.2(a), it can be seen that the surface of the as-received sample is relatively smooth and clean (although there are still some small dents caused by the polishing

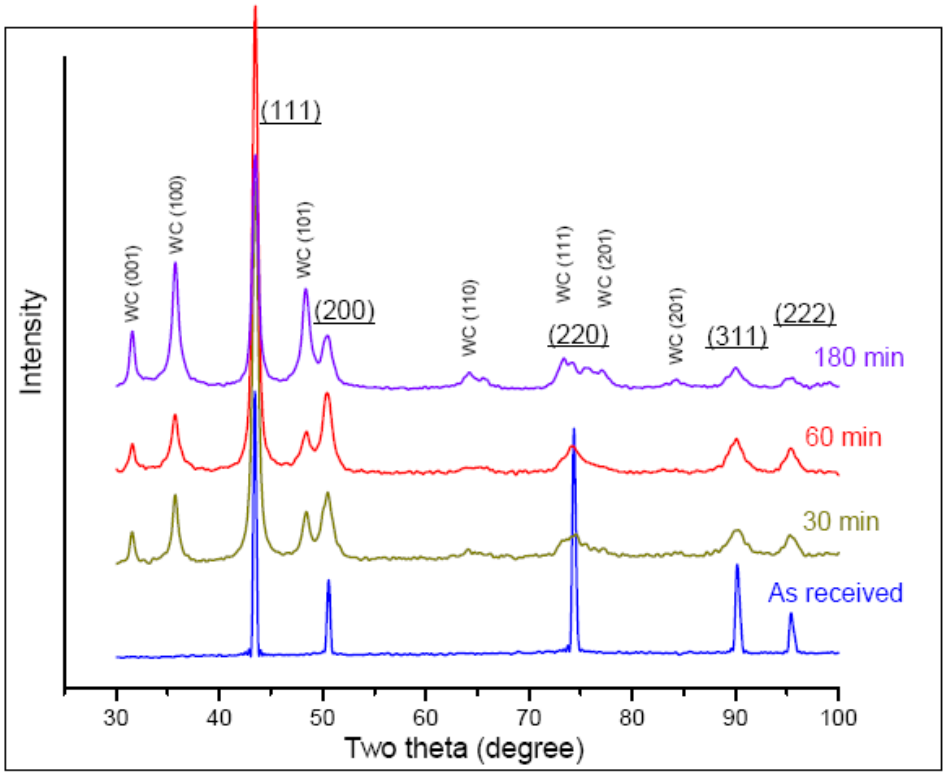

Figure 4.1: XRD spectra show the contamination of the processed sample surface.

SiC particles), but those of the SNH-treated samples are quite rough, as shown in Figs. 4.2(b), (c), and (d) for samples treated 30 (sample L30) and 180 min (sample L180) with 7.9-mm balls, and 60 min with 4.9-mm balls (sample M60), respectively. An interesting result here is that it is noted that L30 [Fig. 4.2(b)] shows the most rough surface, not the other two. A quantitative analysis, which will be shown later, confirms that this observation is really the case. Therefore, we can conclude that the roughness increases with the processing time first, and, then, decreases when the processing time further increases. The possible reason will be discussed later.

From Fig. 4.2, it is noted that in the processed surface, it seems that materials pieces in some region do not seem to be consistent with others in the processed samples, as indicated by the arrows. EDS-mapping experiments were, thus, done to investigate the composition of the sample surface. The results are shown in Fig. 4.3. Here only the mapping of the processed samples are shown. In Fig. 4.3, the green color represents the Ni distribution on the surface, while the red color stands for the

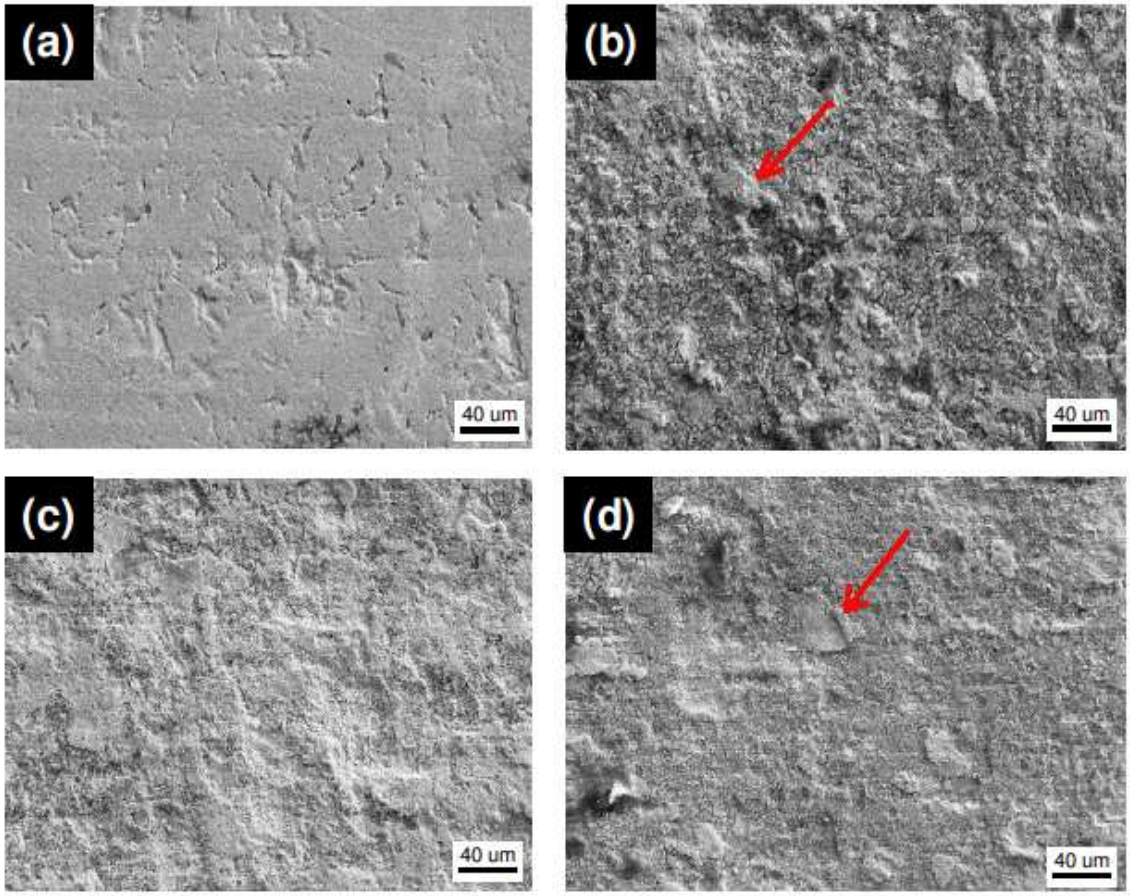

Figure 4.2: SEM observations of the sample surfaces show that surface roughness has changed by the S^2PD process, while the as-received sample (a) is flat and smooth, the 30 min (b), 180 min (c) with 7.9-mm balls and 60 min (d) with 4.9 mm balls samples are relatively rough, and the 30-min sample shows the highest roughness.

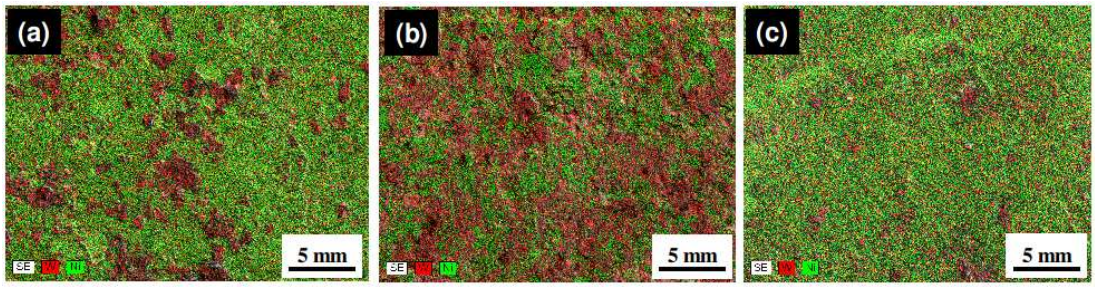

Figure 4.3: EDP mappings of the processed samples. It is shown that sample L30 (a), L180 (b), and M60 (c) were contaminated by the WC during the bombardments, and L180 has the largest amount of W contaminations.

tungsten distribution from the fragments of the WC, which is believed to be from the WC/Co balls during the bombardment. Figs. 4.3(a), (b) and (c) represent specimen, L30, L180, and M60, respectively.

Apparently, on the surface of sample L180 as shown in Fig. 4.3(b), the WC fragments almost covered the entire surface, since it a large portion of red color can be seen. It is not surprising to observe that the longer processing time generates more WC contamination when the ball sizes are the same. For samples L30 and M60, the amount of WC is obviously less than that of L180. Comparing samples L30 with M60, less WC is presented in the latter. Note that the L30 is processed with 7.9-mm balls, while M60 was processed with 4.9-mm balls, thus, the ball size has larger influence on the cold welding and fretting fracture between the sample and the balls than the processing time.

In order to inspect the composition of the contamination on the surface, EDS scanning was performed on the sample surfaces, and resulted spectra are shown in Fig. 4.4. It can be noted that the surface of the as-received sample does not contain any tungsten, while the other three treated samples do. This result is consistent with the observed mapping results. The new information here is that the contamination is not only W, but also caused by Fe, which is believed to be from the steel contain. As the processing time increases, the contamination problem becomes more severe and obvious.

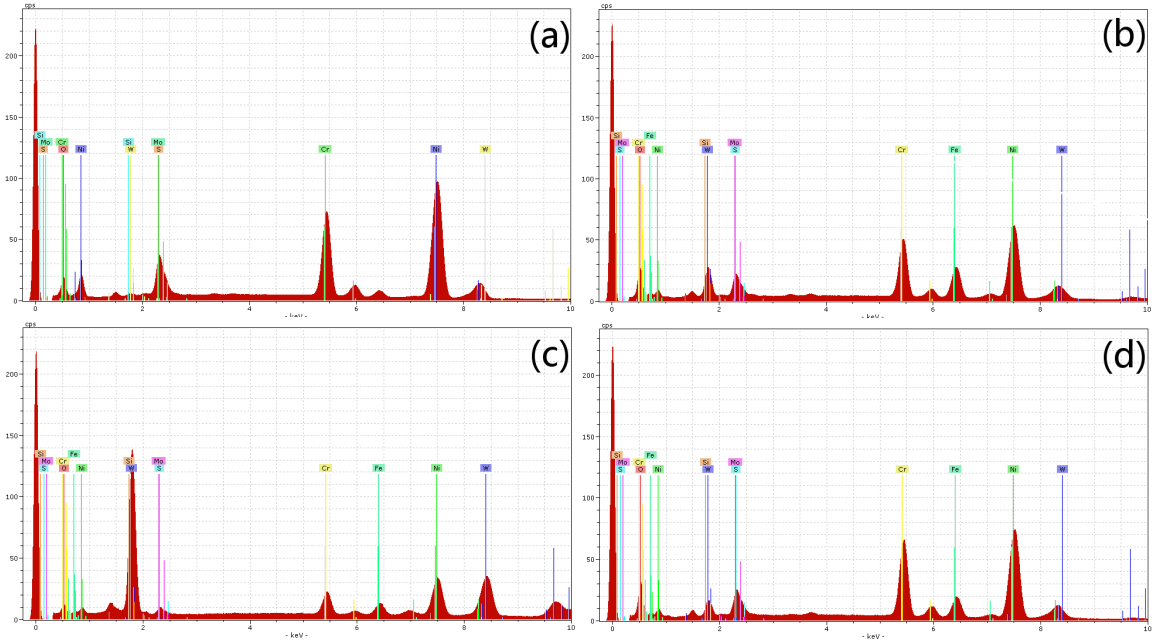

Figure 4.4: EDS scanning spectra of the sample surfaces. The as-received sample (a) shows no sign of contamination, while L30 (b), L180 (c) and M60 (d) were contaminated during bombardment, it is also shown that Fe was introduced in the surface layer.

Table 4.1: Quantitative roughness values

Sample ID	PV (μm)	rms (μm)	Ra (μm)
As-Received	7.98	0.52	0.41
L30	39.78	6.84	5.50
L180	37.86	4.69	3.64
M60	36.73	5.51	4.42

Actually, the composition of the elements on the surface can be quantified by the EDS. It is shown that the sample treated 180 min has the highest tungsten content (average 15.91 at.%, atom percent), while the sample treated 60 min has the lowest tungsten contamination (1.99 at.%). The sample treated for 30 min has an intermediate tungsten content (5.05 at.%) [143]. These quantitative results are consistent with the qualitative observation of EDS mapping which shows that the whole surface of the sample treated 180 min is almost covered by WC fragments, whereas the sample treated 60 min has the least coverage of WC fragments.

The quantitative surface roughness of the specimens was obtained using the 3-D non-contact profilometry, as shown in Fig. 4.5. As presented in the oblique plots of this figure, the surface of the as-received sample is smoother than those of the treated ones. The histogram plot of the former is also much narrower than that of the latter, and the average value is very close to 0. In terms of the peak-to-valley (PV), the root-mean-square average (rms), or the arithmetic-mean (Ra) values, the values of the treated samples are higher than those of the as-received sample. However, there is only slight difference among the treated samples. The sample treated 180 min shows somewhat lower surface roughness than the one treated 30 min. This difference comes from the fact that a long time of repeated bombardments can reduce part of the peak height [87, 151]. As a result, the PV value, rms, and Ra decrease slightly and, then, stabilize after long SNH treatment ($>$ 60 min)[151]. Roughness in terms of PV, rms, and Ra are summarized in Table 4.1

Table 4.1 clearly shows that the roughness measured by all the three methods are consistent with each other. By the difference caught by each different method

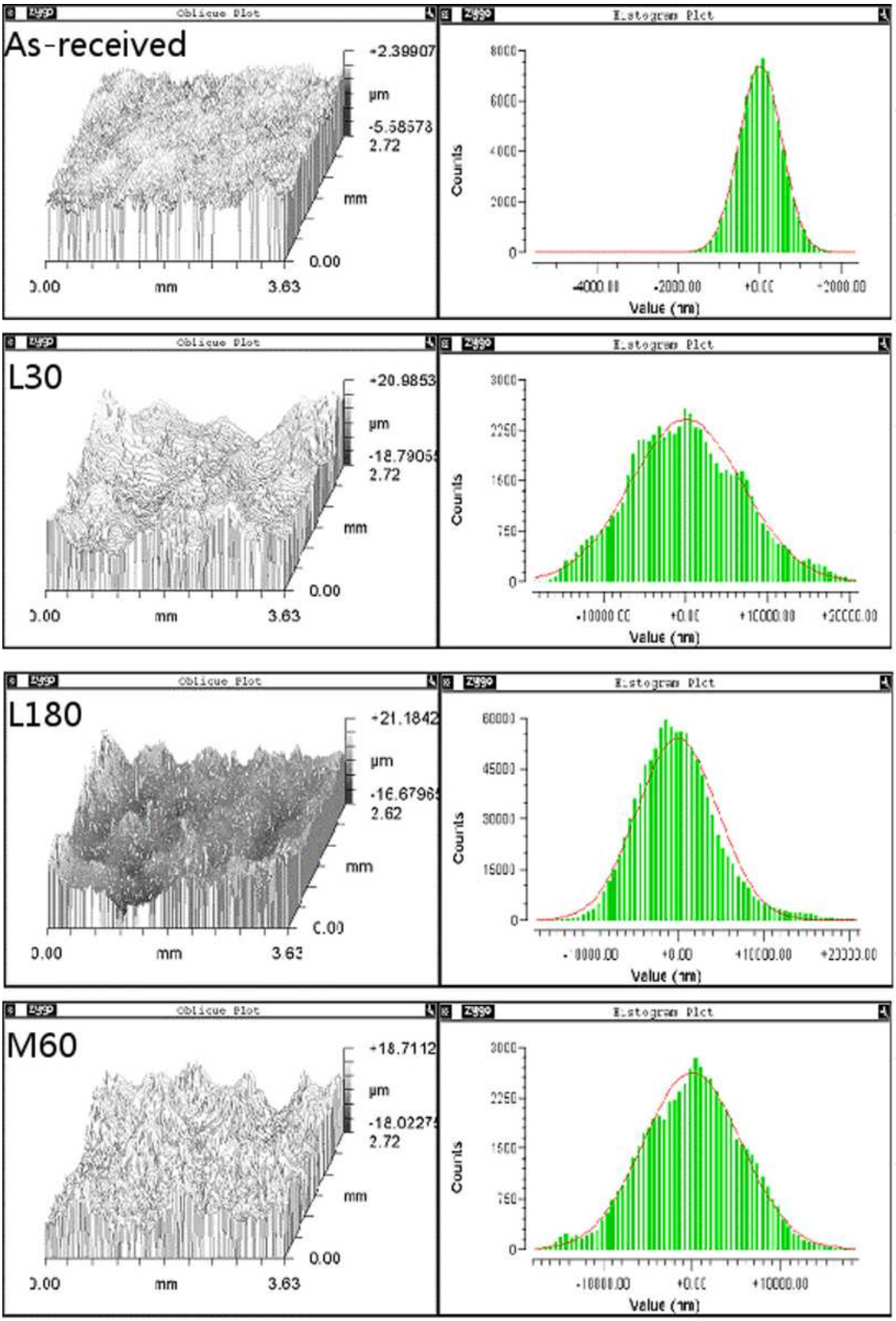

Figure 4.5: Surface roughness of as-received and processed samples measured by a 3-D non-contact profilometry in terms of PV, rms, and Ra.

mentioned above, we can know that (1) after processing, the surface is relatively uniform, since rms is sensitive to extremely high or low values, and here it does not show any abnormal values; (2) the overall surface does not present an obvious curvature, this conclusion is made due to the results that the curvature-sensitive methods, Ra (or rms), and the curvature-insensitive method, PV, do not show any inconsistency. The reason that no curvature difference is detected is because that the measurement is confined within a small area (about 0.6 mm $\times$ 0.9 mm).

4.3.2 Microstructures

Shown in Fig. 4.6 are the full width at half maximum (FWHM) of the X-ray peaks of Ni (111), (200), (220) and (311) crystallographic planes for the four different samples investigated in this study. Note that the XRD signals are measured from the surface of the samples. Based on the absorption coefficient of Ni [43], it is estimated that 90% of the XRD signals are from the top 10-μm surface layer, which varies slightly with the reflection angle.

Using Eq. 4.1 with the FWHM of the Ni (111) reflection, the average crystallite sizes at the surface layers of the Ni samples with different SNH treatment conditions have been estimated and listed in Table 4.2. It can be seen from Table 4.2 that the average crystallite size at the surface layer is in the nanometer regime and decreases with increasing the processing time and the size of balls.

Another interesting phenomenon observed in this study is the change of effective internal strains with S^2PD processing conditions. Using Eq. 4.3 with the FWHM of the Ni (311) reflection, the internal strains in the nickel crystallite have been calculated and included in Table 4.2. It is very interesting to note that the sample L30 has the largest internal strains, while the sample L180 possesses the smallest internal strains among the three treated samples. It is well known that the internal strains are reflections of the lattice micro-strains and mainly induced by defects, such as dislocations. Thus, the estimation of the internal strains suggests that the sample

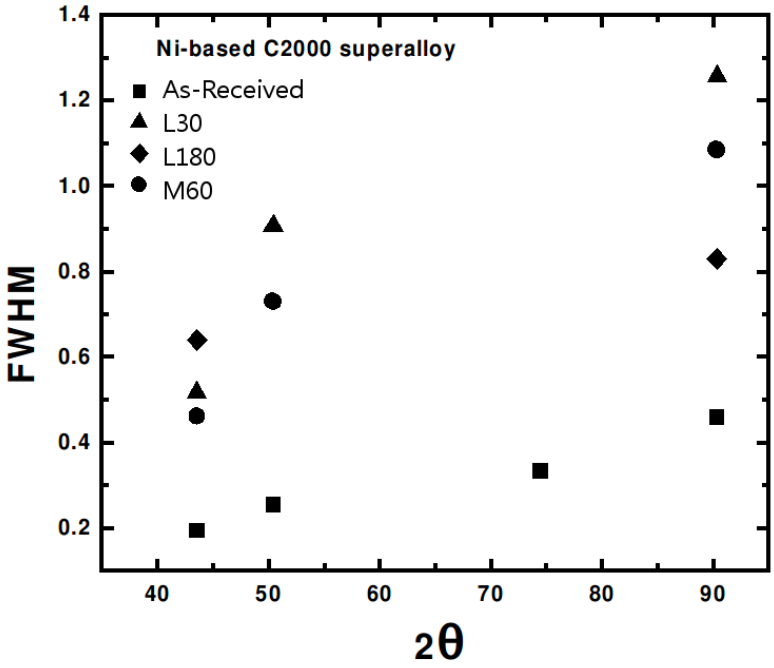

Figure 4.6: Full Width at Half Maximum (FWHM) of the diffraction peaks from the specimen surfaces.

Table 4.2: The grain sizes and internal strains estimated by XRD

Sample ID	Grain Size (μm)	Internal Strain (μm)
L30	17.8	1.0%
L180	14.7	0.6%
M60	20.4	0.8%

treated 180 min has the lowest dislocation density. One possible explanation for this trend is that the dense dislocations generated in the early stage of the SNH treatment rearrange themselves and evolve into grain boundaries, leading to the formation of nano-grains containing few dislocations in the sample treated 180 min. Therefore, the lattice micro-strains in the samples treated 30 and 60 min are larger than that in the sample treated 180 min. Although this explanation appears to be very reasonable, it remains to be confirmed by the detailed TEM investigation.

The formation of nano-grains is confirmed with the TEM analysis. As shown in the TEM bright-field image in Fig. 4.7, 10 to 30 nm grains are present in the surface layer of the sample L180. The previous TEM study has shown that the grain

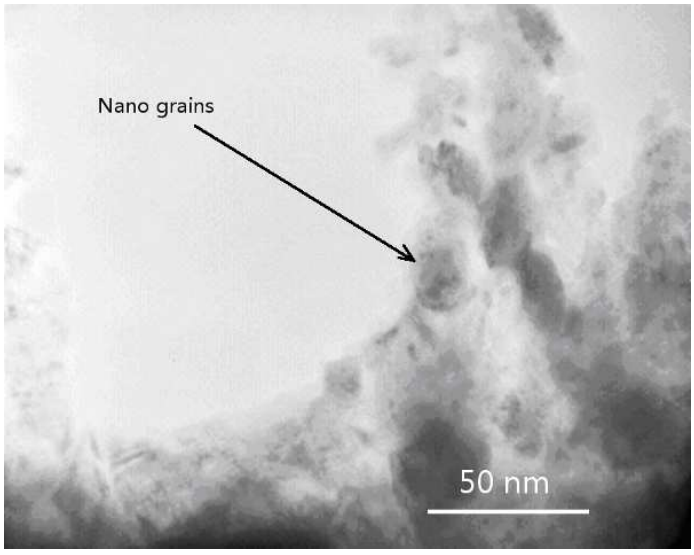

Figure 4.7: Nano-grains in the surface of the sample treated 180 min with 7.9-mm balls shown by the TEM bright-field image.

size in the surface layer of the sample L30 is in the range of 20 nm. Therefore, the estimation of grain sizes in the surface layer based on XRD is corroborated by the TEM analysis.

The general view of the cross-sectional microstructure of the as-received and treated samples is presented in Fig. 4.8. The grain size of the as-received sample is relatively uniform, about 80 to 100 μm in diameter with some visible annealing twins. The surface layer of the sample L30 [Fig. 4.8(b)] clearly shows deformed grains. The thickness of the surface layer with deformed grains becomes thicker as the treatment time increases to 180 min [Fig. 4.8(c)]. Moreover, the grain boundaries at the very surface layer have become hardly discernable. In contrast, the sample M60 has less deformation evidence [Fig. 4.8(d)]. Thus, based on Fig. 4.8, and the assumption that the thickness of the surface nanocrystalline layer is proportional to the depth of the deformation zone, it can be concluded that the thickness of the nano-surface layer increases from the samples M60 to L30 and, then, to L180. A detailed TEM study [153] has indeed confirmed such a relationship between the thickness of the surface nanocrystalline layer and the depth of the deformation zone, and revealed that the sample treated 180 min has a surface nanocrystalline layer of 50 μm in thickness,

whereas the surface nanocrystalline layer for the sample treated 30 min is thinner than 5 μm.

Based on these results, a comparison between Fig. 4.8 and Table 4.2 indicates that the sample treated 60 min has the thinnest nano-surface layer and largest grain size, whereas the sample treated 180 min has the thickest nano-surface layer and smallest grain size. Such a phenomenon is consistent with the decrease in the kinetic energy of WC balls and, thus, the degree of plastic deformation in the C-2000 alloy when the ball size changes from 7.9 (for the 30 and 180 min samples) to 4.9 mm (for the 60-min sample).

4.3.3 Microhardness profiles and macroscopic residual stresses

Figure 4.9 shows that the surface hardness of all the samples increases after the SNH process, regardless of the process times or ball sizes. It is interesting to find that the samples treated 180 and 30 min exhibit similar micro- hardness profiles. This trend may indicate that strengthening has reached the saturation point after 30 min of processing, even though the microstructure has continued to evolve, and the thickness of the nano-grain layer continues to extend. Another possible reason is that the total contribution of the refined grains and work hardening to the hardness improvement in these two samples is similar to each other. For the sample M60, it has a lower hardness than the others, since small balls have a lower kinetic energy and, thus, induce less plastic deformation as well as a shallower deformation zone in the workpiece than the large balls do. Indeed, as shown in Fig. 4.9, the thickness of the work-hardened layer for the sample M60 is about 220 μm, whereas the work-hardened layer for samples L30 and L180 is thicker than 350 μm. The previous study [88] shows that the 30-min treatment with 7.9-mm balls results in a work-hardened layer of about 800 μm.

Macroscopic-residual stresses are usually considered as one of the most important factors affecting the fatigue strengths of engineering components. Many studies

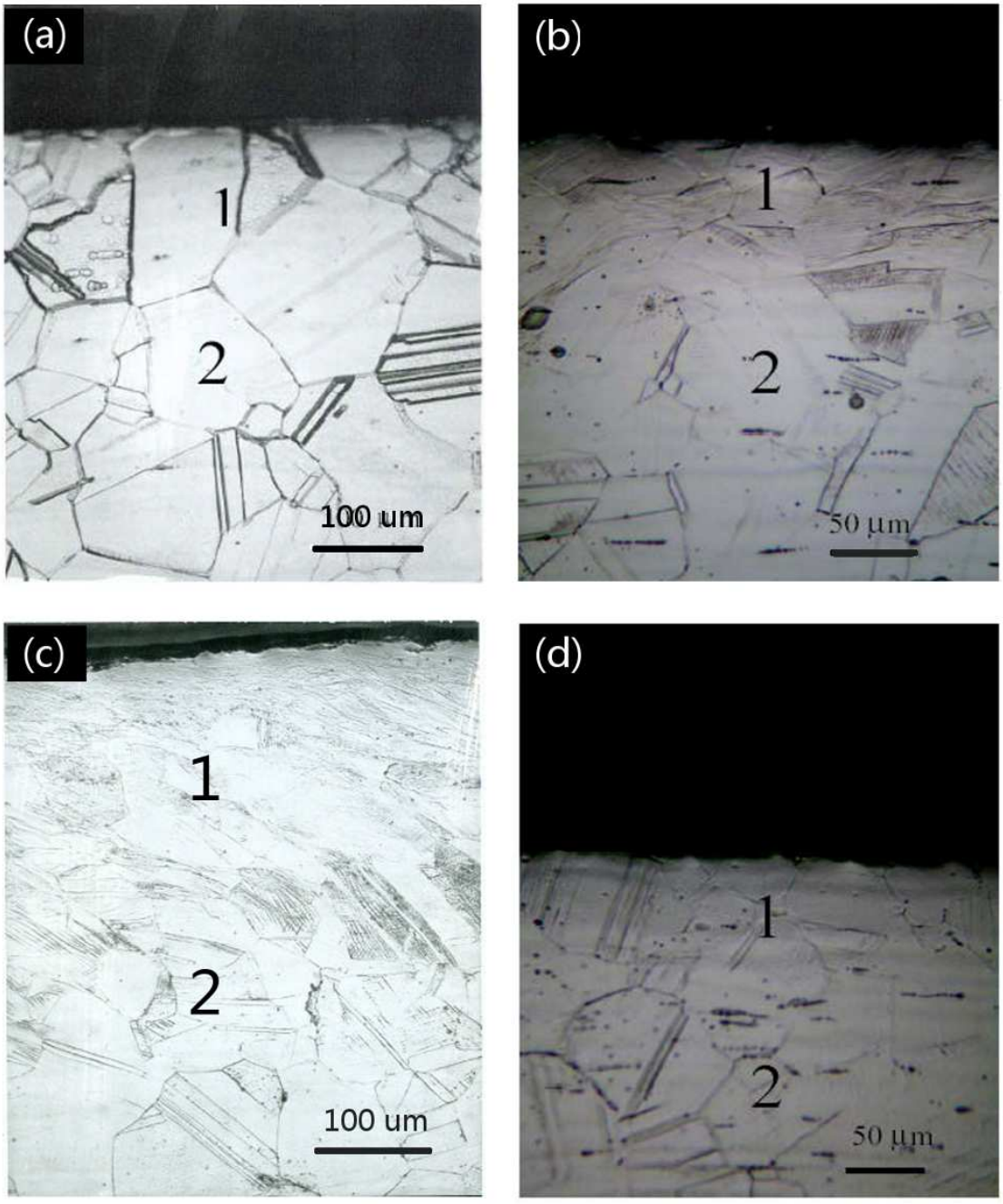

Figure 4.8: Optical images of the cross-sectional microstructures of Ni-based C-2000 samples: (a) as-received, (b) L30, (c) L180, and (d) M60. 1 is the near-surface zone, and 2 is the interior.

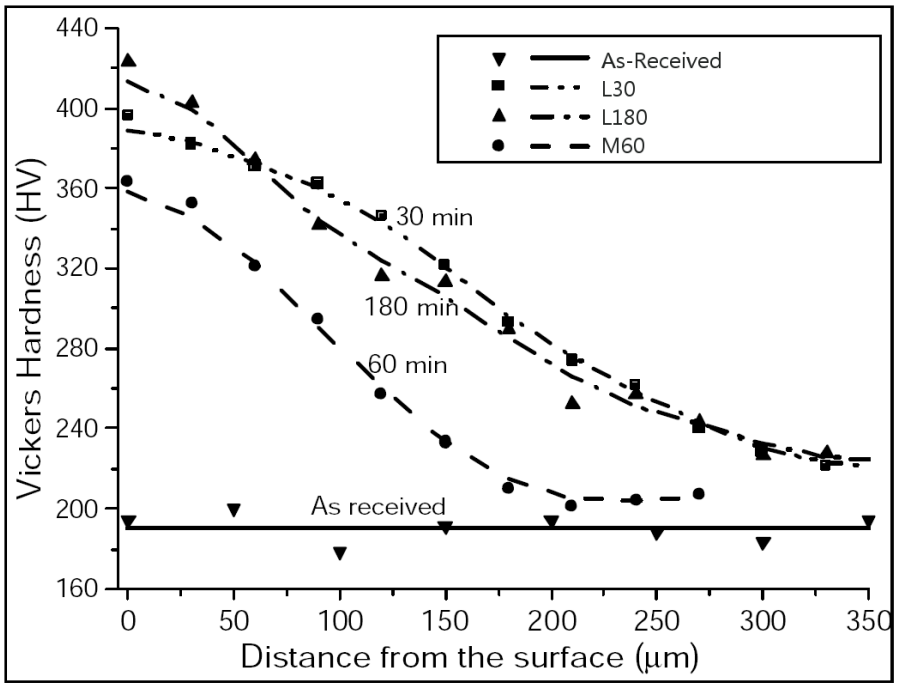

Figure 4.9: Microhardness profiles along the cross sections of the as-received and the processed samples.

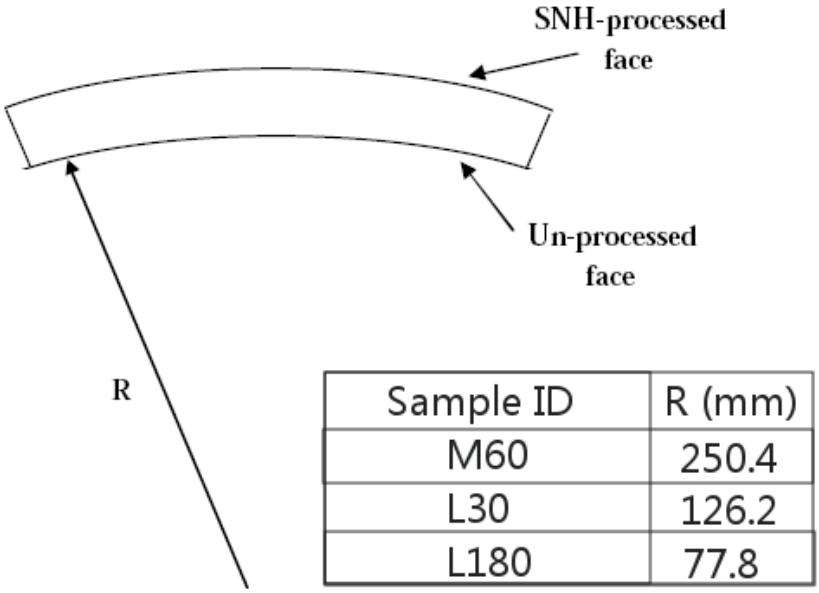

Sample ID	R (mm)
M60	250.4
L30	126.2
L180	77.8

Figure 4.10: The bending direction of the C-2000 plates after S^2PD processing on one side of the plate and their radii of curvature, R, as a function of the S^2PD-processing condition.

have shown that residual compressive stresses at the surface region can effectively inhibit the initiation and propagation of fatigue cracks, and, thus, improve the fatigue resistance. In this study, the sign of residual in-plane stresses parallel to the plane of the C-2000 plate was qualitatively determined via the bending direction of the plate after the SNH process. Shown in Fig. 4.10 are the bending direction of the C-2000 plates after the S^2PD process and their radii of curvatures, R, as a function of the S^2PD-processing condition. Based on the bending direction and the R values measured, it can be concluded that the sample treated 180 min has the highest residual compressive in-plane stresses, which is followed by the sample treated 30 min and then the sample treated 60 min.

4.3.4 Fatigue behavior and fractography

The applied stress versus fatigue-cycle-life (S-N) curves are presented in Fig. 4.11. The results showed that the fatigue properties of the 180-min sample

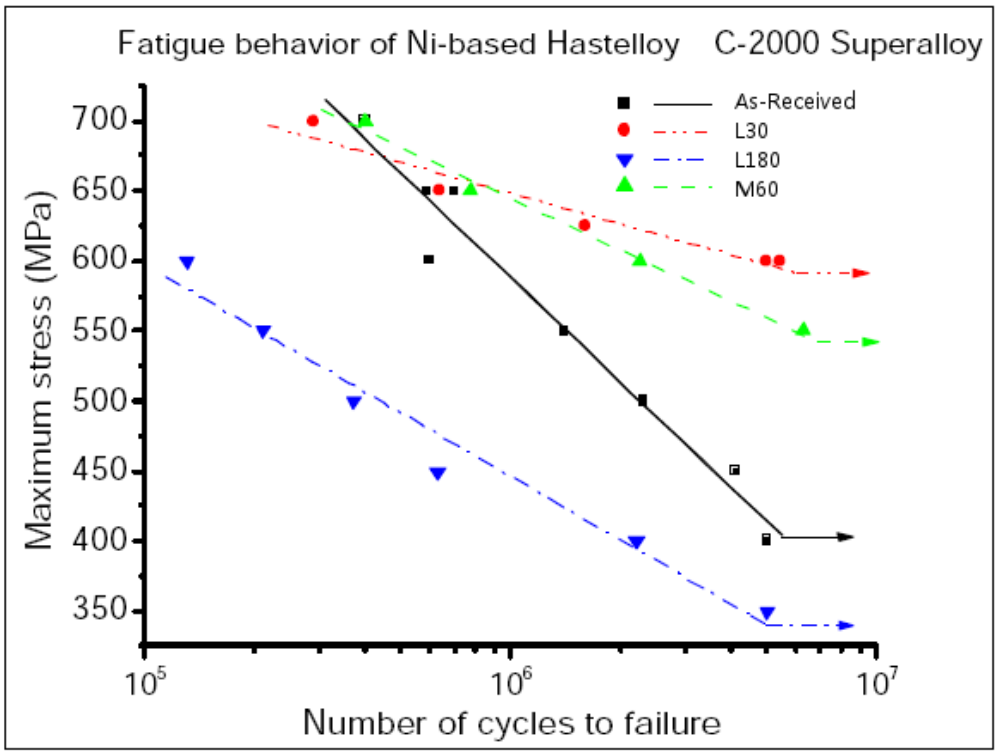

Figure 4.11: Fatigue results of the as-received and S^2PD-treated samples.

is severely deteriorated, while those of the 30- and 60-min treated samples are evidently improved when compared to the as-received one. Recall that the fatigue test was terminated for all of the samples that survived 5×10^6 cycles, and the corresponding maximum stress was taken as the fatigue strength in this study. Based on the fatigue strengths so determined, it can also be stated that L30 has the highest fatigue strength, which is 600 MPa, while the fatigue strength for L180 is only 350 MPa. The sample M60, which was processed with 4.9 mm balls for 60 min, has an intermediate fatigue strength (550 MPa) among the three samples treated. In addition, it is noted that at higher stress level of about 660 to 700 MPa, all the samples exhibit similar fatigue behaviors except for L180.

The fatigue-fracture surfaces and EDS spectra of the defects near the fatigue-crack-initiation sites are presented in Fig. 4.12. From Fig. 4.12(a), it can be seen that the fatigue-crack-initiation site of the as-received sample is right below the surface,

and there are no discernable defects near the crack-initiation site. From the fatigue-fracture surface of the sample treated 30 min shown in Fig. 4.12(b), it can be noted that the fatigue crack initiates from a defect, which shows a different microstructure, relative to the surrounding materials. The EDS spectrum of the defect indicates that it has a high content (5.26 at.%) of tungsten, which is similar to the surface tungsten content (5.05 at.%) of this sample. Fig. 4.12(c) exhibits the fatigue-fracture surface of the sample treated 180 min. It can also be found that the fatigue crack of this sample initiates from an adhesion-fracture defect (i.e., WC fragments). By EDS, this defect shows a tungsten content as high as 32.14 at.%, which is much higher than the average value of the whole surface. Thus, the crack can initiate from the WC fragment, as shown in Fig. 4.12(c). This trend significantly degrades the fatigue strength in the sample L180 (Fig. 4.11), because a large amount of WC fragments were found to be present in these samples.

4.4 Discussion

The present set of experiments clearly shows that the S^2PD process has induced many changes to the C-2000 plates. These changes include (a) the formation of a nanocrystalline surface layer (Fig. 4.7 and Table 4.2), (b) the surface work hardening (Fig. 4.9), (c) the presence of residual compressive in-plane stresses at the surface layer (Fig. 4.10), (d) the increased surface roughness (Fig. 4.5), and (e) the surface contamination due to the material transfer between balls and the plate (Fig. 4.3). Changes (a) to (c) are beneficial for fatigue properties, whereas changes (d) and (e) are detrimental.

A comparison among the characteristics shown in Figs. 4.12(a) to (d) reveals the following phenomena. First, both samples have a similar work hardening profile, as shown in Fig. 4.9. Second, the sample treated 180 min has a slightly lower surface roughness, which is expected to benefit the fatigue resistance because of the potential notch effect of surface roughness for fatigue crack initiation. Third, the sample treated 180 min has a thicker nano-grained surface layer (Fig. 4.8) and finer grain sizes (Table 4.2), both of which are expected to enhance the fatigue resistance because

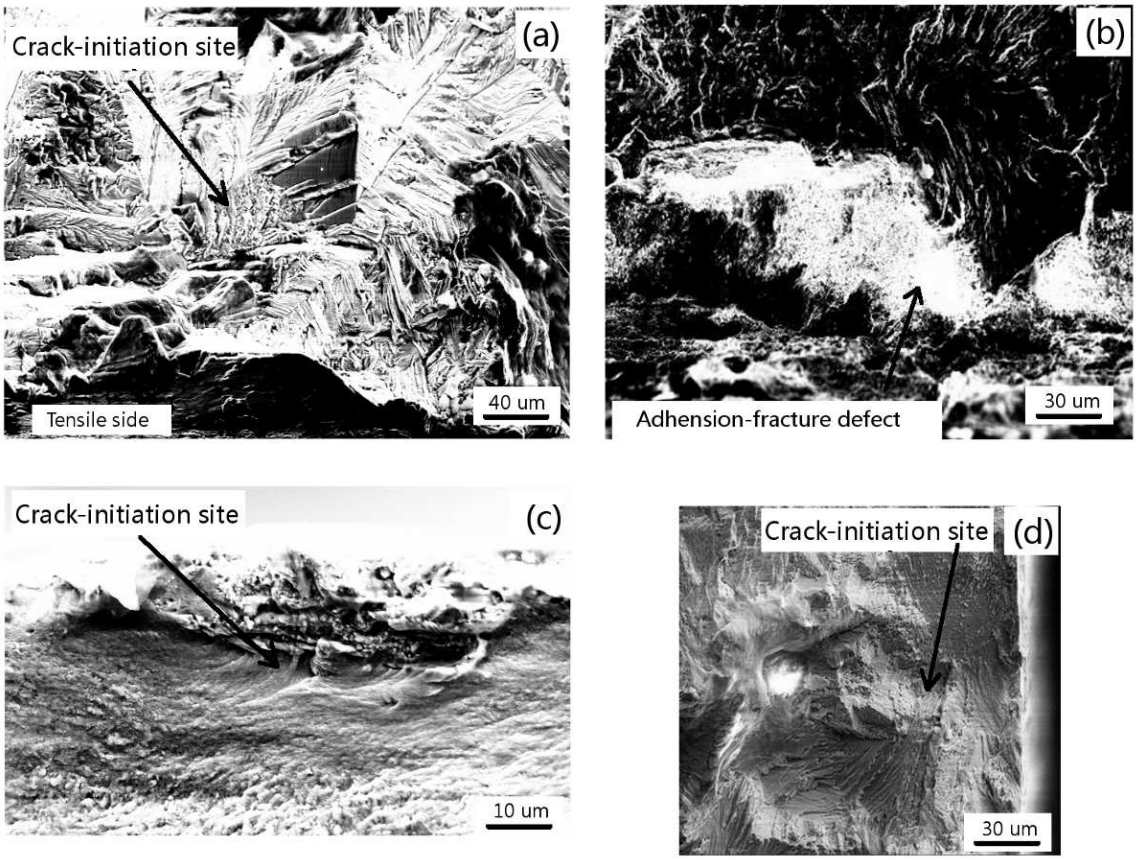

Figure 4.12: Fractography of the fatigue failure samples of As-received (a), L30 (b), L180 (c) and M60 (d). It is shown that crack initiated from the subsurface of the samples where contamination concentration is high, i.e, WC contamination is easy to become the initiation site, an EDS analysis indeed shows that those initiation sites have high W content.

of the increased strength. Fourth, the sample treated 180 min has a higher residual compressive stress (Fig. 4.10), which will also improve the fatigue resistance. Thus, based on the consideration of Changes (a) to (d) only, the sample treated 180 min should exhibit a better fatigue strength. However, the reality is that the sample L180 has a lower fatigue strength than the sample L30. The reason for this is that the L180 has a worse surface contamination than L30. The surface contamination by heterogeneous WC fragments has behaved as the crack-initiation site, as shown in Fig. 4.12. Thus, the severe surface contamination in the sample L180 has outweighed all of the benefits derived from the formation of nano-grains, work hardening, and residual compressive stresses. As a result, L180 has a lower fatigue resistance than L30. In fact, the fatigue resistance of the sample L180 is even lower than the as-received sample, indicating the potent effect of surface defects and the possible deterioration induced by improper S^2PD processing.

When the negative impact of surface contamination is avoided or minimized, significant improvements in the fatigue resistance can be achieved via the S^2PD treatment. This conclusion can be drawn from the comparison between the as-received sample and L30 and M60. Both processed samples exhibit better fatigue resistances than the as-received sample with about 50% and 37% improvements, respectively. The improvements are clearly due to a combined effect of the formation of a surface nanocrystalline layer, a work-hardened surface region, and the presence of residual compressive stresses. There is no doubt that these three beneficial changes induced by the S^2PD process have outweighed the negative impacts of surface roughness and surface contamination for the samples, L30 and M60.

Comparisons between L30 and M60 can offer additional insights into the effects of Changes (a) to (e). Recall that L30 was processed with 7.9-mm balls, whereas M60 processed with 4.9-mm balls. Different processing conditions have resulted in different outcomes in Changes (a) to (e). Specifically, L30 has a thicker work-hardened layer (Fig. 4.9), higher hardness at the surface region (Fig. 4.9), finer grain sizes (Table 4.2), a thicker surface nanocrystalline layer (Fig. 4.8), higher residual-compressive stresses (Fig. 4.10), a rougher surface (Fig. 4.5), and more surface contaminations

(Fig. 4.3) than sample M60. It is interesting to note that the beneficial effects from the formation of surface nano-grains, a work-hardened surface region, and the presence of residual compressive stresses dominate the fatigue behavior of both samples treated 30 and 60 min. As a result, L30 possesses a better fatigue resistance than M60, even though L30 has a rougher surface and more surface contaminations.

It is noted that the as-received sample and the samples L30 and M60 exhibit similar fatigue resistances in the low-cycle fatigue regime. This is most likely related to the macroscopic plastic deformation of the samples. The yield strength at 0.2% offset of the C-2000 alloy at the as-received condition is 400 MPa. After S^2PD processing, the yield strength at the the 0.2% offset at the surface region would be about 600 MPa, if the yield-strength improvement is proportional to the microhardness improvement (which shows 50% enhancements). Thus, at the low-cycle fatigue regime where the maximum stress applied is at or higher than 650 MPa, the macroscopic plastic deformation of the entire sample is likely to occur during fatigue cycles, regardless of the sample condition with or without S^2PD processing. Based on this trend, it is proposed that the similar fatigue resistances in the low-cycle fatigue regime are likely related to the low ductility of the surface nanocrystalline layer and fading of the residual-compressive stresses, both of which can promote the formation of fatigue cracks at the surface of smooth specimens. the yield-strength improvement caused by the treatment process will be discussed later.

The present set of experiments unequivocally indicates that the fatigue resistance of the Ni-based C-2000 alloy can be substantially improved by the S^2PD process. Furthermore, to fully utilize the S^2PD process, the processing condition should be designed to enhance the formation of a surface nanocrystalline layer, a surface work-hardened region, and the presence of residual-compressive stresses at the surface layer, and to minimize surface roughness and surface contamination at the same time. The process optimization to fully utilize the S^2PD process is clearly an area of future studies. Finally, it should be pointed out that the quantitative contribution of each of Changes (a) to (e) to the fatigue resistance should also be investigated in the future. It is expected that in order to accomplish this goal, a large

number of experiments need to be designed so as to separate the individual effect of Changes (a) to (e).

4.5 Conclusions

Based on the results and discussions above, the following conclusions are reached:

1. The S^2PD processing of the Ni-based HASTELLOY C-2000 superalloy has led to the following five changes simultaneously: (a) the formation of a surface nanocrystalline layer; (b) the surface work hardening; (c) the presence of residual compressive in-plane stresses at the surface layer; (d) the increased surface roughness; and (e) the surface contamination due to the material transfer between balls and the plate.

2. Larger balls in the S^2PD process have higher efficiency in introducing a surface work-hardened region, a surface nanocrystalline layer, and residual compressive stresses at the surface than small balls. However, large balls also introduce a greater amount of surface contaminations and result in rougher surfaces.

3. A longer S^2PD-processing time can lead to finer grain sizes at the surface, a thicker work-hardened layer, and larger residual-compressive stresses. However, the strengthening saturation is observed when the processing time is longer than a critical value (which is 30 min for 7.9-mm balls). A longer processing time also results in more surface contaminations, which are detrimental to the fatigue resistance.

4. The fatigue resistance of the Ni-based C-2000 alloy can be substantially improved when the alloy is processed for 30 min with 7.9-mm balls or 60 min with 4.9-mm balls. Under these processing conditions, the formation of a surface nanocrystalline layer, a surface work-hardened region, and the presence of residual-compressive stresses at the surface layer can be enhanced, while the detrimental effects of the increased surface roughness and surface contamination can be minimized.

5. When a surface contamination is not minimized, such as in the case of 180 min processing with 7.9-mm balls, the fatigue resistance can be decreased rather than increased. This is because the severe-surface contamination can outweigh all of the benefits derived from the formation of nanograins, work hardening, and residual-compressive stresses.

CHAPTER 5

Effects of Nanostructured Surface Layers on Fatigue Behavior of a C-2000 Superalloy

5.1 Introduction

Materials with a nanostructured surface and coarse-grained interior have drawn increasing attentions because of their highly-improved mechanical properties, such as the yield strength, hardness, increased wear resistance, etc. [61, 62, 145]. The terminology of the surface nanocrystallization is usually used to refer to the processes by which nanostructured surface layers could be introduced into the materials without changing their compositions. Presently, most of these processes, such as the surface-mechanical attrition [85, 147], wire-brushing [154], and surface nanocrystallization and hardening (SNH) [87, 149], are based on the severe plastic-deformation (SPD) methods, that is, utilizing mechanical impacts to introduce a large amount of dislocations or deformation twins in a short time (high strain and/or strain rate) so as to obtain refined grains. Because of the plastic-deformation process, a surface-nanocrystallized structure is usually accompanied by significant compressive stresses.

It is well known that fatigue properties of materials are highly sensitive to both the grain sizes and residual stresses. A small grain size could effectively increase the yield strength so as to enhance the fatigue-crack-initiation threshold [77]. Meanwhile, a small grain size also has an adverse effect on the resistance to the fatigue-crack growth, since cracks can easily propagate along grain boundaries. On the contrary, coarse grains may deflect the propagation paths of fatigue cracks by grain boundaries, thus introducing crack closure and decreasing the rate of crack growth. However, coarse grains are not effective in preventing the initiation of the

fatigue crack [77]. Since most fatigue cracks initiate from the surface and propagate to the interior, a component with a nanostructured surface layer and coarse-grained interior could be expected to have highly improved fatigue properties because both fatigue-crack initiation and propagation are inhibited by fine grains near the surface and coarse grains in the interior, respectively.

Moreover, the residual-compressive stresses introduced during the severe plastic-deformation process can also effectively stop the initiation and propagation of fatigue cracks. This trend is true especially when the applied stresses are relatively low, that is, in the fatigue-life range with a longer life ($> 10^6$ cycles), since under this condition, the external stresses may be overweighed by the residual-compressive stresses. Structures with surface compressive stresses have been shown to have superior fatigue properties in some materials [12]. In the fatigue-life range with a shorter life ($< 10^6$ cycles), since the applied stresses exceed the residual-compressive stresses, the latter, thus, become a less critical factor, which gives way to some other features of the material, such as the stress concentration and surface roughness.

The nickel-based HASTELLOY C-2000 superalloy* is a typical room-temperature corrosion-resistance superalloy with a single-phased fcc structure. This material is selected due to the reasons that it may facilitate the analysis of the formation mechanism of nanostructures during the severe-plastic-deformation process, as well as the investigation of the effects of the process parameters and the nano-layer on the fatigue properties of the alloy. It has been demonstrated in a previous study [88] that the C-2000 specimens treated with the SNH process for 30 min has indeed exhibited a 50% enhancement in the fatigue resistance, when compared with the counterpart without the treatment. The enhancement has been attributed to the formation of nano-grains at the surface, a surface work-hardened layer, and the presence of residual-compressive stresses in the surface region [88]. It should be noted that the main difference between the current SNH process and a traditional shot peening process includes the thickness of the work-hardening-affected zone and the nano-layer, as well as the compressive stresses, which are investigated in another related study [155].

*HASTELLOY and C-2000 are registered trademarks of Haynes International, Inc.

A recent work has further revealed that not all of the C-2000 alloys after SNH processing exhibit the improved fatigue resistance. Instead, improper SNH processing can result in the degradation of the fatigue resistance. In the present study, additional SNH-processing conditions were investigated in order to identify the domain(s) of the proper SNH processing window for improving the fatigue resistance of the C-2000 superalloy and to further understand the factors that lead to the degradation of the fatigue resistance.

5.2 Experimental Procedures

The material used in this work was a Ni-based HASTELLOY C-2000 superalloy (cold-rolled and fully annealed at 1,120 $^{\circ}C$) with a nominal chemical composition (in wt.%) of 23Cr, 16Mo, 1.6Cu, 0.01C, 0.08Si, and balance Ni. The diameter of the as-received specimen is 50 mm,and the thickness is 3.22 mm. Five tungsten carbide and cobalt (94%WC+ 6%Co, in wt.%) balls with a diameter of 7.9 mm were used to treat the as-received sample, and the duration times are 30, 60, 90, and 180 min, respectively. After the SNH treatment (both sides of the samples are processed with the equal time), which was described in detail in Chapter 2, the samples were, then, cut to small bars with a dimension of $3.2 \times 3.2 \times 25$ mm^3 and subjected to the load-controlled four-point-bend fatigue tests on an MTS 810 electrohydraulic test machine. The distance between the two inner and two outer pins were 10 and 20 mm, respectively. The stress ratio, R [the ratio of σ_{min} (the minimum stress) to σ_{max} (the maximum stress) in one cycle of loading], was 0.1, and the applied frequency was 10 Hz.

The microstructures of the as-treated surface and fatigue-fracture cross sections were characterized by the scanning-electron microscopy (SEM), X-ray diffraction (XRD), and transmission-electron microscopy (TEM). TEM samples at certain depths away from the specimen surface were obtained by: (1) first mechanically polishing on two sides until the sample reached a 20-m thickness, and (2) finally thinning by a two-side jet with a solution of the 5% perchloric acid and 95% ethanol (in vol.%) at 10 $^{\circ}C$. Hardness tests were conducted on a Buehler Vicker's hardness tester, and

the applied load was 300 gf (2.94N). The interference between indentations was eliminated in the measurement. This trend was done by keeping the distance between two successive indentations at about 10 times the size of the impressions. We did this by moving both the x- and y-positions of the indenter, that is, from the surface to interior, the alignment of the indentations is an oblique rather than a perpendicular line to the surface. X-ray diffraction experiments were implemented on a Philips X'pert Diffractometer, and Cu K_α ($\lambda_{K_{\alpha 1}} = 0.154056$ nm and $\lambda_{K_{\alpha 2}} = 0.154439$ nm) radiation was used. The as-treated samples were cut to a 12 $\times$ 12 mm^2 square shape, and the surfaces were scanned with a continuous-scanning mode at a rate of 1.5°/min.

5.3 Results and Discussion

The cross-sectional microstructure of the as-received and the 180-min SNH-treated sample is shown in Fig. 5.1. It can be seen from Fig. 5.1(b) that the near-surface structure has been modified greatly after the treatment. The near-surface grain boundaries and twin boundaries, which are easy to observe in the as-received sample [Fig. 5.1(a)], are difficult to distinguish by the optical microscope on the surface of the 180-min SNH-treated sample. From the surface to interior, the grain-size distribution exhibits a gradient change as expected. Within the grains somewhat far away from the surface, it can be seen that a large amount of cross-linked lines are presented, which are unquestionably caused by the plastic-deformation. These cross-linked lines are confined within individual grains, and have been identified as deformation twins rather than deformation bands or shear bands in previous studies [88].

Figure 5.2 shows a TEM bright-field image and the corresponding selected-area-diffraction (SAD) pattern obtained from the position 50 μm away from the surface of the C-2000 sample SNH-treated for 180 min. It is noticed that the grain size is in the range of 30 to 70 nm. Furthermore, the SAD pattern is composed of partially continuous diffraction rings, which confirms that the as-received large crystalline grains (in the order of 50 μm) have been broken down to nano-grains in this region, and many of these nanograins have high-angle grain boundaries among

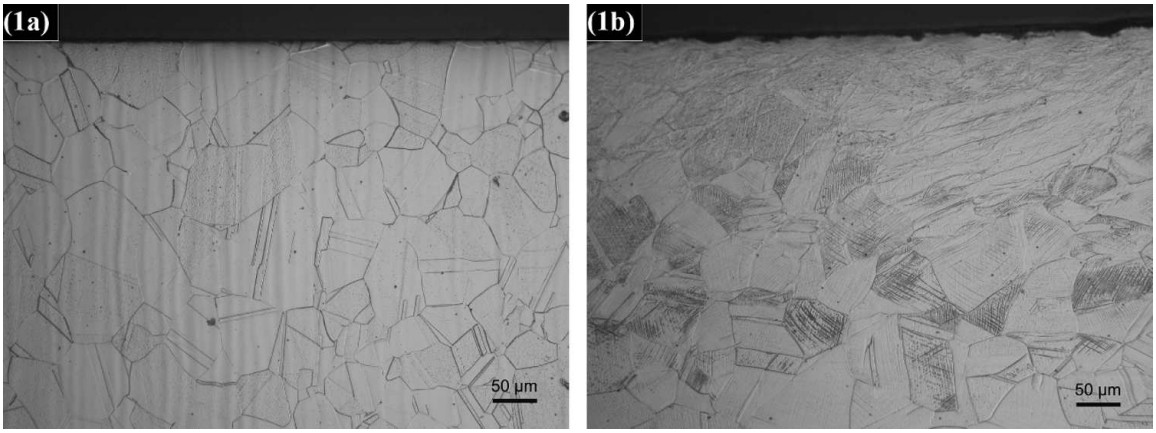

Figure 5.1: Optical microscopic images of the: (a) as-received and (b) 180-min SNH treated samples.

themselves. Figure 5.2(b) shows a TEM bright-field image, and the corresponding selected-area diffraction pattern obtained at the impacted surface from the same sample as in Fig. 5.2(a). The diffraction pattern of continuous rings at this location clearly indicates that the nano-grains at the impacted surface have completely random orientations with high-angle grain boundaries. Furthermore, the grain size has reduced to 10 to 30 nm. Therefore, based on Figs. 5.1 and 5.2, it can be known that after the SNH process, a nanostructured surface layer was formed in the 180-min SNH-treated sample. This nanostructured layer has a grain-size gradient changing from 10 to 70 nm as the locations moves from the impacted surface to a depth of 50 μm.

Figure 5.3 exhibits the microhardness distribution along the depth of the samples. Because of the SNH process, work hardening occurs in these samples. The hardness of the near-surface layer of the as-received and the treated samples are about 250 and 470 Hv, respectively. Compared with the as-received sample, the hardness of the treated sample has been increased substantially, but the hardness profile does not change much with the processing time. Since work hardening is a consequence of the severe plastic-deformation process, it can be seen that after the surface treatment for 30 min, the depth of the deformation-affected zone changed only slightly. In other words, because the intensity of the impact of the balls does not change, the plastic-deformation zone remains nearly constant, although it has already been known that the surface nano-layer could continue to extend with the processing time.

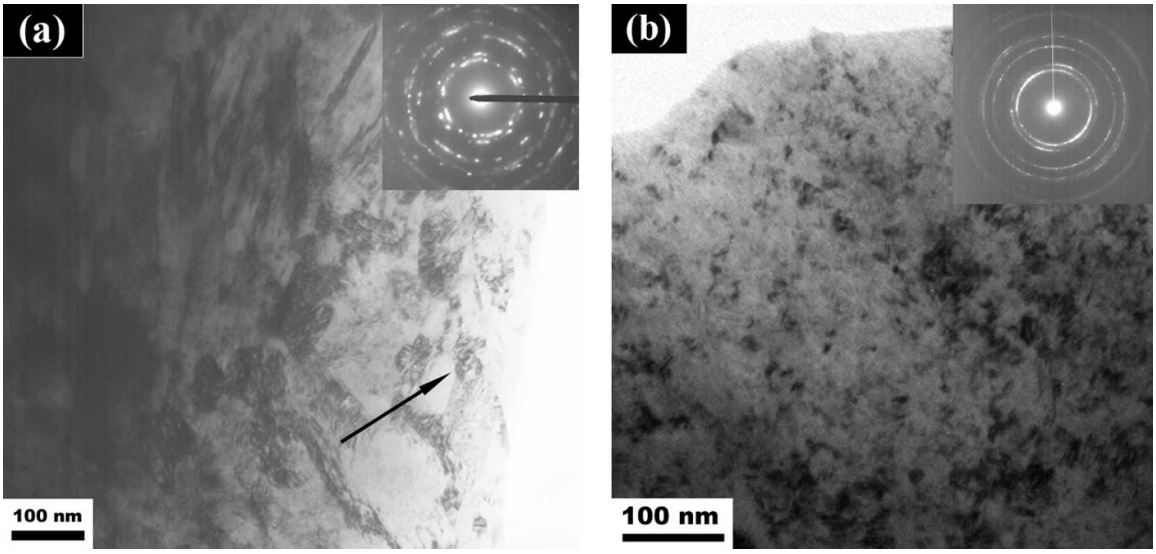

Figure 5.2: TEM bright-filed image and SAD patterns of the 180 min SNH-treated sample with: (a) at 50 μm away from the surface, showing the formation of 30 - 70 nm nanograins, one of which is pointed out using the arrow, and (b) at the impacted surface, showing the formation of 10 - 30 nm nanograins.

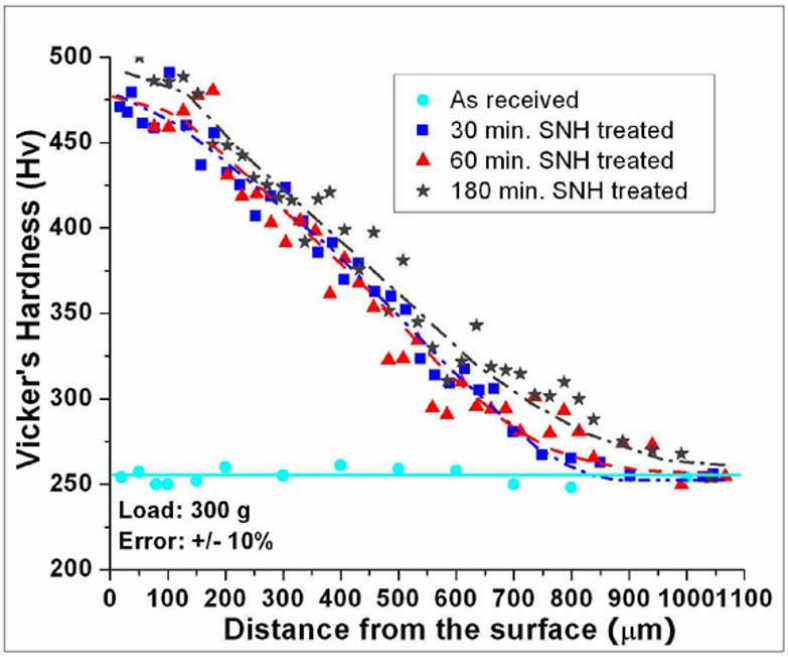

Figure 5.3: Vicker's Hardness profile of the specimens.

Four-point-bend fatigue tests were conducted on the as-received and SNH-treated samples, and the resulted stress versus the number of cycles to failure (SN) curves are shown in Fig. 5.4. The oblique lines are drawn according to the linear regression principle while the horizontal lines with arrows indicate that at these points (usually the cycle number is 5×10^6, a larger limit, say, 10^7 cycles may be very time-consuming for a 10 Hz fatigue test), the sample actually not failed and it is considered under this circumstance the sample will not fail and the corresponding stress is considered as the fatigue strength. One obvious result is that the SNH process indeed affects the fatigue behaviors of this alloy. For the 30-min treated sample, the high-cycle fatigue-endurance limit has improved from 400 to 600 MPa, but for the 60- and 90-min-treated samples, it does not change much. For the 180-min-treated sample, the fatigue strength was even lower than that of the as-received sample, decreasing from 400 to 350 MPa. However, when the applied stress exceeds 700 MPa, it appears that the fatigue lifetimes of all the treated samples are lower than that of the as-received one. The longer the processing time, the lower the fatigue lifetimes in the fatigue-life range smaller than 10^6 cycles. One of the possible reasons for this phenomenon is that when the applied stress is relatively high, most of the benefits that a nanostructured surface layer can contribute to the fatigue strength will be counteracted by the external stresses. For the SNH-treated samples, a large amount of surface contaminations and damages are introduced during the process. These flaws are potential stress-concentration sites during the fatigue test. Therefore, fatigue cracks may easily initiate and propagate from the surface at high-stress levels.

Theoretically, a component with a nanostructured surface layer could have a superior fatigue property compared with its coarse-grained counterpart, as we discussed in Chapter 1 and found in the previous study [88]. However, it is noted that this trend is not always the case; the 180-min SNH-treated sample shows a severely deteriorated fatigue behavior. Besides the contamination issue, the root of the matter may originate from the severe-plastic-deformation process itself. During any SPD-based processes, from the surface-mechanical-attrition treatment (SMAT) [78, 85, 147] to wire-brushing [154], the equal-channel-angular pressing (ECAP) [156],

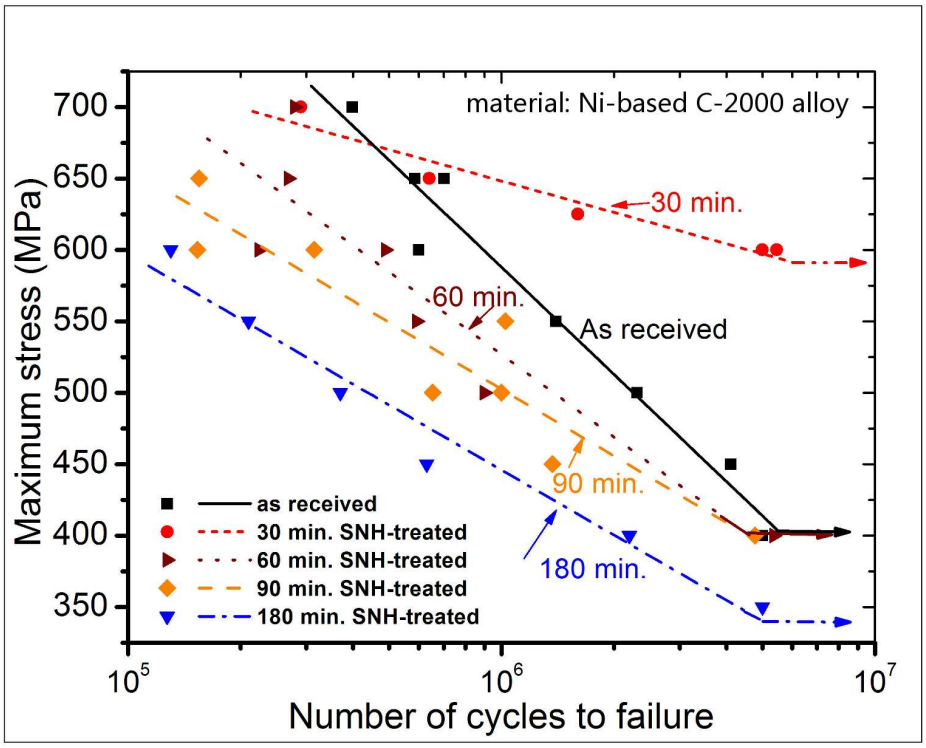

Figure 5.4: Stress - Fatigue lifetime (S-N) curves of the as-reveived and the SNH-processed samples. It is shown that longer processing time decreases the fatigue life in both the low-stress and the high-stress levels.

and SNH [87, 149], a large amount of lattice defects, i.e., high-density dislocations, are generated in the material in a very short time, and the near-surface microstructure of the material is drastically changed. The high-density dislocation clusters or tangled dislocations generated in the SPD process can accumulate further in the subsequent fatigue loading, and form micro-damages, such as voids and microcracks. Since usually no follow-up recovery processes, i.e., annealing, are applied after the SPD process, the lattice defects or sometimes micro-damages are present in the SPD-processed material. Therefore, for those properties, which are sensitive to the micro-damages, such as fatigue, the existence of these defects may severely affect the behavior of the material. For example, in an ECAP-treated AlMg specimen, it was reported that the fatigue strength has indeed remained unchanged even though the yield strength was improved greatly due to the grain refinement [156]. On the other hand, for those properties, which are not sensitive to the micro-damages, such as hardness and yield strength, they will not be affected much by these defects.

It is known that during a fatigue test, the stress-intensity-factor range ΔK ($\Delta K = K_{max} - K_{min}$, where K_{max} and K_{min} are the maximum and minimum stress-intensity factors, respectively) is a function of both the crack size, a (for an internal crack, the size is 2a, but for a surface crack, the size is a) and the applied stress range, $\Delta\sigma$ ($\Delta\sigma = \sigma_{max} - \sigma_{min}$), i.e., $\Delta K = Y\Delta\sigma(\pi a)^{1/2}$, where Y is the correction factor, usually of the order of unity. When ΔK is smaller than the threshold-stress-intensity-factor range, ΔK_{th}, the crack practically should not grow. That is, under certain external stress amplitudes, $\Delta\sigma$, the macrocrack initiation does not take place if the sizes of microcracks are sufficiently small; or, for a given microcrack size, a, the macrocrack should not propagate, if the external stress magnitude is sufficiently small. During the SNH process, as the processing time increases, both the number and size of the micro-damages and surface contaminations could increase, which may, thus, increase the probability of the macrocrack initiation. The probability, $Q(N)$, that at least one macrocrack initiates at a cycle number, N, is presented as [4]

$$Q(N) = 1 - exp\{-f[\omega(N)]\} \tag{5.1}$$

where $\omega(N)$ is the measure of the local damage of the cycle number, N, and $0 \leq \omega \leq 1$. $\omega = 0$ for a non-damaged material; $\omega = 1$ for a completely damaged material; $\mu(N) = f[\omega(N)]$ represents the mean number of macrocracks initiated at the cycle number, N; the function, $f()$, is differentiable and satisfies the conditions, $f'() > 0$, $f(0) = 0$, and $f(1) = 1$. In this case, due to the surface contamination and micro-damages caused by the impact, the equation, $\omega(N = 0) > 0$, will be satisfied, and its value increases with the processing time. Thus, from Eq. 5.1, it can be known that the increase in the number of microcracks could evidently increase the probability of the macrocrack initiation if no other effects are considered. This conclusion could be used to explain that the SNH or other SPD-based processes could cause the decrease in the fatigue strength, and a longer time treatment makes this effect more pronounced than a shorter time treatment. In short, the fatigue behavior depends on the competition between the positive factors (such as compressive residual stresses, a nanostructured surface layer, a grain-size gradient, work hardening, etc.) and the adverse factors (such as the surface contamination and micro-damages).

The cross-sectional SEM observations of the fatigue-fractured specimens were shown in Figs. 5.5 and 5.6. In Fig. 5.5, the crack-initiation sites of the as-received and the processed samples are compared. It can be seen that all the initiation sites were located beside some defects. For the as-received sample, this defect was an inclusion inside the specimen; while for the treated samples, the defects were WC contaminations at their surfaces. This observation is confirmed by the energy dispersive X-ray spectroscopy (EDX) , as shown in Fig. 5.5(d). It is found that at this initiation site, the contents of the W, C, and Co are much higher than those at other positions, which indicates the presence of an adhesion-fractured defect. That is, when the WC/Co balls bounced back from the surface, materials from the ball were left on the sample surface, and the contamination problems is, thus, generated. Figure 5.6 shows the crack-propagation area of the as-received and the 60-min processed samples. A typical intergranular propagation mode was found for the as-received sample, and the average fatigue striation width is about 2.4 μm, as shown in the figure. Some evident crystallographic facets (indicated with a arrow) with width about 15 μm can

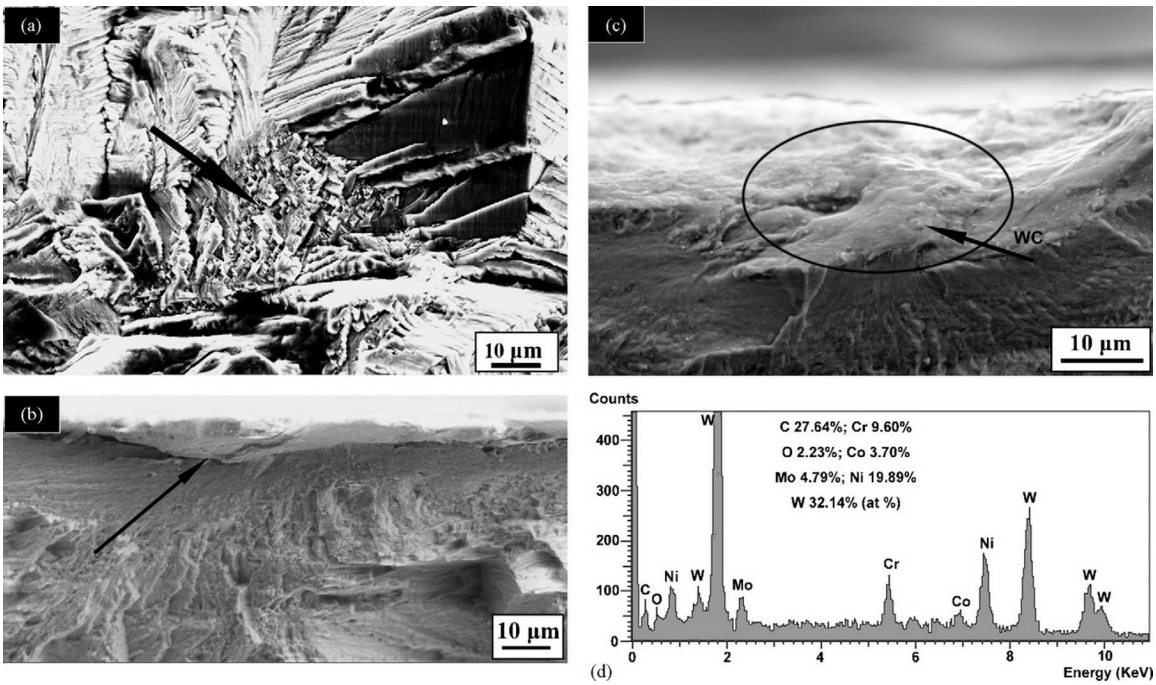

Figure 5.5: Crack-initiation-site comparisons of the: (a) as-received, 500 MPa, (b) 30-min SNH-treated, 700 MPa, (c) 60-min SNH-treated, 550 MPa samples, and (d) EDX spectrum of the selected area in (c).

be seen in Fig. 5.6, which are caused by the cyclic loading and corresponds to the loading stresses; while for the 60 min SNH-treated sample, a large amount of deformation twins are found, it is hard to detect the fatigue striations, although the distance between two adjacent crystallographic facets can be easily measured as about 10 μm or less. Because of the plastic-deformation, the propagation of the fatigue cracks have been confined within the deformation twins as it is observed that the crystallographic facets have so many different orientations.

5.4 Conclusions

Using the SNH process, a C-2000 alloy with a nanostructured surface layer was obtained, and the fatigue behaviors of the specimens were investigated. It is shown that the severe plastic-deformation-based surface-nanocrystallization process could affect the fatigue behaviors of the material in two ways. The nanostructured surface layer, work-hardened region, and residual-compressive stress could enhance the fatigue strength especially in the high-cycle fatigue range ($> 10^6$ cycles), while

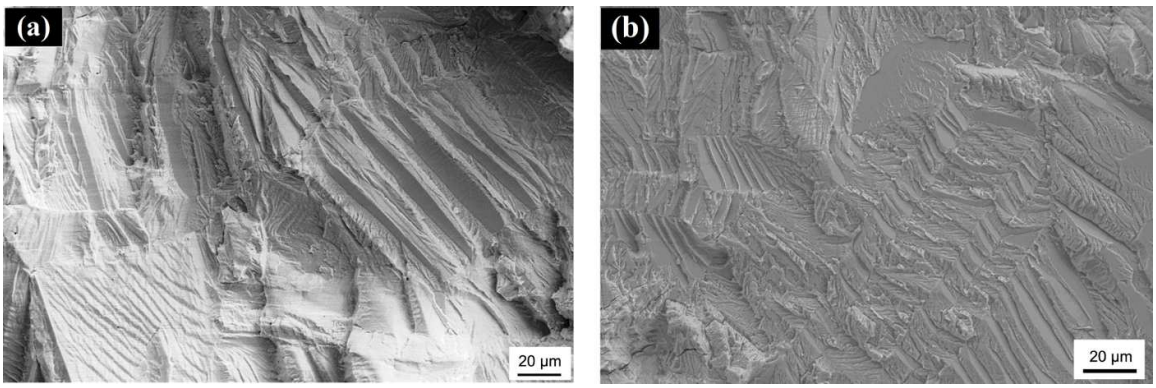

Figure 5.6: Crack-propagation comparison of the: (a) as-received, 700 MPa, and (b) the 60-min SNH-treated, 550 MPa samples.

the surface contamination and micro-damages caused by the SNH process could deteriorate the fatigue strength. Using five WC/Co balls 7.9 mm in diameter, the 30-min treatment results in the best improvement in the fatigue resistance, while prolonged treatments (60, 90, and 180 min) either lead to no improvements or even decreases in the fatigue resistance. In the shorter cycle fatigue range ($< 10^6$ cycles), the fatigue lifetimes of all the treated samples except the 30-min-treated sample are lower than those of the as-received one. The longer the processing time, the lower the fatigue lifetimes in the shorter-cycle-fatigue range. Thus, to fully utilize the SNH process to improve the fatigue behavior of the material with a nanostructured surface layer, processing conditions need to be optimized, at least in terms of processing-time periods.

CHAPTER 6

On the Ductility of a Surface-Severely-Plastically Deformed Nickel Alloy

6.1 Introduction

Surface-severe-plastic deformation (S^2PD) processes [157, 158] have been recently developed to introduce nano-grains and grain-size gradients into the surface region of bulk materials. There are several variants of S^2PD-based processes [157, 158] among which S^2PD with high-velocity ball impacts has received most of the attention because of its versatility in processing complex-shaped parts [78, 81–83, 85, 88, 90, 91, 147, 148, 150, 151, 159, 160]. S^2PD with high-velocity ball impacts is similar to conventional shot peening (SP) because both processes entail impacting the workpiece surface using balls and shots. However, the kinetic energy of balls in S^2PD is 150 to 1,000 times larger than that in SP [89]. As a result of this high kinetic energy, S^2PD can produce a thicker nanocrystalline (nc) surface layer, a deeper work-hardened region, and a thicker surface zone with residual-compressive stresses [89].

The nc surface layer combined with the work-hardened region and residual-compressive stresses has imparted the S^2PD-processed materials with superior mechanical properties. It has been demonstrated that the fatigue-endurance limit of a nickel-based alloy can be improved by 50% via S^2PD, as shown in the previous chapter. The improvement in the fatigue resistance has also been demonstrated for a 316L stainless steel [81]. Other mechanical properties, such as the tensile strength and wear resistance, have all been enhanced by S^2PD [85, 90]. However, it is also noted that the ductility of the material normally decreases after S^2PD processing. For

example, a recent study [75] reveals that the 0.2% offset yield strength of a nickel-based alloy is increased by 65 to 85%, depending on the S^2PD processing condition. This improvement in the yield strength is, however, accompanied by a reduction in the tensile elongation from 80 to 40 or 50% [75]. For steels, the 35% enhancement in the tensile yield strength is accompanied by a 4% reduction in the elongation [85]. In spite of the observed reduction in ductility, no studies have been performed so far to investigate the mechanism responsible for the reduced ductility.

The motivation of the present study is to identify the factors, which could affect the ductility of a component subjected to the S^2PD process. Since S^2PD can induce multiple changes in the material properties simultaneously as pointed out above, it is important to correctly correlate the decreased ductility to the corresponding factor(s). The specific questions that are of interest may include whether the reduced ductility is caused by the surface roughness or is due to the formation of nano-grains at the surface. What is the role of other factors, such as the presence of a work-hardened surface layer and residual-compressive stresses? The answers to these questions will greatly help us clarify the mechanism responsible for the reduced ductility in S^2PD-processed materials. The fundamental understanding, if developed, can, then, be used as a guideline for optimizing the S^2PD process to minimize the reduction in the ductility.

6.2 Experimental Procedures

The material used in this work was an annealed Ni-based HASTELLOY C-2000 superalloy plate (cold-rolled and fully annealed at 1,120 $^{\circ}C$) with a 3.2-mm in thickness. It was a single-phase alloy with the face-centered-cubic (fcc) crystal structure and a nominal chemical composition (in weight percent) of 23Cr, 16Mo, 1.6Cu, 0.01C, 0.08Si, and balance Ni. Discs with 49 mm in diameter were cut out from the as-received plates. After cleaning, the disc was loaded to the cylindrical steel container of a Spex mill (SPEX/8000D Mill) and held in place via mechanical locking at one end of the container. The loading was performed in a glovebox filled with argon of purity 99.9%. Five WC/Co balls 7.9 mm in diameter were used to

provide the desired impact on the surface of the C-2000 plate. The impact velocity of WC/Co balls induced by shaking the steel container of the Spex mill was about 5 m/s. The S^2PD treatment was conducted under the stationary argon atmosphere and lasted for 30 or 180 min for both sides of the plate.

The processed plates were cut into dog-bone tensile specimens with a rectangular cross-section (3.3×3.2 mm^2) and a gage length 12.7 mm. Tensile tests were conducted on an MTS 810 test machine with a displacement control, and an extensometer was used in all the tensile tests to measure the strain. The extensometer was installed after the tensile specimen was pre-loaded with a 10 lb force (i.e., 44.48 N). After installation of the extensometer the sample was, then, deformed at a starting strain rate of 0.05 min^{-1}. The fracture surface analysis of tensile specimens was performed using a scanning electron microscope (SEM, JEOL 6335SF FESEM).

The microstructures of the C-2000 alloy before and after the S^2PD treatment were examined using both SEM and TEM (EOL 2010 FASTEM). For the TEM analysis, two orientations of samples were prepared, one being the plane-view, which has the TEM foil parallel with the impacted surface and the other the cross-sectional view with the TEM foil perpendicular to the impacted surface. The former allowed for the study of the microstructure of the impacted surface, whereas the latter permitted the investigation of the microstructural evolution from the impacted surface to the interior of the specimen.

The work-hardened profile of the specimen as a function of the depth measured from the impacted surface was determined using nanoindentation, which was conducted in a displacement-controlled mode employing a computer-controlled Nano Indenter XP System equipped with a Berkovich indenter. Data acquisitions and analyses were done in TestWorks 4 Software for Nanoindentation Systems (MTS Systems Corporation). The calibration to a polished, single-crystal aluminum standard was performed prior to the measurement. The displacement-controlled condition selected in the nanoindentation measurement gave the indent size of ~ 2 μm along one of the

Berkovich triangle edge and ~ 0.26 μm in depth. The surface roughness of samples before and after S^2PD processing was measured using a noncontact, three-dimensional, scanning white-light interferometer (NewView 5000), which can generate a 3D image of the surface contour for quantitative analyses of surface roughness. The macroscopic residual stresses in the S^2PD-processed samples were determined using X-ray diffraction (XRD).

6.3 Results and Discussion

6.3.1 Microstructures revealed by OM and TEM

Figure 6.1 shows cross-sectional images of the C-2000 specimens processed for 0, 30, and 180 min. The starting material at the annealed condition has an average grain size of 50 μm and contains a large number of annealing twins, suggesting that this material has a low stacking-fault energy. Many deformation markings are present in the 30- and 180-min processed samples. Furthermore, these deformation markings are confined within individual grains and become richer as the position moves closer to the impacted surface. Due to the low stacking-fault energy and the fcc structure, the deformation markings were identified as deformation twins. Note that for the 30-min processed sample, grain boundaries are visible everywhere except the impacted surface. In contrast, plastic deformation in the 180-min processed sample is so severe that grain boundaries and deformation markings become un-resolvable up to about 100 μm beneath the impacted surface.

Figure 6.2 presents TEM dark-field images and the corresponding selected-area diffraction (SAD) patterns of the specimens after 30- and 180-min processing. These images are taken from the very impacted surface, and reveal that nano-grains have been formed via the surface-severe-plastic deformation. The average grain sizes are 10 and 20 nm at the very impacted surface for 180- and 30-min processing, respectively. The SAD patterns indicate that these nano-grains, generated from one large grain, are polycrystalline in nature with high-angle grain boundaries between

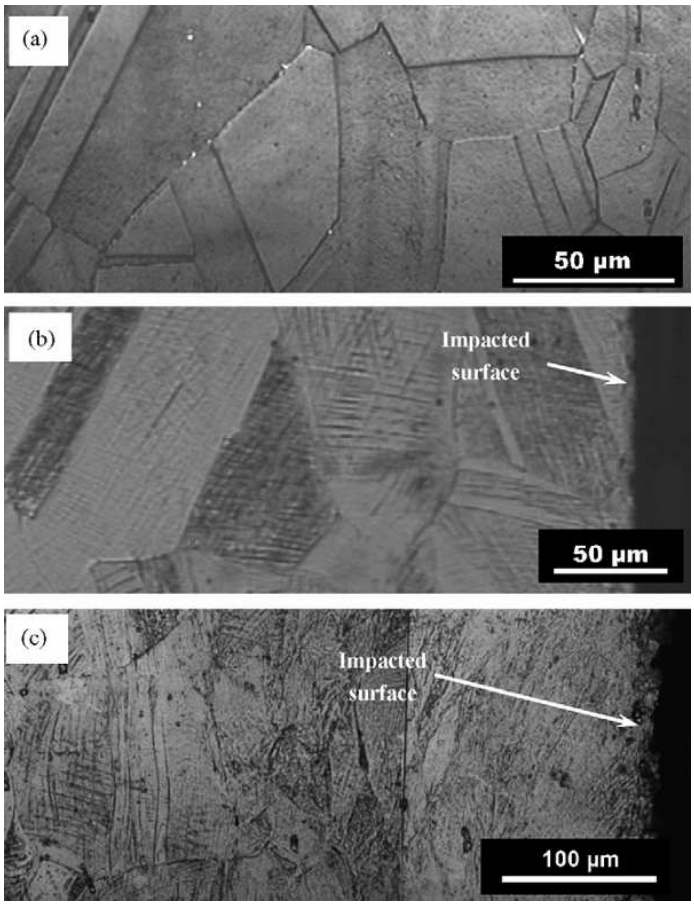

Figure 6.1: Optical images of the cross-sectional view of the C-2000 alloy (a) at the annealed condition, (b) after S^2PD processing for 30 min, and (c) after S^2PD processing for 180 min.

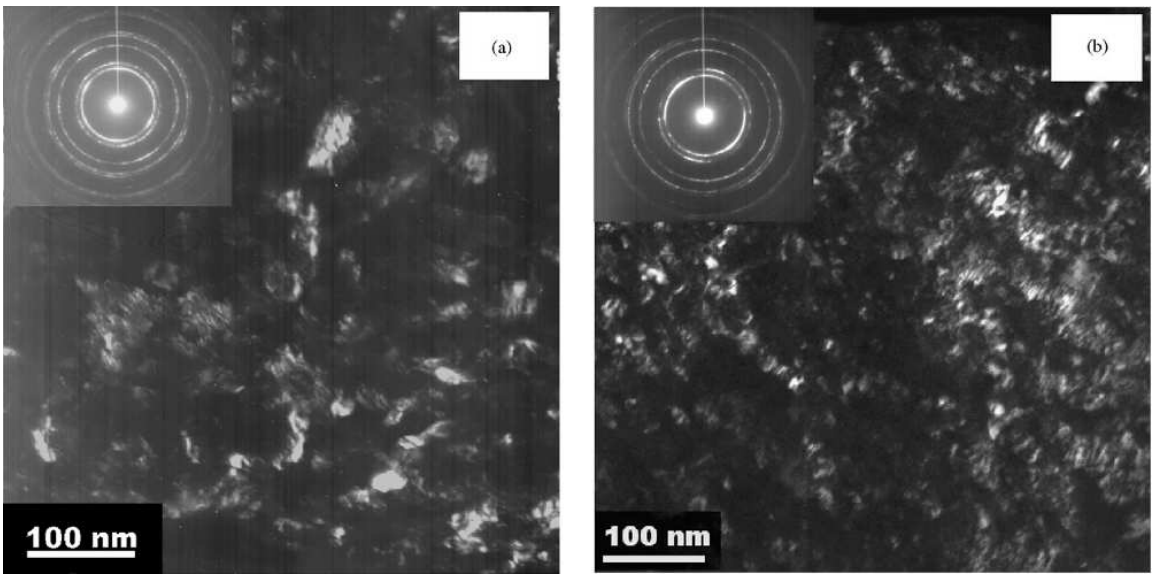

Figure 6.2: TEM dark-field images from the very impacted surface with the corresponding selected-area diffraction (SAD) patterns taken from the entire region shown in the corresponding dark-field images: (a) after S^2PD processing for 30 min and (b) after S^2PD processing for 180 min. Note that fcc polycrystalline rings are present in both SAD patterns.

themselves. The thickness of the nanocrystalline surface layer is about 50 μm for 180-min-processed samples, whereas it is less than 5 μm for 30-min processed samples, as shown in Chapter 3.

Figure 6.3 shows the residual in-plane stress distribution in the C-2000 sample after 30-min processing. The stress profile was obtained by a layer-by-layer removal followed by a X-ray diffraction scanning. Note that the residual stress distribution as a function of the position is very similar to that generated from shot peening with the peak residual compressive stress appearing at a sub-surface region. Such a similarity is not a surprise because both shot peening and the S^2PD process used in this study rely on repeated impacts of shots and balls. The difference between shot peening and S^2PD processes is that balls in S^2PD are much larger than those in shot peening. As a result, S^2PD processes have higher kinetic energies, and can produce a thicker work-hardened region, a thicker nano-grained surface layer, and larger compressive-residual stresses than shot peening.

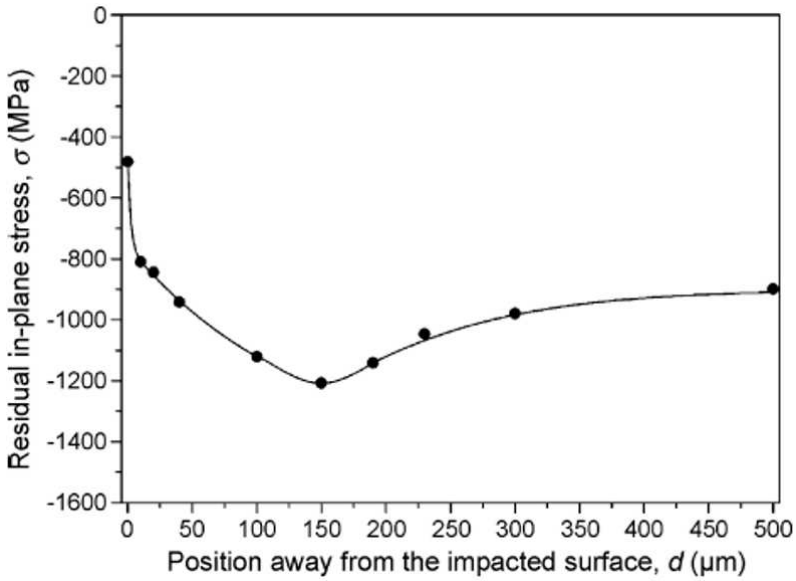

Figure 6.3: The residual in-plane stress profile of the sample with S^2PD processing for 30 min as a function of the position measured from the impacted surface.

Specifically, the residual in-plane compressive stress at the impacted surface of the 30-min processed sample is approximately 500 MPa, whereas the peak compressive residual stress of about 1,200 MPa appears at the sub-surface ($\sim$ 150 μm away from the impacted surface). Residual stresses in the 180-min processed sample have not been measured yet. However, it is expected that the magnitude of the compressive residual stresses in the 180-min processed sample is higher than that in the 30-min processed sample because the former exhibits more bending than the latter when only one side of the plate was S^2PD-processed. Note that the radius of the bending curvature has long being used to estimate the magnitude of compressive-residual stresses produced from shot peening on one side of the plate. However, the detailed stress profile cannot be derived from the radius of curvature, because different residual stress profiles can lead to the same radius of curvature.

6.3.2 Stress-strain behavior

The tensile stress vs. strain curves of C-2000 specimens are shown in Fig. 6.4. Note that both the 0.2% offset yield strength and ultimate tensile strength have

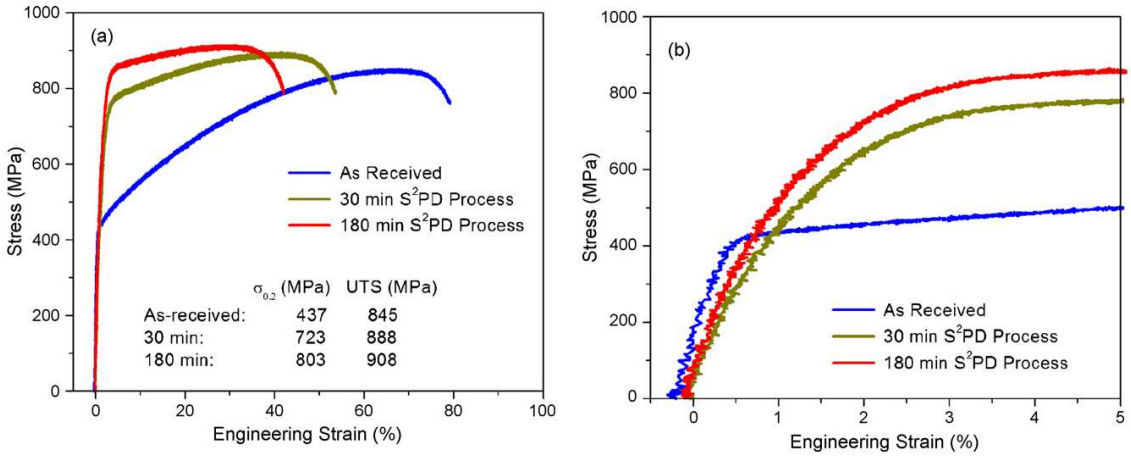

Figure 6.4: Tensile stress-strain behavior of various samples with and without S^2PD processing as indicated: (a) overall stress-strain curves and (b) the blow-up of the stress-strain behavior at the early stage of deformation. The origins of the tensile stress-strain curves in (b) have been shifted slightly to facilitate the observation of the slopes of the stress-strain curves.

been improved via S^2PD processing. Specifically, the 0.2% offset yield strength has been increased by $\sim$ 65% and $\sim$ 84% for the 30- and 180-min processed samples, respectively, over the annealed sample. The tensile elongation, however, decreases from about 60% for the annealed sample to 40% and 30% for the samples with 30- and 180-min processing, respectively. Additionally, it is noted that the elastic modulus of the specimen, as gauged from the slope of the stress-strain curve at the elastic deformation range, has decreased after S^2PD processing (Fig. 6.4b). This change in the elastic modulus (to be discussed more below) has resulted in some difficulty in determining the 0.2% offset yield strength precisely. Nevertheless, the 0.2% offset yield strength was estimated using the elastic portion of the stress-strain curve in Fig. 6.4(a) (i.e., the low stress portion of the stress-strain curve) to construct a line with a 0.2% strain offset from the origin, and defining the yield strength based on the intersection of the line with the stress-strain curve.

With a simple equation, $\varepsilon_{true} = \ln(1 + \varepsilon_{engineer})$, the engineering strain, $\varepsilon_{engineer}$, can be converted to the true strain, ε_{true}. Further, the true strain to fracture, $\varepsilon_{true(total)}$, can be further divided into two sub-strains, the uniform true strain before necking, $\varepsilon_{true(unit)}$, and the true strain after the onset of necking, $\varepsilon_{true(neck)}$. As

summarized in Table 6.1, the uniform true strain before necking decreases from 0.52 for the annealed sample to 0.35 and 0.28 for the 30- and 80-min processed samples, respectively. However, the true strain after the onset of necking changes little with the processing condition.

Table 6.1: Ductility parameters of C-2000 alloy

Sample ID	Engineering strain	Total true strain	Uniform true strain	Necking true strain	Reduction of area (%)
As-Received	0.79	0.58	0.52	0.06	73.9
L30	0.54	0.43	0.35	0.08	57.3
L180	0.41	0.34	0.28	0.06	54.2

It is found that the true stress-strain curves (from the onset of yielding to the maximum load) of all samples can be approximately described by Hollomons relation, $\sigma = K\varepsilon^n$, where σ and ε are the true stress and true strain, respectively, K is a material constant, and n is called the strain-hardening coefficient. In this study, n is found to be 0.47 for the as-annealed sample, whereas the corresponding values for the samples with S^2PD processing for 30 and 180 min are 0.31 and 0.24, respectively. According to Considère's criterion [161], the uniform true strain is numerically equal to the strain-hardening coefficient for a material exhibiting Hollomons relationship. However, the strain-hardening coefficients obtained from the C-2000 alloy are lower than the corresponding uniform true strains (i.e., 0.52 vs. 0.47, 0.35 vs. 0.31, and 0.28 vs. 0.24). Since the discrepancy between the strain-hardening coefficient and the uniform true strain is also present in the annealed sample, this phenomenon suggests the presence of the effect of the strain-rate sensitivity on the uniform true strain of this alloy, based on Harts criterion [162].

However, it is noted that the discrepancy increases with the S^2PD processing time (i.e., the ratio of the strain-hardening coefficient to the uniform true strain decreases from 0.90 for the annealed sample to 0.88 and 0.86 for the 30- and 80-min processed samples, respectively). The fact that different samples display different degrees of discrepancy, while they have a similar post-necking strain and, thus, a similar strain-rate sensitivity indicates that the discrepancy between the strain-hardening

coefficient and the uniform true strain in S^2PD-processed samples must also be affected by other factors. One additional source for the discrepancy in S^2PD-processed samples is the presence of different strain-hardening capabilities in the surface region of the sample. The strain-hardening coefficient of the S^2PD-processed sample is actually the average of the strain-hardening coefficients of different regions within the sample. Previous studies [8] have shown that strain hardening of nc materials is high. However, such high strain hardening is lost quickly on deformation owing to their very low dislocation storage efficiency inside the tiny grains [163]. As a result, the tensile ductility of nc materials is typically lower than that of the coarse-grained counterparts [163]. On compression, however, nc materials can exhibit substantial strains before fracture, even though the stain-hardening coefficient has decreased to near zero after a small amount of plastic deformation.

Taking together all of these previous observations, it is proposed that the lower strain-hardening coefficients of S^2PD-processed samples in comparison with that of the annealed sample is partially due to the quick loss of the strain-hardening capability of the nc surface layer in S^2PD-processed samples. Such a quick loss in the strain-hardening capability also contributes to the large discrepancy between the strain-hardening coefficient and the uniform true strain observed with the S^2PD-processed samples. Additionally, the presence of a work-hardened surface region in S^2PD-processed samples also contributes to their lower strain-hardening coefficients. This conclusion is consistent with the fact that a material that exhibits Hollomons relation would display a lower strain-hardening coefficient after some prior plastic deformation.

The above proposition can also offer a consistent explanation for a continuous decrease in the strain-hardening coefficient and the increased discrepancy between the strain-hardening coefficient and the uniform true strain, as the S^2PD-processing time increases. The TEM results have already shown that the nc surface layer in the 30- min processed sample is very thin (less than 5 μm), whereas the thickness of the nc surface layer in the 180-min processed sample is about 50 μm. Thus, the

decreased strain-hardening coefficient and increased discrepancy between the strain-hardening coefficient and the uniform true strain in the 30-min processed sample is mainly attributed to the presence of the work-hardened surface region. However, the further decreased strain-hardening coefficient and further increased discrepancy between the strain-hardening coefficient and the uniform true strain in the 180-min processed sample is due to the combined effect of a nc surface layer and the work-hardened surface region. This statement is supported by similar microhardness values of the surface regions for 30- and 180-min processed samples. Therefore, the additional decrease in the strain-hardening coefficient and further increased discrepancy between the strain-hardening coefficient and the uniform true strain in the 180-min processed sample must be related to the presence of the nc surface layer. The reduced strain-hardening coefficients, in turn, result in lower uniform true strains and, thus, less ductility in S^2PD-processed samples. The macroscopic residual stresses and high surface roughness induced by S^2PD, however, appear to have little influence on the uniform true strain, as will be discussed in the next several sections.

6.3.3 Overall fracture morphology and fractography

The overall fracture morphologies of the tensile specimens are presented in Fig. 6.5. Note that the annealed sample exhibits a cup-and-cone fracture, a typical fracture behavior of ductile materials under tension. However, the overall fracture morphology has changed from the cup-and-cone fracture to a shear fracture after S^2PD processing. Necking is still very obvious in the S^2PD-processed samples. However, the degree of necking has decreased in comparison with the annealed sample. As summarized in Table 6.1, the reduction of area has decreased from 74% for the annealed sample to 57% for the 30-min processed sample and to 54% for the 180-min-processed sample.

Accompanied with the changes in the tensile elongation, the reduction of area, the uniform true strain, the strain-hardening coefficient, and the overall fracture morphology, the fracture surface morphology has also been altered dramatically

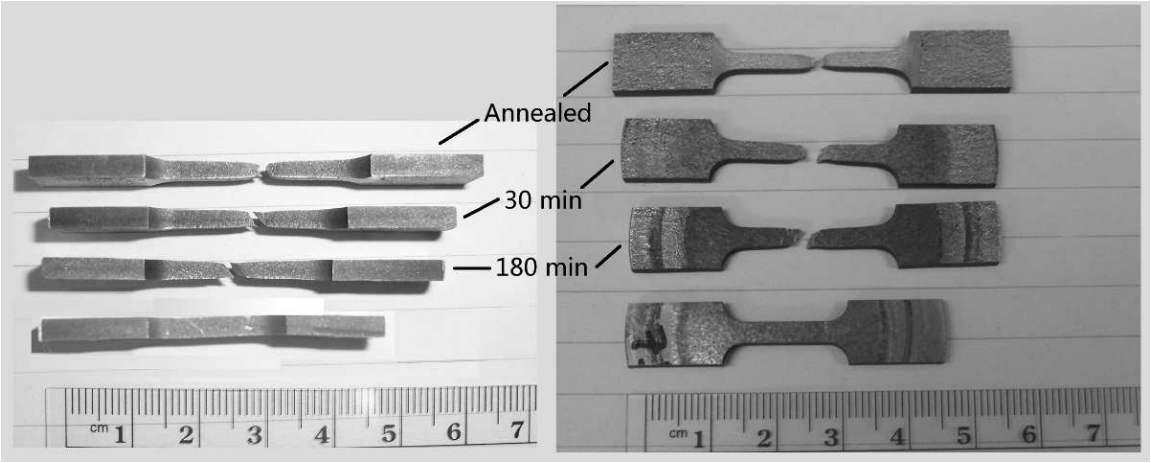

Figure 6.5: Macroscopic fracture morphology viewed in two orientations of the tensile-tested specimens with three conditions: (i) as-received (in an annealed condition), (ii) S^2PD processed for 30 min, and (iii) S^2PD processed for 180 min.

by S^2PD processing. Shown in Fig. 6.6 are the fracture surfaces of the annealed sample at the central and edge regions. Being consistent with the cup-and-cone fracture morphology, the central region [Fig. 6.6(a)] exhibits extensive equiaxed dimples. The depth of some dimples reaches about 10 μm, indicating substantial plastic deformation of the boundaries between micro-voids before local separation of the void boundaries. At the edge region where oblique shear rupture occurs at the cone portion of the fracture, slightly elongated dimples with a much reduced depth are present [Fig. 6.6(b)]. Such a change in the dimple morphology is consistent with the detailed study by Beachem [164] who has revealed that dimples on the shear-rupture surface are elongated, pointing in the direction of the relative shear motion for that half of the specimen. Figure 6.7 presents the fracture surfaces of S^2PD-processed samples, showing substantial changes in the dimple morphology at the central region of the specimen in comparison with the annealed sample. For the sample S^2PD-processed for 30 min, elongated dimples are present at the central region [Fig. 6.7(a)]. This trend is entirely consistent with the shear fracture mode found in Fig. 6.5. The sample with 180-min of S^2PD processing exhibits further changes in the central region, showing dimples with a shallow depth [Fig. 6.7(b)]. The decreased depth of dimples from 30- to 180-min processed samples is a reflection of the decreased plastic deformation of the boundaries between micro-voids before the local separation of the void

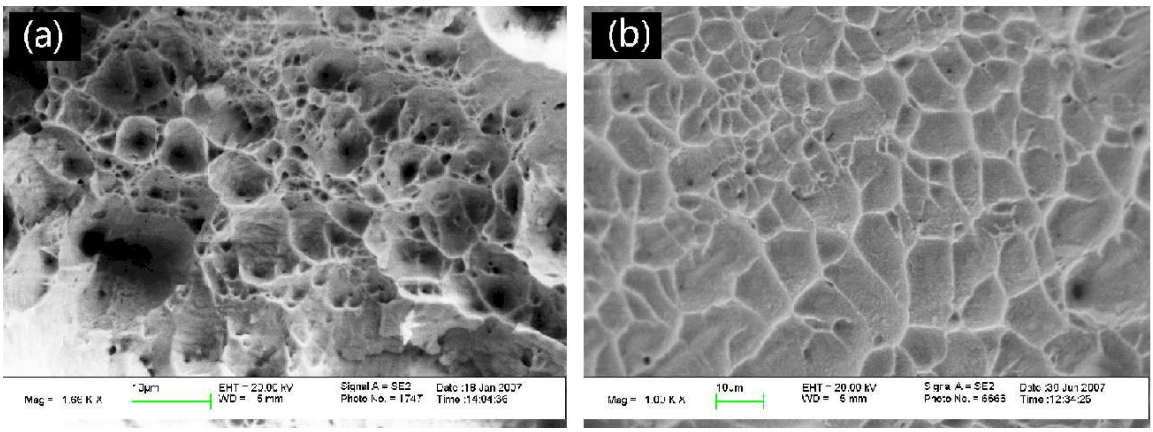

Figure 6.6: Fracture surfaces of the annealed sample with (a) from the center and (b) from the edge of the specimen.

boundaries. Such a change in the fracture-surface morphology is in good accordance with the measured tensile ductility and the reduction of area (Fig. 6.4 and Table 6.1). The fracture surfaces at the edge regions for 30- and 180-min-processed samples are similar, showing slightly elongated dimples with very shallow depth [Fig. 6.7(c)].

The change in the fracture-surface morphology from more ductile to less ductile manner as the S^{2}PD-processing time increases may be explained by a recently-proposed-unified-tensile fracture criterion [165]. This new criterion states that the fracture modes of all materials can be related to an α factor defined as $\alpha = \tau_0/\sigma_0$, where τ_0 and σ_0 are the critical normal and shear fracture stresses, respectively. The annealed C-2000 sample is a typical coarse-grained metal and, thus, has a very low value of α, ($\alpha \ll 0.3$) [165], which leads to a substantial shear fracture in both the center and edge of the specimen. In contrast, the S^{2}PD-processed samples have a nc surface layer which would have a high value of ($0.3 < \alpha < 0.6$) [165]. As a result, the degree of shear fracture, manifested as the depth of dimples, is decreased at the edge of the S^{2}PD-processed samples. The change from the equiaxed dimple to elongated dimple in the center of S^{2}PD-processed samples is presumably due to the crack initiation at the surface region and subsequent propagation through the central region to the other side of the specimen by shear fracture. The crack initiation site change from the center for the annealed sample to the surface for the S^{2}PD-processed sample

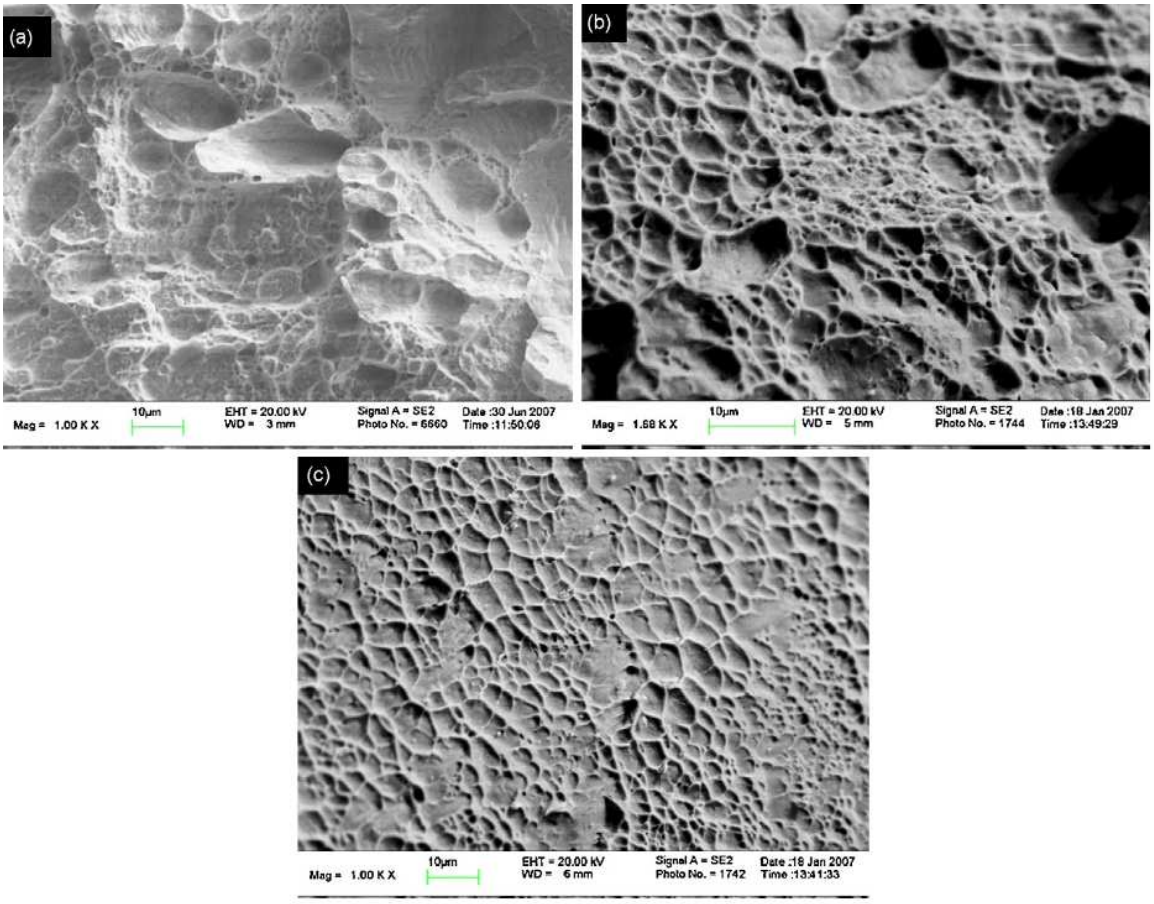

Figure 6.7: Fracture surfaces of S^2PD-processed samples with (a) from the center of the 30-min processed sample, (b) from the center of the 180-min processed sample, and (c) from the edge of the 180-min processed sample.

is supported by the presence of many corner cracks in the S^2PD-processed samples near the necking region, and attributed to the lower ductility of the nc surface layer.

6.4 Summary

The reduced tensile ductility of a Ni-based C-2000 alloy induced by S^2PD has been investigated via systematic experiments. In particular, effects of the macroscopic residual stress, work-hardened region, nc surface layer, and surface roughness present in S^2PD-processed samples have been studied. Based on this investigation, the following conclusions can be offered.

1. S^2PD processing decreases the tensile ductility of the C-2000 alloy. The longer the S^2PD processing time, the more reduction in the ductility. However, the remaining ductility after reduction (40%) is still more than sufficient for engineering applications.

2. S^2PD processing leads to decreases in the strain-hardening coefficient, the uniform true strain, and the reduction of area.

3. The overall fracture morphology of tensile specimens has been changed from the cup-and-cone fracture for the annealed sample to the shear fracture for S^2PD-processed samples.

4. The reduced uniform true strain is mainly related to the decreased strain-hardening coefficient, which, in turn, is caused by the presence of the nano-grained surface and the work-hardened surface region created via S^2PD.

5. The nano-grained surface and the work-hardened surface region created via S^2PD also result in higher tensile stresses at the surface region than those at the central region of the specimen. These high surface tensile stresses, in turn, lead to the formation of the fatal crack at the surface of the S^2PD-processed specimen, thereby changing the cup-and-cone fracture for the annealed sample to the shear fracture for S^2PD-processed samples.

6. The residual compressive stresses created via S^2PD have little influence on the ductility of the specimen. Instead, these compressive stresses only extend the apparent elastic strain of S^2PD-processed samples.

7. The high surface roughness of S^2PD-processed samples does not have much influence on the ductility. However, surface roughness may play a role in changing the cup-and-cone fracture for the annealed sample to the shear fracture for S^2PD-processed samples.

CHAPTER 7

A Study on the Surface-Severe-Plastic-Deformation Behavior of a Zr-based Bulk-Metallic Glass (BMG)

7.1 Introduction

The potential application of bulk-metallic glasses (BMGs) is so closely dependent on their plasticity that extensive research has been conducted to investigate their plastic-deformation performance at room temperature [14, 15, 111, 137, 166–170]. Some popular experimental setups, such as the indentation, compression, bending, etc., are widely used to exert different loading modes on the amorphous material to generate the plastic deformation. According to the results of those studies, it has been established that the inhomogeneous shear-band operation is the characteristic of the deformation in the BMGs at room temperature [14–16]. In order to improve the ductility of BMGs, both extrinsic and intrinsic methods have been proposed to suppress the propagation of shear bands in recent years. An example of the former method is to optimize the geometry of the sample so that shear bands would not propagate to the free surface [15, 16], while that of the latter is to introduce reinforcements into the material so as to retard the propagation of the shear band [17, 18]. However, the continuous emergence of papers regarding the plastic deformation of BMGs indicates that this issue is far from clear.

Partially due to the fact that BMGs are easy to fracture before enough plastic deformation could be accumulated within the material, there are few studies on the effects of the plastic deformation on the mechanical properties of BMGs. A recent work by Zhang et al. showed that the shot-peening process would decrease the

hardness of a Zr-based BMG in a certain thickness of the surface layer [134]. Similar results were also reported by Bei et al. in a compression test [16]. However, in some other studies, both work hardening [110, 133] and flow softening [137] were reported under deformation caused by nanoindentation. It is also noted that those studies were based on a moderate localized plastic deformation, e.g., the deformation zone is limited to a small region or a very shallow layer. The evolution of the microstructures under further deformation and its effects on the material properties are still of great interest.

In the present study, a surface-severe-plastic-deformation (S^2PD) process, which has been successfully applied on a Ni-based polycrystalline alloy to form surface plastic deformation [74, 76, 87, 88, 149, 159], is modified and utilized on a Zr-based BMG to generate a severe plastically-deformed near-surface layer in the material, and the effects of the deformation layer on the microstructures and mechanical properties of the materials are investigated.

7.2 Experimental Procedures

The material used in this work is a Zr-based $Zr_{50}Cu_{40}Al_{10}$ (in atomic percent) BMG, which was prepared by arc-melting mixtures of pure Zr, Cu, and Al metals in an argon atmosphere. A low-oxygen-concentration Zr ($<$ 0.05 at.% oxygen) rod was used to minimize the oxygen content in the alloy. A tilt-casting method was implemented to cast the alloy to its final rod shape of 60 mm and diameter of 8 mm [141].

The rod samples were cut to rectangular bars with a geometry of $3.0 \times 3.0 \times 25$ mm^3. After polished using the 2,400-grit grinding paper, the bars were mechanically attached to the cover of a cylindrical container. Twenty WC/Co (with 5% Co in weight percent, wt.%) balls with a diameter of 1.6 mm each were put into the container, which was, then, sealed with the cover in an pure argon atmosphere. Finally, the container was clamped into the Spex 8000 miller and subjected to back-and-forth vibration movements with a frequency of 60 Hz. Figure 7.1 shows the equipment used

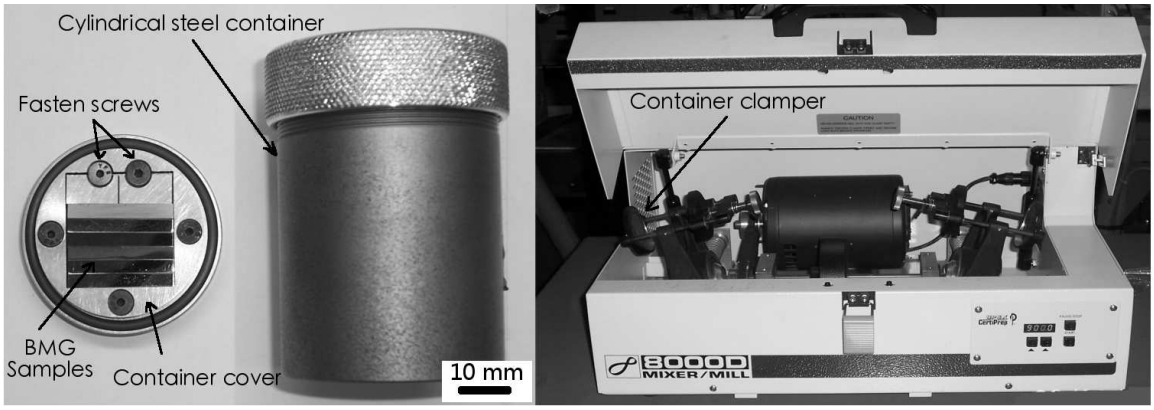

Figure 7.1: Equipment used to introduce severe-plastic deformation in the near-surface layer of the BMG samples.

in this study. Note that in order to minimize the overall temperature rising, the process is stopped every 15 min to fully dissipate the generated heat. With these setups, the balls would impact the sample surface with an average energy much higher than that of the shots, which were used in a shot-peening process [135], thus generate a severely-deformed near-surface layer in the BMG at room temperature. The bombardment process was lasted for 60 and 180 min, respectively, to obtain two different specimens, each with the S^2PD treatment on one surface.

Sample pieces with a dimension of 2×2 mm^2 and thickness 0.3 mm, which were cut from the treated surface and carefully polished to its final shape, were used to measure the thermal properties of the deformed specimens in a Perkin-Elmer Diamond Differential-scanning-calorimeter (DSC) at a heating rate of 30 K/min under a constant flow of high-purity argon. X-ray diffraction (XRD) analyses were conducted using a Philips's X'pert diffractometer to characterize the near-surface structure of the specimen before and after the S^2PD process.

A synchrotron high-energy X-ray diffraction experiment was conducted at the 11-ID-C beamline at the Advanced Photon Source (APS), Argonne National Laboratory, for inspecting the minor crystal phase contained in the samples. The beam size used is 400 μm (parallel to the treated surface) $\times$ 20 μm (along the normal direction of the treated surface), and the wave length is 0.107560 Å. A two-dimension (2-D) Image plate, Mar345, was used as the area detector for collecting the diffraction

patterns. The synchrotron sample was cut from the processed bar and had a geometry of $2 \times 2 \times 1.5$ mm^3, with the thickness, 1.5 mm, along the longitude direction of the bar. Diffraction data from the treated surface to the less-affected interior are collected and compared. It should be noted that the high-energy X-ray diffraction technique used in the present investigation provides a very powerful and sensitive tool for characterizing a tiny volume of crystalline phases among the amorphous matrix, due to the high flux and high resolution of the high-energy X-ray beam produced by the synchrotron source and the 2-D area detector used in the present technique, respectively.

Nanoindentation was conducted in a load-controlled mode employing a computer-controlled Nano Indenter XP system equipped with a Berkovich indenter. Data acquisitions and analyses were done in TestWorks 4 Software for Nanoindentation Systems (MTS Systems Corporation). The calibration to a polished, single-crystal aluminum standard was performed prior to the measurements. A 10-gf (i.e., 0.098 N) load was applied in each test, and the measurement was along multiple lines beginning approximately 10 μm from the processed surface and extending approximately 1 mm into the center of the material. Additional indents were made in the near-surface region. The average indent depth was approximately 900 nm.

Four-point-bending-fatigue test were preformed in a computer-controlled Mste-rial Test System (MTS) servohydraulic testing machine with a fixed R ratio (where $R = \sigma_{min}/\sigma_{max} = 0.1$, σ_{min} and σ_{max} are the applied minimum and maximum stresses, respectively) and different stress levels. Using a load-controlled bending-fatigue test, the nominal stress, σ_{nom}, has the following relationship with the applied load on each pin:

$$\sigma_{nom} = \frac{3P(L-t)}{2Wh^2} \tag{7.1}$$

where P is the force applied, L and t are the distances between two outer and two inner pins, respectively. While W and h are the width and height of the rectangular sample, respectively. The fractography of the fatigue samples were examined using a Leo 1526 scanning-electron microscope to study fatigue and fracture mechanisms.

7.3 Results and Discussion

Figure 7.2 shows the SEM observations of the side surface of the sample treated with 180 min. It is shown that layer-by-layer features in the near-surface region is formed by the flow-out material during the process, since at the edge, there is little constraint. This is a good illustration that this BMG material can undergo severe-plastic deformation without brittle fracture at room temperature under certain conditions. A similar confirmed result is that during a compression test, a huge amount of plastic deformation can be accumulated before the final fracture when the aspect ratio of the sample is very small [15, 16]. Below the flow-out layer, a large amount of deformation boundaries can be observed, where each extrusion and/or intrusion line is believed to be composed of numerous fine shear bands. It can also be estimated from the figure that the plastic deformation can reach at least 120 μm from the processed surface, which is deep enough to affect the overall mechanical properties of the material.

The amorphous phase of the as-casted specimen is confirmed by the X-ray diffraction spectrum shown in Fig. 7.3. It is noted that for both of the two plastically-deformed samples, crystalline diffraction peaks are superimposed on the broad amorphous peak, indicating the presence of crystal phases in these samples. It is believed that the crystalline particles are some $ZrCu$ phase though further experiment is needed to confirm the detailed composition [171]. The 2-D synchrotron-diffraction patterns of the 180-min processed sample are shown in Fig. 7.4. Those diffractions are taken at different positions, i.e., 60, 100 and 460 μm, away from the processed surface. Obviously, the bright spots (corresponding to a high intensity) should come from the crystal phase rather than amorphous phase. It is noted that lesser and lesser crystalline diffractions are detected by the 2-D detector from the surface to interior, which shows that more crystalline phases were contained in the near-surface layer but less in the interior. The diffraction patterns at those letter-indicated positions are shown in Fig. 7.5, which was obtained by caking the 2-D diffraction pattern within a small angle ($\sim 0.6^{\circ}$) around the letter-indicated positions. From Fig. 7.5, it

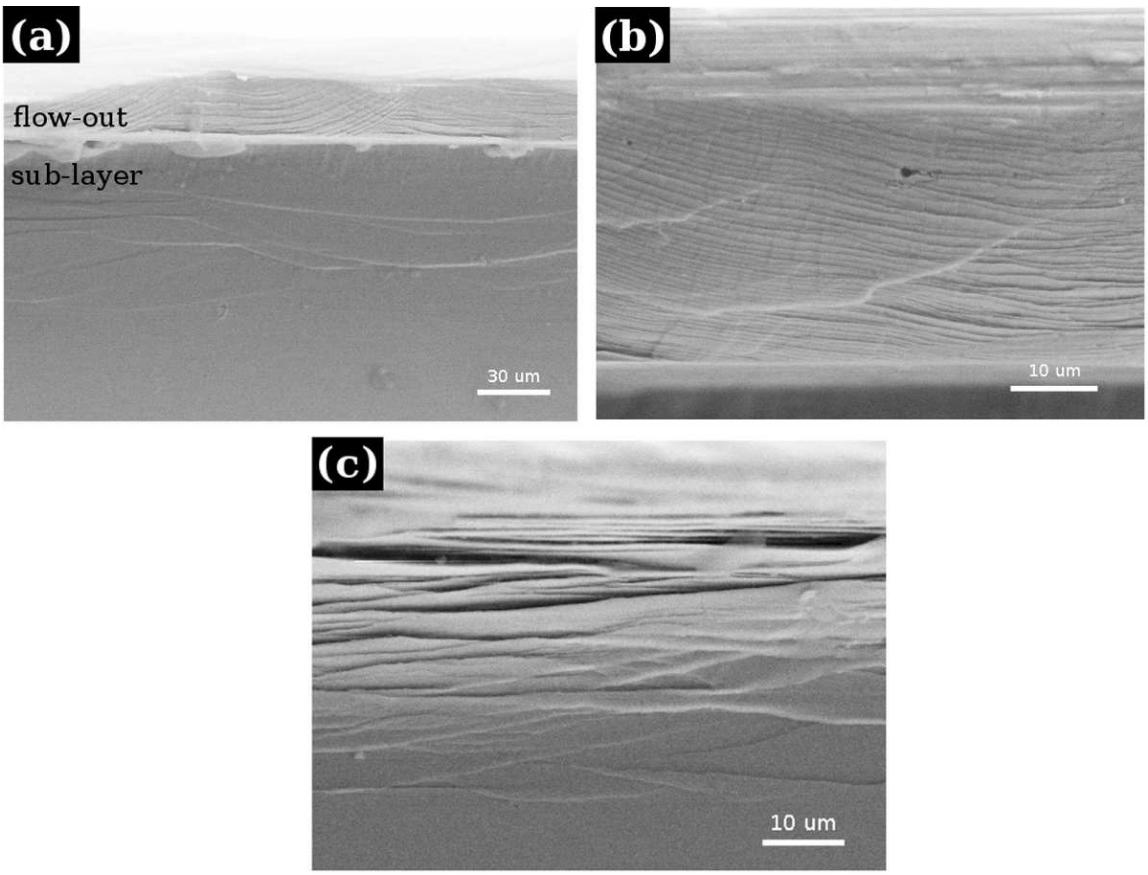

Figure 7.2: SEM observations on the side surface of the BMG subjected to the surface-severe-plastic deformation (a). The image shows two distinct layers: flow-out surface layer (b) and sub-layer with deformed marks (c).

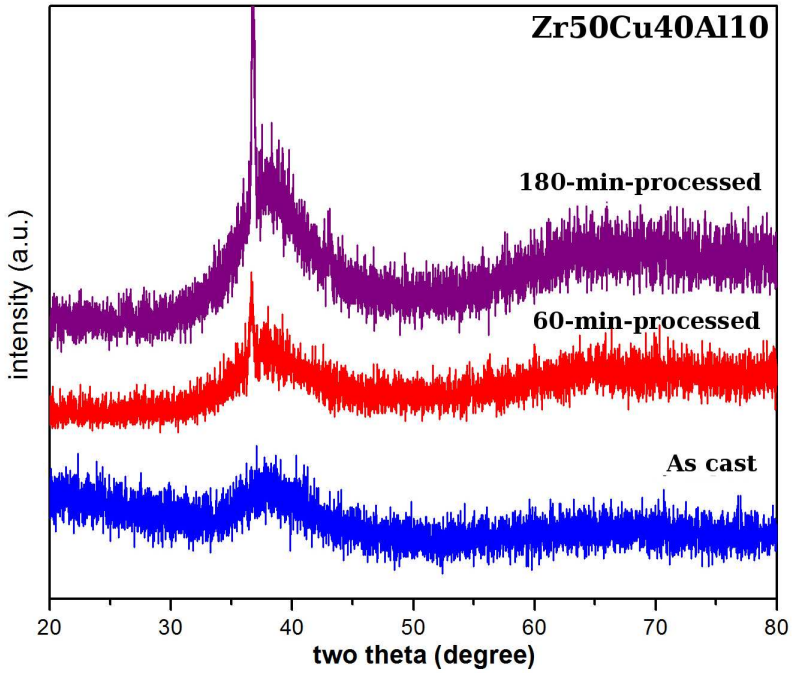

Figure 7.3: XRD spectra of the as-casted and the S^2PD-processed BMG sample. Note that only the processed samples have the crystal diffraction peaks.

is known that the white spots in Fig. 7.4 indeed represent the crystal phase in the material. Though there might be a few high intensity spots, which could be argued to be crystalline phase formed initially during the casting process, we can still make the conclusion that crystallization occurs during the process due to: (1) the beam size (400 μm $\times$ 20 μm) is large enough to make the results statistically meaningful; (2) the diffraction patterns are compared under exactly the same conditions (i.e., the same contrast and brightness) and the trend remains the same no matter how we transform the patterns; (3) the crystallization did occur under some other severe-plastic deformation processes. e.g., nanoindentation [118, 172]; and (4) the conventional XRD and synchrotron high-energy XRD diffraction give the consistent results.

The thermal behaviors of the as-casted and the severe-plastic-deformed BMG samples are compared through the DSC curves as shown in Fig. 7.6. It is known that the heat absorbed during the relaxation period is an indication of the change of free volumes. i.e., the integrated area under the exothermic peak is proportional to the free volume in the material [173]. With this principle, it is noted that extra

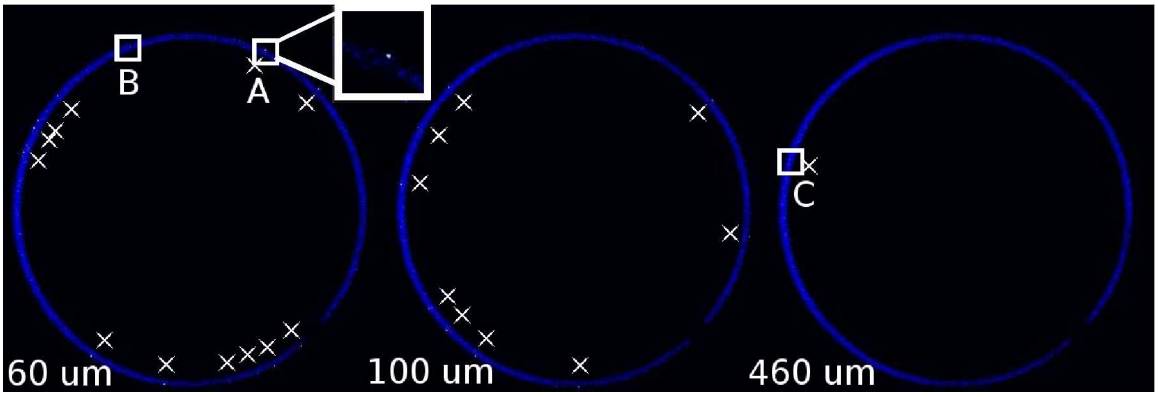

Figure 7.4: Two dimensional (2-D) synchrotron-diffraction patterns with the intensity higher than 3,930 at different positions (60, 100, and 460 μm) from the surface, respectively. The white spots represent high diffraction intensities. Point A is believed to be a crystal-diffraction peak, point B is an arbitrarily selected point without a white spot, and point C is the highest intensity point in the as-cast sample. Note that only the first diffraction rings are shown here, and crystal peaks may also appear in the (unshown) second diffraction rings.

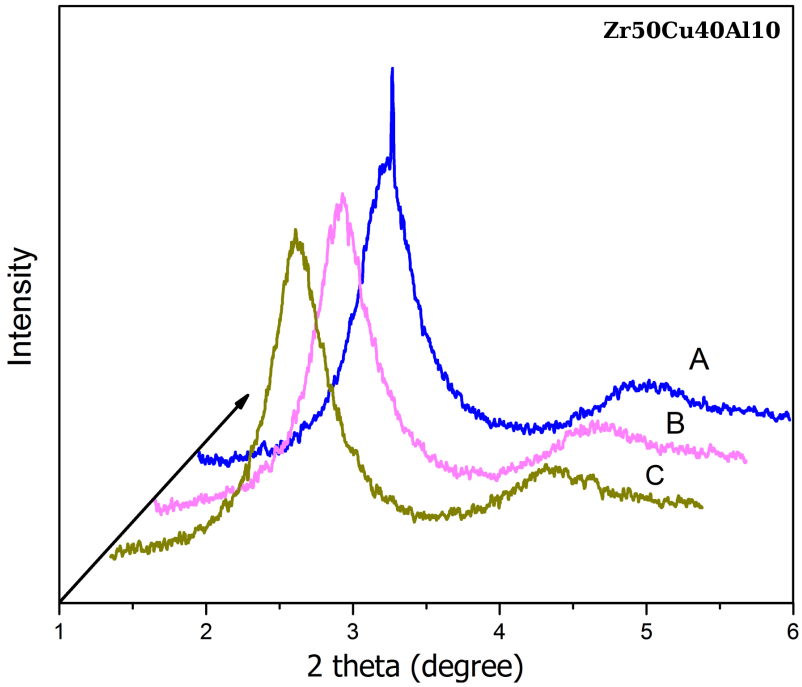

Figure 7.5: The 1-D diffraction patterns corresponding to point A, B and C. It is shown that there exhibits an obvious crystal diffraction peak at point A.

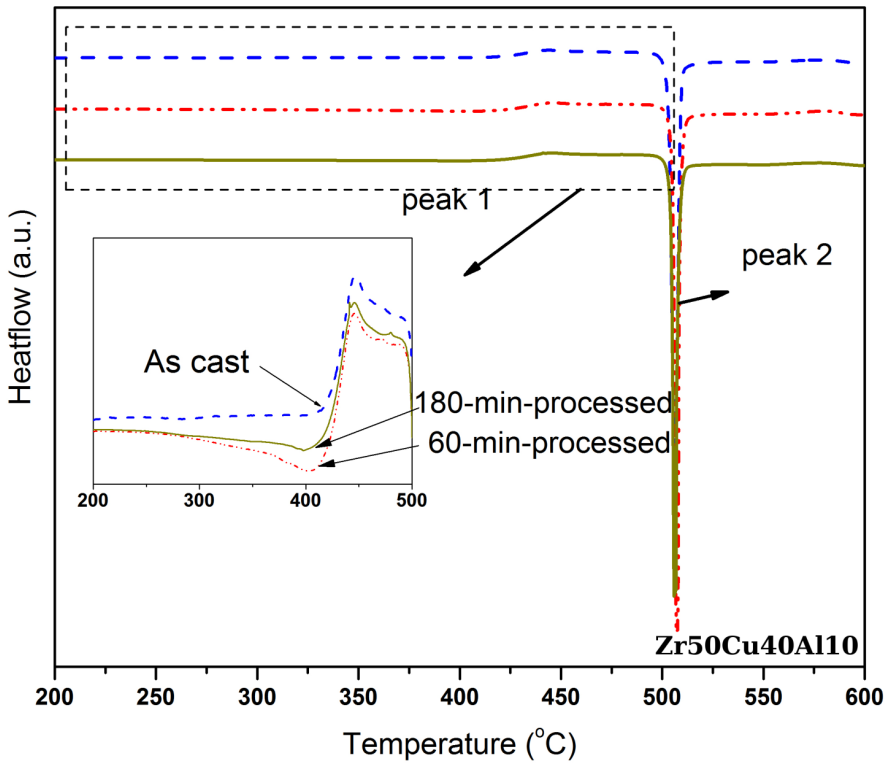

Figure 7.6: DSC curves of the as-casted and the S^{2}PD processed BMG samples.

free volumes are generated during the S^{2}PD process. However, compared with the 60-min-processed sample, the free volume in the 180-min-processed-sample actually decreases. This trend might be due to the reason that a long processing time gives the atoms enough time to (1) to rearrange themselves to corresponding preferred positions so as to generate some nanometer-scale voids [174, 175]; and (2) to form nanocrystallines, as shown in the above-mentioned results.

Some other thermal features of the specimens are summarized in Table 7.1, from which it is known that the glass-transition temperature, Tg, and the crystallization temperature, Tx, did not change much with the deformation process. Therefore, Tg and Tx might not be sensitive to the severe plastic deformation in this case. On the other hand, the heat absorbed (indicated as ΔH_2) during the crystallization period, i.e., the integrated area under the crystallization peak, has pronouncedly decreased as the processing time increases. One possible explanation for this change is that the partial crystallization and atom rearrangement have occurred during the deformation

Table 7.1: Thermal properties of the $Zr_{50}Cu_{40}Al_{10}$ BMG subjected to the surface-severe-plastic-deformation process

Sample	Tg(℃)	Tx(℃)	$\Delta H_1(J/g)$	$\Delta H_2(J/g)$
As-Cast	422.8	501.9	4.41	45.9
60 min	421.7	502.3	3.04	42.7
180 min	420.5	504.0	2.75	36.4

process for the treated samples. Therefore, the energy needed to crystallize unit mass glasses decreases.

A microhardness profile of the samples measured by the nanoindentation is shown in Fig. 7.7. The hardness for the interior of the glass is 6.6 GPa. The maximum hardness measured for the 180-min-processed sample is 7.6 GPa, whereas the corresponding value for the 60-min-processed sample is 7.3 GPa. It is interesting to find that both work hardening and work softening were observed in this case. In general, the nano-hardness gradually increases as the position changes from 1,000 to 100 μm measured from the processed surface. However, when the position is approaching the very impacted surface (i.e., about 100 μm or less from the impacted surface), the hardness appears to decrease. Note that edge rounding in the near-surface region may have an effect on the exact hardness values in the extreme near-surface region, as the indent-contact area may not be computed precisely because of the slightly elongated triangles. Nevertheless, there is no doubt that the overall trends for both samples are similar, i.e., exhibiting softening in the very impacted layer.

Zhang et al. [134] found a softened near-surface layer in a shot-peened BMG and attributed the change of hardness to the residual stress, which is also applicable to this study. However, since the impact energy in this investigation is tens of times higher, and the processing times are more than 100 times longer than those in the shot-peening process (A detailed comparison about these two processes can be found

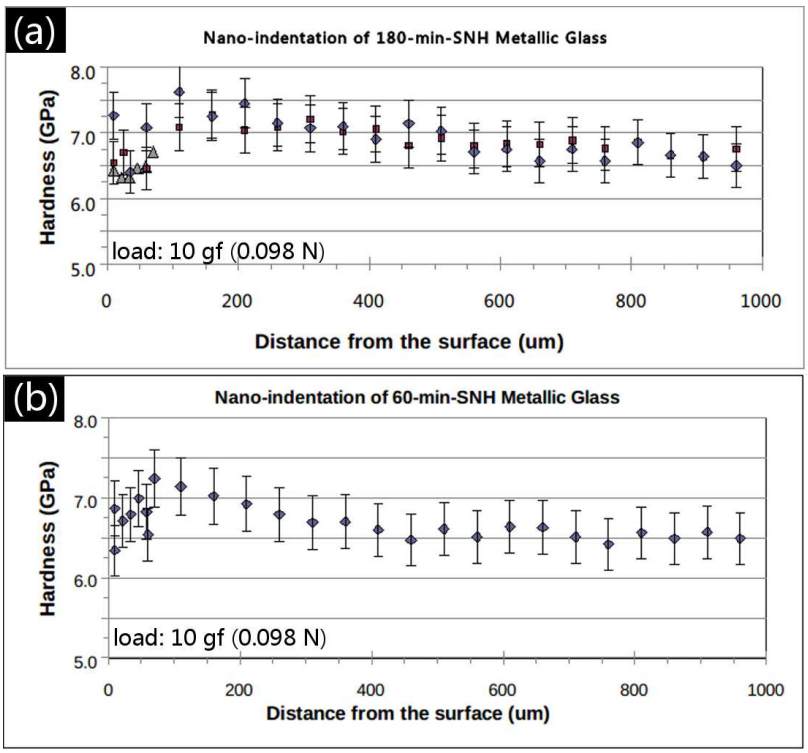

Figure 7.7: Hardness profiles of the 60-min (a) and 180-min (b) S^2PD-processed $Zr_{50}Cu_{40}Al_{10}$ BMG.

elsewhere [135]), it is believed that other effects, such as the free volume and formation of nanocrystallites, may also increase the resistance to the indentation, so as to improve the hardness. Therefore, the different hardness profiles between the current study and Zhang et al.'s result might be attributed to the different degrees of the plastic deformation. A systematic study on the hardness profile is in active progress.

The high-cycle fatigue properties of the specimens before and after the surface treatment are shown in Fig. 7.8. In the low-cycle-fatigue range (the fatigue life lower than 10^5 cycles), there is no detectable difference in the fatigue behaviors between the as-casted and the processed samples, i.e., all the data points are distributed around the same line. However, in the high-cycle-fatigue range (the fatigue life higher than 10^5 cycles), it is found that the fatigue strength has pronouncedly decreased from 500 MPa to below 400 MPa after 180 min of the surface treatment. Thus, this surface treatment is not an effective process to improve the fatigue strength

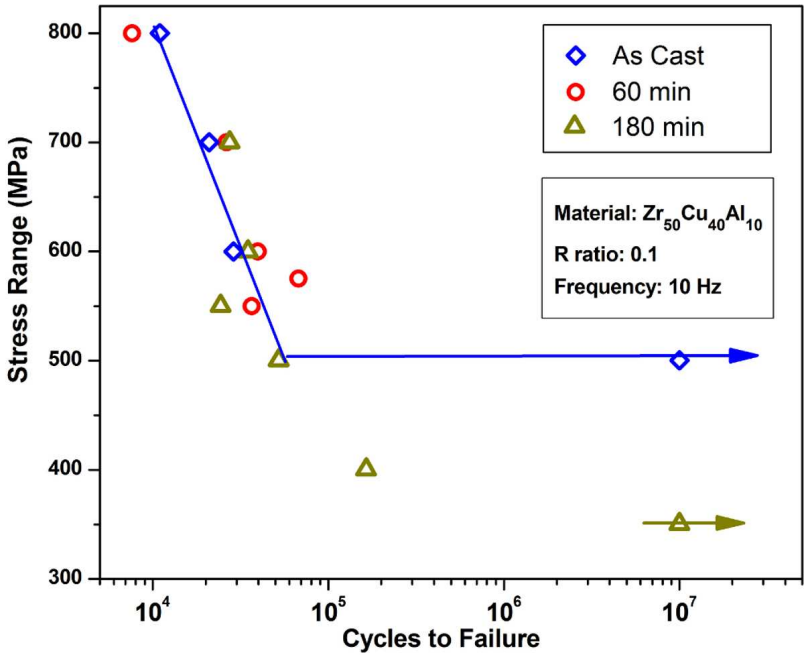

Figure 7.8: S-N curves of the as-cast and S^{2}PD-processed $Zr_{50}Cu_{40}Al_{10}$ BMG obtained through four-point-bending fatigue experiments.

of the BMG material, though it works well on a Ni-based superalloy [88]. In Reference [74], it is noted that the bombardment may cause surface contaminations and damages in the sample-surface layer, which may have a detrimental effect on the fatigue properties. The similar trend was also observed in an LM-001 (commercially known as $Zr_{21.5}Ti_{42}Cu_{15.5}Ni_{14.5}Be_{3.5}Al_3$) BMG. It is found that the shot-peening process does not cause a significant enhancement of the fatigue performance due to the deformation-induced plastic-flow softening [138].

A detailed analysis of the fractography of the fatigue specimens is presented as follows. Since the fatigue life depends on both the crack-initiation and the crack-propagation cycles, it is important to investigate how the S^{2}PD process will affect these two stages before we can fully understand the effects of the severely-plastically-deformed surface layer on the fatigue behavior of the BMGs. Figure 7.9 shows the fractography of the 60-min-processed sample with the fatigue life of 7,633 cycles. It is shown in Fig. 7.9(a) that the crack actually initiated from the corner of the rectangular sample, which is also true for most of the other processed samples. In Fig. 7.9(b), we did find that the surface treatment has an effect on the fatigue propagation: the

elliptically radial fatigue striations were retarded when they propagated close to the processed surface. The near-surface compressive-residual stress and/or the structural change caused by the process might be the reasons for this phenomenon. Some simple measurements shown in Figs. 7.9(c) and (d) indicate that in this sample, there are only approximately 440 striations. Noted that the total fatigue cycles to failure is 7,633. Therefore, the crack propagation only contributed about 5% to the total fatigue lifetime, if we assumed that one striation is formed during one fatigue cycle. In some other studies [6], about 10 finer striations were observed within each striation defined here, and each fine striation was assumed to be corresponding to one fatigue cycle. If this is the case, the crack propagation still contributes around half of the total life.

Based on the above observation, it can be concluded that the surface treatment does has an effect to retard the fatigue-crack propagation, but the damages that it causes may accelerate the crack initiation especially in the high-cycle-fatigue range. On the other hand, the fatigue life of this material mainly depends on the crack-initiation cycle because most of the total cycles are contributed by the crack initiation. Therefore, it is not surprising to find that the fatigue-life time decreases especially in a high-cycle fatigue range after the surface treatment.

7.4 Conclusions

The surface-severe-plastic-deformation behavior of a Zr-based BMG has been investigated in the present work. It is shown that both the microstructures and the mechanical properties have been affected by the treatment process. To be specific:

1. The surface of the BMG has been subjected to the severe-plastic deformation at room temperature without the occurrence of brittle fracture, which shows the good ductility of the material if the propagation of shear bands can be inhibited;

2. During the severe-plastic-deformation process, crystallization is observed in the near-surface layer, and the amount of crystal phases decreases as the position goes from the treated surface to the interior;

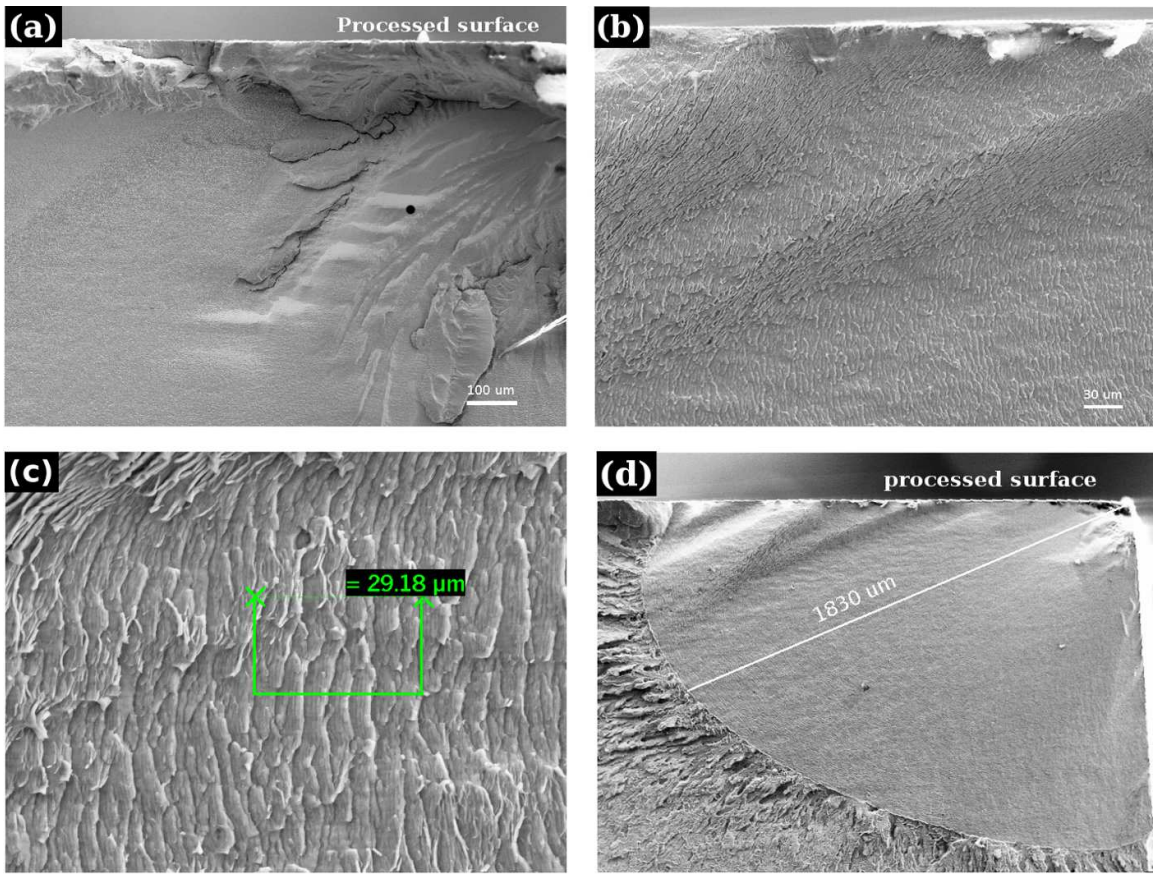

Figure 7.9: Fractography of the fatigue samples shows that the crack initiated from the corner (a), the propagation path was retarded by the processed surface (b), a measurement of the width of each fatigue striation (c), and the total length of the propagation path (d).

3. Work softening was observed in the very impact surface, but the maximal hardness, which is higher than that of the unaffected interior, was observed at about 100 μm from the treated surface;

4. The fatigue strength of this BMG did not benefit from the S^2PD process as it did for a crystal material. The possible surface damages introduced during the bombardment might be the main reason.

CHAPTER 8

Conclusions

In this work, a surface severe-plastic-deformation process (S^2PD) was successfully developed and applied on a Ni-based C-2000 superalloy and a Zr-based bulk metallic glass. It uses the WC/Co hard balls with diammters varying from 1.6 mm to 7.9 mm, a velocity of about 5 m/s to impact the sample surface in a controlled argon atmosphere. Because of the near-surface plastic deformtion produced by the process, it is shown that the S^2PD process has the capability of simultaneously creating (a) a work-hardened surface layer, (b) a nanocrystalline (nc) surface layer, (c) a surface region with compressive residual stresses, and (d) a grain-size gradient with a nc surface and a coarse-grained interior for the polycrystalline superalloy. For the amorphous Zr-based bulk metallic glass, it is shown that the process may also alter the near-surface microstructures, such as introducing nanocrystallization, and, thus, changing the overall mechanical properties of the component. To be specific, the conclusions obtained through this thesis work are:

- The S^2PD process, (or a surface nanocrystallization and hardening (SNH) process as called at the begining of the thesis work), has been successfully developed and utilized on a commercialized Ni-based C-2000 superalloy. With different setups of the easy-to-change parameters, such as impacting time periods, ball number, ball sizes, etc., both the microstructures and the mechanical properties have shown different characteristics. However, the following five changes are basically the same regardless of the processing conditions. They are: (a) the formation of a surface-nanocrystalline layer; (b) surface work hardening; (c) the presence of residual compressive in-plane stresses at the surface layer; (d) the increased surface roughness; and (e) the surface contamination due to the material transfer between balls and the plate.

- It is shown that larger balls in the S^2PD process have higher efficiency in introducing a surface work-hardened region, a surface nanocrystalline layer, and residual compressive stresses at the surface than small balls. However, large balls also introduce a greater amount of surface contamination and result in a rougher surface. The surface hardness of the specimen was increased about 90% and 70% after being treated with 7.9 mm and 4.9 mm balls, respectively. However, the hardness profileon the cross section did not change much with the processing time. The surface-WC contamination was found to be more severe in the large-ball-processed samples than in the small-ball-processed samples.

- A longer SNH-processing time can lead to finer grain sizes at the surface, a thicker work-hardened layer, and larger residual compressive stresses. However, the strengthening saturation is observed when the processing time is longer than a critical value (which is 30 min for 7.9-mm balls). For example, in the studied C-2000 samples with 180-min surface treatment, a nano-structured near surface layer (grain sizes about 10 - 20 nm) with a thickness of around 50 - 100 μm was observed, while that of the 30-min treated sample is less than 5 μm. A longer processing time also results in more surface contamination. With the 180-min treatment, the contamination can reach as deep as 20 microns into the surface.

- Through the comprehensive and exhaustive XRD analysis, it is confirmed that the S^2PD process has resulted in: (i) the formation of nanograins, grain-size gradients, deformation twins, and deformation faults, (ii) the introduction of macroscopic residual stresses, lattice microstrains, and crystallographic texture, and (iii) the alternation in the dislocation density and in-plane lattice parameters of the crystal lattices. The impacted surface with 30-min processing exhibits polycrystalline nano-grains with sizes predominately 10 to 20 nm and containing few dislocations and twins and, thus, very low lattice strains. The sub-surface region right below the impacted surface (about 5 to 10 μm from the impacted surface) has the highest dislocation, twin, and fault densities and the highest internal strain in the entire Ni-alloy sample. The profile of

macroscopic residual stresses induced by S^2PD is qualitatively similar to that generated via shot peening.

- The tensile ductility of the C-2000 alloy was reduced by the S^2PD processing. The overall fracture morphology of tensile specimens has been changed from the cup-and-cone fracture for the annealed sample to the shear fracture for S^2PD-processed samples. The longer the S^2PD processing time, the more reduction in the ductility. However, the remaining ductility after the reduction ($\sim 40\%$) is still more than sufficient for engineering applications. The strain-hardening coefficient, the uniform true strain, and the reduction of area also decreased after the treatment. The reduced uniform true strain is mainly related to the decreased strain-hardening coefficient, which, in turn, is caused by the presence of the nano-grained surface and the work hardened surface region.

- The nano-grained surface and the work-hardened surface regions created via S^2PD also result in higher tensile stresses in the surface region than those at the central region of the specimen. These high surface-tensile stresses, in turn, lead to the formation of the fatal crack at the surface of the S^2PD-processed specimen, thereby changing the cup-and-cone fracture for the annealed sample to the shear fracture for S^2PD-processed samples. It is also shown that the residual compressive stresses created via S^2PD have little influence on the ductility of the specimen. Instead, these compressive stresses only extend the apparent elastic strains of S^2PD-processed samples.

- The high surface roughness of S^2PD-processed samples does not have much influence on the ductility. However, surface roughness may play a role in changing the cup-and-cone fracture for the annealed sample to the shear fracture for S^2PD-processed samples.

- It is shown that the severe-plastic-deformation-based surface-nanocrystallization process could affect the fatigue behaviors of the material in two ways. The nanostructured surface layer, work-hardened region, and residual-compressive stress could enhance the fatigue strength especially in the high-cycle fatigue

range ($> 10^6$ cycles), while the surface contamination and micro-damages caused by the S^2PD process could deteriorate the fatigue strength. Using five WC/Co balls 7.9 mm in diameter, the 30 min treatment results in the best improvement in the fatigue resistance, while prolonged treatments (60, 90, and 180 min) either lead to no improvements or even decreases in the fatigue resistance. In the shorter cycle-fatigue range ($< 10^6$ cycles), the fatigue lifetimes of all the treated samples except the 30-min treated sample are lower than those of the as received one. The longer the processing time, the lower the fatigue lifetimes in the shorter cycle-fatigue range. Thus, to fully utilize the S^2PD process to improve the fatigue behavior of the material with a nanostructrued surface layer, processing conditions need to be optimized, at least in terms of processing-time periods. In this study, the optimized fatigue property was obtained in the sample of a 30-min treatment with five WC/Co balls with diameter of 7.9 mm.

- When the surface contamination is not minimized, such as in the case of 180-min processing with 7.9-mm balls, the fatigue resistance can be decreased rather than increased. This is because the severe-surface contamination can outweigh all of the benefits derived from the formation of nano-grains, work hardening, and residual-compressive stresses.

- The surface of the BMG has been subjected to the severe-plastic deformation at room temperature without the occurrence of a brittle fracture, which shows the good ductility of the material if the propagation of shear bands can be inhibited. During the severe-plastic-deformation process, crystallization is observed through the high-sentivity synchrotron diffraction in the near-surface layer, and the amount of crystal phases decreases as the position goes from the treated surface to the interior. Work softening was observed in the very impact surface, but the maximal hardness, which is higher than that of the unaffected interior, was observed at about 100 μm from the treated surface.

- The fatigue strength of this BMG did not benefit from the S^2PD process as it did for a crystal material component. The fatigue fractography showed that the surface damages or contaminations may accelerate the crack initiation, though the

near-surface compressive-residual stress could actually retard the crack propagation. Since the propagation cycles does not predominate in the entire fatigue life, the overall effect of the treatment on the fatigue-property improvement is not significant.

Future Work

The surface-treatment processes on BMGs have attracted attentions only in recent years. Therefore, some interesting issues are still under active investigations. For example, what is the temperature of the shear band during plastic deformation? What is the mechanism for the plastic-deformation-induced crystallization? Is it possible to improve the mechanical properties of the BMGs through the surface treatments? Based upon the work done in this thesis, the following future work are proposed:

- For the C-2000 alloy, the effects of nanograin, work hardening, and residual stress on the mechanical properties may be separated by annealing the processed sample at an appropriate temperature range. For example, selecting a temperature where the nano-grain will not grow, but the residual stress can be eliminated. Hence, the effects of residual stress can be identified.

- For the BMG, further parameter-optimizing work can be done so that the damages and contaminations induced on the sample surface can be minimized, and, therefore, the fatigue properties can be improved. The effects of the impact energy, in terms of the ball sizes and bombardment durations, should be systematically studied.

- The BMG-treatment process can be conducted in a more controllable environment, especially with a controlled temperature. Since the crystallization process is very sensitive to the temperature, conducting the treatment process at a low temperature may inhibit the thermal-induced crystallization. Thus, the deformation-induced crystallization effects could be separated.

- Fatigue behavior of the BMG specimens under different processing times and load conditions can be further investigated in terms of fatigue initiation and

propagation. The results obtained in this work show that the fatigue propagation was retarded by the treatment, but it does not account for a large portion in the total fatigue life. Further studies are needed to confirm this result.

REFERENCES

References

[1] Ralph I. Stephens, Ali Fatemi, Robert R. Stephens, and Henry O. Fuchs, *Metal Fatigue in Engineering*. John Wiley & Sons, Inc., 2001.

[2] W. Schutz, "A history of fatigue", *Engineering Fracture Mechanics*, vol. 54, pp. 263–300, 1996.

[3] See: http://en.wikipedia.org/wiki/Fatigue_(material).

[4] V.V. Bolotin, *Mechanics of Fatigue*. CRC Press, 1999.

[5] P.K. Liaw, C.Y. Yang, S.S. Palusamy, and W. Ren, "Fatigue crack initiation and propagation behavior of pressure vessel steels", *Engineering Fracture Mechanics*, vol. 57, pp. 85–104, 1997.

[6] G.Y. Wang, P.K. Liaw, W.H. Peter, B. Yang, Y. Yokoyama, M.L. Benson, B.A. Green, M.J. Kirkham, S.A. White, T.A. Saleh, R.L. McDaniels, R.V. Steward, R.A. Buchanan, C.T. Liu, and C.R. Brooks, "Fatigue behavior of bulk metallic glasses", *Intermetallics*, vol. 12, pp. 885–892, 2004.

[7] T. Nicholas, *High Cycle Fatigue*. Elsevier, 2006.

[8] M.A. Meyers, A. Mishra, and D.J. Benson, "Mechanical properties of nanocrystalline materials", *Progress in Materials Science*, vol. 51, pp. 527–556, 2006.

[9] A.Y. Vinogradov, V.V. Stolyarov, S. Hashimoto, and R.Z. Valiev, "Cyclic behavior of ultrafine-grain titanium produced by severe plastic deformation", *Materials Science and Engineering A*, vol. 318, pp. 163–173, 2001.

[10] C.S. Chung, J.K. Kim, H.K. Kim, and W.J. Kim, "Improvement of high-cycle fatigue life in a 6061 Al alloy produced by equal channel angular pressing", *Materials Science and Engineering A*, vol. 337, pp. 39–44, 2002.

[11] K.S. Chan, "A microstructure-based fatigue-crack-initiation model", *Metallurgical and Materials Transactions A*, vol. 34, pp. 43–58, 2003.

[12] Y. Ochi, K. Masaki, T. Matsumura, and T. Sekino, "Effect of shot-peening treatment on high-cycle fatigue properties of ductile cast iron", *International Journal of Fatigue*, vol. 23, pp. 441–448, 2001.

[13] M. Telford, "The case for bulk metallic glass", *Materialstoday*, vol. 7, pp. 36–43, 2004.

[14] A. Inoue, "High strength bulk amorphous alloys with low critical cooling rates", *Materials Transactions JIM*, vol. 36, pp. 866–875, 1995.

[15] W.H. Jiang, G.J. Fan, H. Choo, and P.K. Liaw, "Ductility of a Zr-based bulk-metallic glass with different specimen's geometries", *Materials Letters*, vol. 60, pp. 3537–3540, 2006.

[16] H. Bei, S. Xie, and E.P. George, "Softening caused by profuse shear banding in a bulk metallic glass", *Applied Physics Letters*, vol. 96, p. 105503, 2006.

[17] C.C. Hays, C.P. Kim, and W.L. Johnson, "Microstructure controlled shear band pattern formation and enhanced plasticity of bulk metallic glasses containing in situ formed ductile phase dendrite dispersions", *Physical Review Letters*, vol. 84, pp. 2901–2904, 2000.

[18] Y. Zeng, D.V. Louzguine-Luzgin, N. Nishiyama, and A. Inoue, "Role of nanocrystals in ductile Ni-Pd-P metallic glass", *Journal of Alloys and Compounds*, vol. 441, pp. 131–134, 2007.

[19] H.O. Fuchs, *Mechanical Engineers' Handbook*. Metal Improvement Company, 1986.

[20] S. Ya. Yarema, "Formation of the science of fatigue of metals 1840-1940", *Materials Science*, vol. 43, pp. 869–885, 2007.

[21] C.A. Rodopoulos, S.A. Curtis, E.R. de los Rios, and J. SolisRomero, "Optimisation of the fatigue resistance of 2024-T351 aluminium alloys by controlled shot peeningmethodology, results and analysis", *International Journal of Fatigue*, vol. 26, pp. 849–856, 2004.

[22] E.R. de los Rios, M. Trull, and A. Levers, "Modelling fatigue crack growth in shot peened components of 2024-T351", *Fatigue & Fracture of Engineering Materials & Structures*, vol. 23, pp. 709–716, 2000.

[23] W. Cheng and I. Finnie, *Residual Stress Measurement and the Slitting Method*. Springer, 2007.

[24] P.J. Withers and H.K.D.H. Bhadeshia, "Residual stress: Part 1 - Measurement techniques", *Materials Science and Technology*, vol. 17, pp. 355–364, 2001.

[25] H.O. Fuchs, "Shot peening stress profiles", tech. rep., Metal Improvement Company, 1986.

[26] H.J. Grover, "Factors by which shot peening influences the fatigue strength of parts", *The shot peener*, vol. 12, pp. 5–9, 1998.

[27] M. Kobayashi, T. Matsui, and Y. Murakami, "Mechanism of creation of compressive residual stress by shot peening", *International Journal of Fatigue*, vol. 20, pp. 351–357, 1998.

[28] G.A. Webster and A.N. Ezeilo, "Residual stress distributions and their influence on fatigue lifetimes", *International Journal of Fatigue*, vol. 23, pp. 357–383, 2001.

[29] M. Meo and R. Vignjevic, "Finite element analysis of residual stress induced by shot peening process", *Advances in Engineering Software*, vol. 34, pp. 569–575, 2003.

[30] T. Hong, J.Y. Ooi, and B. Shaw, "A numerical simulation to relate the shot peening parameters to the induced residual stresses", *Engineering Failure Analysis*, vol. 15, pp. 1097–1110, 2008.

[31] T.W. Clyne and S.C. Gill, "Residual stresses in thermal spray coatings and their effect on interfacial adhesion: A review of recent work", *Journal of Thermal Spray Technology*, vol. 4, pp. 401–418, 1996.

[32] K. Sasaki, M. Kishida, and T. Itoh, "The accuracy of residual stress measurement by the hole-drilling method", *Experimental Mechanics*, vol. 37, pp. 250–257, 1997.

[33] V.K. Sinha and V.S. Godaba, "Residual stress measurement in worked and heat treated steel by X-ray diffractometry", *Materials Science and Engineering A*, vol. 488, pp. 491–495, 2008.

[34] R.A. Owen, R.V. Preston, P.J. Withers, H.R. Shercliff, and P.J. Webster, "Neutron and synchrotron measurements of residual strain in TIG welded aluminium alloy 2024", *Materials Science and Engineering A*, vol. 346, pp. 159–167, 2003.

[35] Y.N. Sun, H. Choo, P.K. Liaw, Y.L. Lu, B. Yang, D.W. Brown, and M.A.M. Bourke, "Neutron diffraction studies on lattice strain evolution around a crack-tip during tensile loading and unloading cycles", *Scripta Materialia*, vol. 53, pp. 971–975, 2005.

[36] B.E. Warren, *X-ray Diffraction*. Dover, 1990.

[37] M.R. Daymond, M.A.M. Bourke, R.B. Von Dreele, B. Clausen, and T. Lorentzen, "Use of Rietveld refinement for elastic macrostrain determination and for evaluation of plastic strain history from diffraction spectra", *Journal of Applied Physics*, vol. 82, pp. 1554–1562, 1997.

[38] A.N. Ezeilo, G.A. Webster, P.J. Withers, and X. Wang, "Characterisation of elastic and plastic deformation in a nickel superalloy using pulsed neutrons", *Physica B*, vol. 180-181, pp. 1044–1046, 1992.

[39] C.N.J. Wagner, "Stacking faults by low-temperature cold work in copper and alpha brass", *Acta Metallurgica*, vol. 5, pp. 427–434, 1957.

[40] C.N.J. Wagner, "X-ray study of low-temperature cold work in silver and aluminum", *Acta Metallurgica*, vol. 5, pp. 477–482, 1957.

[41] R.L. Snyder, J. Fiala, and H.J. Bunge, eds., *Defect and Microstructure Analysis by Diffraction*. Oxford University Press, 1999.

[42] J.I. Langford, *Diffraction Analysis of the Microstructure of Materials*. Springer, 2004.

[43] B.D. Cullity, *Elements of X-ray Diffraction*. Addison-Wesley, 1978.

[44] U. Welzel, J. Ligot, P. Lamparter, A. C. Vermeulen, and E. J. Mittemeijer, "Stress analysis of polycrystalline thin films and surface regions by X-ray diffraction", *Journal of Applied Crystallography*, vol. 38, pp. 1–29, 2005.

[45] J. Straub, "Shot peening - theory", tech. rep., AMGA meeting, 1962.

[46] M.A. Moshier and B.M. Hillberry, "The inclusion of compressive residual stress effects in crack growth modelling", *Fatigue & Fracture of Engineering Materials & Structures*, vol. 22, pp. 519–526, 1999.

[47] J. Shigley, C. Mischke, and R. Budynas, *Mechanical Engineering Design*. McGraw-Hill, 2003.

[48] *SAE fatigue design handbook, 3rd ed., 1997*.

[49] Y. Mutoh, G.H. Fair, B. Nobel, and R.B. Waterhouse, "The effect of residual stresses induced by shot-peening on fatigue crack propagation in two high strength aluminium alloys", *Fatigue & Fracture of Engineering Materials & Structures*, vol. 10, pp. 261–272, 1987.

[50] J.C. Newman, "Fatigue-life prediction methodology using a crak-closure model", *Journal of Engineering Materials and Technology*, vol. 117, pp. 433–439, 1995.

[51] B. Kumar, "Effects of residual stresses on crack growth in aluminum alloys", in *Residual Stress and Its Effects on Fatigue and Fracture*, 2006.

[52] S.B. Mahagaonkar, P.K. Brahmankar, and C.Y. Seemikeri, "Effect of shot peening parameters on microhardness of AISI 1045 and 316L material: an analysis using design of experiment", *International Journal of Advanced Manufacturing Technology*, vol. 38, pp. 563–574, 2008.

[53] R. Fathallah, A. Laamouri, H. Sidhom, and C. Braham, "High cycle fatigue behavior prediction of shot-peened parts", *International Journal of Fatigue*, vol. 26, pp. 1053–1067, 2004.

[54] I.F. Pariente and M Guagliano, "About the role of residual stresses and surface work hardening on fatigue ΔK_{th} of a nitrided and shot peened low-alloy steel", *Surface and Coating Technology*, vol. 202, pp. 3072–3080, 2008.

[55] E.R. de los Rios, P. Mercier, and B.M. El-Sehily, "Short crack growth behavior under variable amplitude loading of shot peened surfaces", *Fatigue & Fracture of Engineering Materials & Structures*, vol. 19, pp. 175–184, 1996.

[56] S. Curtis, E.R. de los Rios, C.A. Rodopoulos, and A. Levers, "Analysis of the effects of controlled shot peening on fatigue damage of high strength aluminium alloys", *International Journal of Fatigue*, vol. 25, pp. 59–66, 2003.

[57] A. Turnball, E.R. de los Rios, R.B. Tait, C. Laurant, and J.S. Boabaid, "Improving the fatigue crack resistance of Waspaloy by shot peening", *Fatigue & Fracture of Engineering Materials & Structures*, vol. 21, pp. 1513–1524, 1998.

[58] H. Gleiter, "Nanocrystalline materials", *Progress in Materials Science*, vol. 33, pp. 323–315, 1989.

[59] K. Lu, "Nanocrystalline metals crystallized from amorphous solids: nanocrystalline, strucure and properties", *Materials Science and Engineering R*, vol. 16, pp. 161–221, 1996.

[60] H. Gleiter, "Nanostructured materials:basic concepts and microstructure", *Acta Materialia*, vol. 48, pp. 1–29, 2000.

[61] R.Z. Valiev, R.K. Islamgaliev, and I.V. Alexandrov, "Bulk nanostructured materials from severe plastic deformation", *Progress in Materials Science*, vol. 45, pp. 103–189, 2000.

[62] K.S. Kumar, H. Van Swygenhoven, and S. Suresh, "Mechanical behavior of nanocrystalline metals and alloys", *Acta Materialia*, vol. 51, pp. 5743–5774, 2003.

[63] D. Wolf, V. Yamakov, S.R. Phillpot, A. Mukherjee, and H. Gleiter, "Deformation of nanocrystalline materials by molecular-dynamics simulation: relationship to experiments?", *Acta Materialia*, vol. 53, pp. 1–40, 2005.

[64] G.J. Fan, H. Choo, P.K. Liaw, and E.J. Lavernia, "A model for the inverse Hall-Petch relation of nanocrystalline materials", *Materials Science and Engineering A*, vol. 409, pp. 243–248, 2005.

[65] G.J. Fan, G.Y. Wang, H. Choo, P.K. Liaw, Y.S. Park, B.Q. Han, and E.J. Lavernia, "Deformation behavior of an ultrafine-grained Al-Mg alloy at different strain rates", *Scripta Materialia*, vol. 52, pp. 929–933, 2005.

[66] G.J. Fan, L.F. Fu, D.C. Qiao, H. Choo, P.K. Liaw, and N.D. Browning, "Grain growth in a bulk nanocrystalline Co alloy during tensile plastic deformation", *Scripta Materialia*, vol. 54, pp. 2137–2141, 2006.

[67] R.Z. Valiev and T.G. Langdon, "Principles of equal-channel angular pressing as a processing tool for grain refinement", *Progress in Materials Science*, vol. 51, pp. 881–981, 2006.

[68] Y. Iwahashi, Z. Horita, M. Nemoto, and T.G. Langdon, "The process of grain refinement in equal-channel angular pressing", *Acta Materialia*, vol. 46, pp. 3317–3331, 1998.

[69] A.P. Zhilyaev and T.G. Langdon, "Using high-pressure torsion for metal processing:fundamentals and applications", *Progress in Materials Science*, vol. 53, pp. 893–979, 2008.

[70] J.R. Weertman, "Hall-Petch strengthening in nanocrystalline metals", *Materials Science and Engineering A*, vol. 166, pp. 161–167, 1993.

[71] R.Z. Valiev, "Structure and mechanical properties of ultrafine-grained metals", *Materials Science and Engineering A*, vol. 234-236, pp. 59–66, 1997.

[72] G. Palumbo, S.J. thorpe, and K.T. Aust, "On the contribution of triple junctions to the structure and properties of nanocrystalline materials", *Scripta Metallurgica et Materialia*, vol. 24, pp. 1347–1350, 1990.

[73] G.J. Fan, L.F. Fu, G.Y. Wang, H. Choo, P.K. Liaw, and N.D. Browning, "Mechanical behavior of a bulk nanocrystalline Ni-Fe alloy", *Journal of Alloys and Compounds*, vol. 434-435, pp. 298–300, 2007.

[74] J.W. Tian, J.C. Villegas, W. Yuan, D. Fielden, L. Shaw, P.K. Liaw, and D.L. Klarstrom, "A study of the effect of nanostructured surface layers on the fatigue behaviors of a C-2000 superalloy", *Materials Science and Engineering A*, vol. 468-470, pp. 164–170, 2007.

[75] J.W. Tian, K. Dai, J.C. Villegas, L. Shaw, P.K. Liaw, D.L. Klarstrom, and A.L. Ortiz, "Tensile properties of a nickel-base alloy subjected to surface severe plastic deformation", *Materials Science and Engineering A*, vol. 493, pp. 176–183, 2008. Materials Science and Engineering A, 2008, available online at doi:10.1016/j.msea.2007.07.102.

[76] A.L. Ortiz, J.W. Tian, J.C. Villegas, L.L. Shaw, and P.K. Liaw, "Interrogation of the microstructure and residual stress of a nickel-base alloy subjected to surface severe plastic deformation", *Acta Materialia*, vol. 56, pp. 413–426, 2008.

[77] T. Hanlon, Y.-N. Kwon, and S. Suresh, "Grain size effects on the fatigue response of nanocrystalline metals", *Scripta Materialia*, vol. 49, pp. 675–680, 2003.

[78] H.W. Zhang, Z.K. Hei, G. Liu, J. Lu, and K. Lu, "Formation of nanostructured surface layer on AISI 304 stainless steel by means of surface mechanical attrition treatment", *Acta Materialia*, vol. 51, pp. 1871–1881, 2003.

[79] N.R. Tao, X.L. Wu, M.L. Sui, J. Lu, and K. Lu, "Grain refinement at the nanoscale via mechanical twinning and dislocation interaction in a nickel-based alloy", *Journal of Materials Research*, vol. 19, pp. 1623–1629, 2004.

[80] K. Lu and J. Lu, "Nanostructured surface layer on metallic materials induced by surface mechanical attrition treatment", *Materials Science and Engineering A*, vol. 375-377, pp. 38–45, 2004.

[81] T. Roland, D. Retraint, K. Lu, and J. Lu, "Fatigue life improvement through surface nanostructuring of stainless steel by means of surface mechanical attrition treatment", *Scripta Materialia*, vol. 54, pp. 1949–1954, 2006.

[82] N.R. Tao, M.L. Sui, J. Lu, and K. Lu, "Surface nanocrystallization of iron induced by ultrasonic shot peening", *Nanostructured Materials*, vol. 11, pp. 433–440, 1999.

[83] X. Wu, N. Tao, Y. Hong, B. Xu, J. Lu, and K. Lu, "Microstructure and evolution of mechanically induced ultrafine grain in surface layer of Al-Alloy subjected to USSP", *Acta Materialia*, vol. 50, pp. 2075–2084, 2002.

[84] G. Liu, J. Lu, and K. Lu, "Surface nanocrystallization of 316L stainless steel induced by ultrasonic shot peening", *Materials Science and Engineering A*, vol. 286, pp. 91–95, 2000.

[85] G. Liu, S.C. Wang, X.F. Lou, J. Lu, and K. Lu, "Low carbon steel with nanostructured surface layer induced by high-energy shot peening", *Scripta Materialia*, vol. 44, pp. 1791–1795, 2001.

[86] J.L. Liu, M. Umemoto, Y. Todaka, and K. Tsuchiya, "Formation of a nanocrystalline surface layer on steels by air blast shot peening", *Journal of Materials Science*, vol. 42, pp. 7716–7720, 2007.

[87] J. Villegas, K. Dai, and L. Shaw, "Experiments and modeling of the surface nanocrystallization and hardening (SNH) process", in *Processing and Fabrication of Advanced Materials: XII* (T. Srivatsan and R. Varin, eds.), (Materials Park, OH), pp. 358–372, ASM International, 2003.

[88] J.C. Villegas, L.L. Shaw, K. Dai, W. Yuan, J. Tian, P.K. Liaw, and D.L. Klarstrom, "Enhanced fatigue resistance of a nickel-based hastelloy induced by a surface nanocrystallization and hardening process", *Philosophical Magazine Letters*, vol. 85, pp. 427–437, 2005.

[89] K. Dai and L. Shaw, "Comparison between shot peening and surface nanocrystallization and hardening processes", *Materials Science and Engineering A*, vol. 463, pp. 46–53, 2007.

[90] Z.B. Wang, N.R. Tao, S. Li, W. Wang, G. Liu, J. Lu, and K. Lu, "Effect of surface nanocrystallization on friction and wear properties in low carbon steel", *Materials Science and Engineering A*, vol. 352, pp. 144–149, 2003.

[91] M. Umemoto, K. todaka, and K. Tsuchiya, "Formation of nanocrystalline structure in carbon steels by ball drop and particle impact technicues", *Materials Science and Engineering A*, vol. 375-377, pp. 899–904, 2004.

[92] H.P. Klug and L.E. Alexander, eds., *X-ray Diffraction Procedures for Polycrystalline and Amorphous Materials*. Wiley, 1974.

[93] T. Ungar, "Microstructural parameters from X-ray diffraction peak broadening", *Scripta Materialia*, vol. 51, pp. 777–781, 2004.

[94] H.P. Klug and L.E. Alexander, *X-Ray Diffraction Procedures for Polycrystalline and Amorphous Materials*. John Wiley & Sons, 1954.

[95] A.R. Stokes and A.J.C. Wilson, "The diffraction of X-rays by distorted crystal aggregates -I", in *Proceedings of Physics Society*, 1944.

[96] L. Shaw, J. Villegas, H. Luo, and M. Miracle, "Thermal stability of nanostructured $Al_93Fe_3Ti_2Cr_2$ alloys prepared via mechanical alloying", *Acta Materialia*, vol. 51, pp. 2647–2663, 2003.

[97] A.L. Ortiz and L. Shaw, "X-ray diffraction analysis of a severely plastically deformed aluminum alloy", *Acta Materialia*, vol. 52, pp. 2185–2197, 2004.

[98] F. Sanchez-Bajo, A.L.Ortiz, and F.L. Cumbrera, "Analytical formulation of the variance method of line-broadening analysis for Voigtian X-ray diffraction peaks", *Journal of Applied Crystallography*, vol. 39, pp. 598–600, 2006.

[99] J.I. Langford and A.J.C. Wilson, "Scherrer after sixty years: A survey and some new results in the determination of crystallite size", *Journal of Applied Crystallography*, vol. 11, pp. 102–113, 1978.

[100] T. Ungar, "Characterization of nanocrystalline materials by X-ray line profile analysis", *Journal of Materials Science*, vol. 42, pp. 1584–1593, 2007.

[101] T. Roland, D. Retraint, K. Lu, and J. Lu, "Enhanced mechanical behavior of a nanocrystallized stainless steel and its thermal stability", *Materials Science and Engineering A*, vol. 445-446, pp. 281–288, 2007.

[102] L. Balogh, T. Ungar, Y. Zhao, Y.T. Zhu, Z. Horita, C. Xu, and T.G. Langdon, "Influence of stacking-fault energy on microstructural characteristics of ultrafine-grain copper and copper-zinc alloys", *Acta Materialia*, vol. 56, pp. 809–820, 2008.

[103] W. Klement, R.H. Willens, and P. Duwez, "Non-crystalline structure in solidified gold-silicon alloys", *Nature*, vol. 187, p. 869, 1960.

[104] W.H. Wang, C. Dong, and C.H. Shek, "Bulk metallic glasses", *Materials Science and Engineering R*, vol. 44, pp. 45–89, 2004.

[105] H.S. Chen, "Thermodynamic considerations of the formation and stability of metallic glasses", *Acta Metallurgica*, vol. 22, pp. 1505–1511, 1974.

[106] A.L. Greer, "Through a glass, lightly", *Nature*, vol. 402, pp. 132–133, 1999.

[107] D.B. Miracle, "A structural model for metallic glasses", *Nature Materials*, vol. 3, pp. 679–702, 2004.

[108] H.W. Sheng, W.K. Luo, F.M. Alamgir, J.M. Bai, and E. Ma, "Atomic packing and short-to-medium-range order in metallic glasses", *Nature*, vol. 439, pp. 419–425, 2006.

[109] D.C. Hofmann, J.-Y. Suh, A. Wiest, G. Duan, M.-L. Lind, M.D. Demetriou, and W.L. Johnson, "Designing metallic glass matrix composites with high toughness and tensile ductility", *Nature*, vol. 451, pp. 1085–1090, 2008.

[110] J. Das, M.B. Tang, K.B. Kim, R. Theissmann, F. Baier, W.H. Wang, and J. Eckert, "Work-hardenable ductile bulk metallic glass", *Physical Review Letters*, vol. 94, p. 205502, 2005.

[111] Michael Miller and Peter K. Liaw, *Bulk Metallic Glasses*. Springer, 2008.

[112] J.F. Loffler, "Bulk metallic glasses", *Intermetallics*, vol. 11, pp. 529–540, 2003.

[113] A. Inoue, N. Nishiyama, and H. Kimura, "Preparation and thermal stability of bulk amorphous $Pd_40Cu_30Ni_10P_20$ alloy cylinder of 72 mm in diameter", *Materials Transactions JIM*, vol. 38, pp. 179–183, 1997.

[114] T. Egami, "Formation and deformation of metallic glasses: Atomistic theory", *Intermetallics*, vol. 14, pp. 882–887, 2006.

[115] J.R. Morris, M. Xu, Y.Y. Ye, D.J. Sordelet, and M.J. Kramer, "Theoretical and experimental studies of devitrification pathways in the $Zr_2Cu_1 - xPd_x$ metallic glass system", *Acta Materialia*, vol. 55, pp. 5901–5909, 2007.

[116] C.A. Schuh and T.G. Nieh, "A nanoindentation study of serrated flow in bulk metallic glasses", *Acta Materialia*, vol. 51, pp. 87–99, 2003.

[117] R.D. Conner, Y. Li, W.D. Nix, and W.L. Johnson, "Shear band spacing under bending of Zr-based metallic glass plates", *Acta Materialia*, vol. 52, pp. 2429–2434, 2004.

[118] J.-J. Kim, Y. Choi, S. Suresh, and A.S. Argon, "Nanoindentation of a bulk amorphous metal alloy at room temperature", *Science*, vol. 295, pp. 654–657, 2002.

[119] C.A. Schuh, A.C. Lund, and T.G. Nieh, "New regime of homogeneous flow in the deformation map of metallic glasses: elevated temperature nanoindentation experiments and mechanistic modeling", *Acta Materialia*, vol. 52, pp. 5879–5891, 2004.

[120] W.H. Jiang, G.J. Fan, F.X. Liu, G.Y. Wang, H. Choo, and P.K. Liaw, "Spatiotemporally inhomogeneous plastic flow of a bulk-metallic glass", *International Journal of Plasticity*, vol. 24, pp. 1–16, 2008.

[121] F. Yang, K. Geng, P.K. Liaw, G.J. Fan, and H. Choo, "Deformation in a $Zr_{57}Ti_5Cu_{20}Ni_8Al_{10}$ bulk metallic glass during nanoindentation", *Acta Materialia*, vol. 55, pp. 321–327, 2007.

[122] H. Chen, Y. He, G.J. Shiflet, and S.J. Poon, "Deformation-induced nanocrystal formation in shear bands of amorphous alloy", *Nature*, vol. 367, pp. 541–543, 1994.

[123] W.H. jiang, F.E. Pinkerton, and M. Atzmon, "Deformation-induced nanocrystallization in an Al-based amorphous alloy at a subambient temperature", *Scripta Materialia*, vol. 48, pp. 1195–1200, 2003.

[124] M. Chen, A. Inoue, W. Zhang, and T. Sakurai, "Extraordinary plasticity of ductile bulk metallic glasses", *Physical Review Letters*, vol. 96, p. 245502, 2006.

[125] J.J. Lewandowski and A.L. Greer, "Temperature rise at shear bands in metallic glasses", *Nature Materials*, vol. 5, pp. 15–18, 2006.

[126] C.T. Liu, L. heatherly, D.S. Easton, C.A. Carmichael, J.H. Schneibel, C.H. Chen, J.L. Wright, M.H. Yoo, and J.A. Horton andA. Inoue, "Test environments and mechanical properties of Zr-base bulk amorphous alloys", *Metallurgical and Materials Transactions A*, vol. 29, pp. 1811–1820, 1998.

[127] C.J. Gilbert, J.W. Ager III, V. Schroeder, R.O. Ritchie, J.P. Lioyd, and J.R. Graham, "Light emission during fracture of a ZrTiNiCuBe bulk metallic glass", *Applied Physics Letters*, vol. 74, pp. 3809–3811, 1999.

[128] W.J. Wright, R.B. Schwarz, and W.D. Nix, "Localized heating druing serrated plastic flow in bulk metallic glasses", *Materials Science and Engineering A*, vol. 319-321, pp. 229–232, 2001.

[129] B. Yang, M.L. Morrison, P.K. Liaw, R.A. Buchanan, G.Y. Wang, C.T. Liu, and M. Denda, "Dynamic evolution of nanoscale shear bands in a bulk-metallic glass", *Applied Physics Letters*, vol. 86, p. 141904, 2005.

[130] Z.J. Yan, J.F. Li, R.H. Zhou, and Y.Q. Wu, "Indentation-induced crystallization in a metallic glass", *Acta Physica Sinica*, vol. 56, pp. 999–1003, 2007. (In Chinese).

[131] K. Wang, T. Fujita, Y.Q. Zeng, N. Nishiyama, A. Inoue, and M.W. Chen, "Micromechanisms of serrated flow in a $Ni_50Pd_30P_{20}$ bulk metallic glass with a large compression plasticity", *Acta Materialia*, vol. 56, pp. 2834–2842, 2008.

[132] F.Z. Li, Z.-J. Liu, Q. Jin, Z.-M. Yu, and E. Liu, "Investigation on work softening behavior of Aluminum and its alloys with iron", *Journal of Materials Engineering and Performance*, vol. 6, pp. 172–176, 1997.

[133] B. Yang, L. Riester, and T.G. Nieh, "Strain hardening and recovery in a bulk metallic glass under nanoindentation", *Scripta Materialia*, vol. 54, pp. 1277–1280, 2006.

[134] Y. Zhang, W.H. Wang, and A.L. Greer, "Making metallic glasses plastic by control of residual stress", *Nature Materials*, vol. 5, pp. 857–860, 2006.

[135] L.H. Dai and Y.L. Bai, "Basic mechanical behaviors and mechanics of shear banding in BMGs", *International Journal of Impact Engineering*, vol. 35, pp. 704–716, 2008.

[136] L.Y. Chen, Q. Ge, S. Qu, and J.Z. Jiang, "Stress-induced softening and hardening in a bulk metallic glass", *Acta Materialia*, vol. 59, pp. 1210–1213, 2008.

[137] R. Bhowmick, R. Raghavan, K. Chattopadhyay, and U. Ramamurty, "Plastic flow softening in a bulk metallic glass", *Acta Materialia*, vol. 54, pp. 4221–4228, 2006.

[138] R. Raghavan, R. Ayer, H.W. Jin, C.N. Marzinsky, and U. Ramamurty, "Effect of shot peening on the fatigue life of a Zr-based bulk metallic glass", *Scripta Materialia*, vol. 59, pp. 167–170, 2008.

[139] T. Yamamoto, T. Takahashi, H. Kimura, and A. Inoue, "Effect of ball-milling and shot-peening on $Zr_{55}Al_{10}Ni_5Cu_{30}$ alloys", *Journal of Alloys and Compounds*, vol. 430, pp. 97–101, 2007.

[140] F.O. Mear, B. Lenk, Y. Zhang, and A.L. Greer, "Structural relaxation in a heavily cold-worked metallic glass", `doi:10.1016/j.scriptamat.2008.08.023`, 2008.

[141] Y. Yokoyama, H. Inoue, K. Fukaura, and A. Inoue, "Relationship between the liquidus surface and structures of Zr-Cu-Al bulk amorphous alloys", *Materials Transactions, JIM*, vol. 43, pp. 575–579, 2002.

[142] ASTM C 1211-98a, "Standard Test Method for Flexural Strength of Advanced Ceramics at Elevated Temperatures", ASTM Standards, 1998.

[143] W. Yuan, "The Effects of the Surface-Nanocrystallization and Hardening (SNH) Process on the Fatigue Resistance", Master's thesis, University of Tennessee, 2004.

[144] R.W. Cahn, "Materials science - nanastructured materials", *Nature*, vol. 348, pp. 389–390, 1990.

[145] J.S.C. Tang and C.C. Koch, "The Hall-Petch relationship in nanocrystalline Iron produced by ball milling", *Scripta Metallurgica et Materiallia*, vol. 24, pp. 1599–1604, 1990.

[146] H.O. Fuchs and R.I. Stephens, *Metal Fatigue in Engineering*. John Wiley, New York, 1980.

[147] N.R. Tao, Z.B. Wang, W.P. Tong, M.L. Sui, J. Lu, and K. Lu, "An investigation of surface nanocrystallization mechanism in Fe induced by surface mechanical attrition treatment", *Acta Materialia*, vol. 50, pp. 4603–4616, 2002.

[148] K.Y. Zhu, A. Vassel, F. Brisset, K. Lu, and J. Lu, "Nanostructure formation mechanism of α-Titanium using SMAT", *Acta Materialia*, vol. 52, pp. 4101–4110, 2004.

[149] J. Villegas, K. Dai, L. Shaw, and P.K. Liaw, "Surface roughness evolution in the surface nanocrystallization and hardening (SNH) process", in *Processing and Properties of Structural Nanomaterials* (L. Shaw, C. Suryanarayana, and R. Mishra, eds.), (Warrendale, PA), pp. 61–68, TMS, 2003.

[150] K. Dai, J. Villegas, Z. Stone, and L. Shaw, "Finite element modeling of the surface roughness of 5052 Al alloy subjected to a surface severe plastic deformation process", *Acta Materialia*, vol. 52, pp. 5771–5782, 2004.

[151] K. Dai, J. Villegas, and L. Shaw, "An analytical model of the surface roughness of an aluminum alloy treated with a surface nanocrystallization and hardening process", *Scripta Materialia*, vol. 52, pp. 259–263, 2004.

[152] G.T. Smith, *Industrial Metrology: Surfaces and roundness*. Springer, 2002.

[153] J.C. Villegas, *Investigation of the Effects of the Surface Nanocrystallization and Hardening (SNH) Process on Bulk Metallic Components*. PhD thesis, University of Connecticut, 2005.

[154] M. Sato, N. Tsuji, Y. Minamino, and Y. Koizumi, "Formation of nanocrystalline surface layers in various metallic materials by near surface severe plastic deformation", *Science and Technology of Advanced Materials*, vol. 5, pp. 145–152, 2004.

[155] K. Dai and L. Shaw, "Parametric studies of multi-material laser densification", *Materials Science and Engineering A*, vol. 430, pp. 221–229, 2006.

[156] A. Vinogradov, S. Nagasaki, V. Patlan, K. Kitagawa, and M. Kawazoe11 (1999) 925934., "Fatigue properties of 5056 Al-Mg alloy produced by equal-channel angular pressing", *Nanostructured Materials*, vol. 11, pp. 925–934, 1999.

[157] K. Lu and J. Lu, "Surface nanocrystallization (SNC) of metallic materials-presentation of the concept behind a new approach", *Journal of Materials Science and Technology*, vol. 15, pp. 193–197, 1999.

[158] L. Shaw and Y.T. Zhu, *CRC Materials Processing Handbook*. CRC Press, 2007.

[159] J.C. Villegas, K. Dai, L.L. Shaw, and P.K. Liaw, "Nanocrystallization of a nickel alloy subjected to surface severe plastic deformation", *Materials Science and Engineering A*, vol. 410-411, pp. 257–260, 2005.

[160] K. Todaka, M. Umemoto, and K. Tsuchiya, "Comparison of nanocrystalline surface layer in steels formed by air blast and ultrasonic shot peening", *Materials Transactions*, vol. 45, pp. 376–379, 2004.

[161] M.A. Meyers and K.K. Chawla, *Mechanical Metallurgy: Principles and Applications*. Prentice-Hall, Inc., 1984.

[162] E.W. Hart, "Theory of the tensile test", *Acta Metallurgica*, vol. 15, pp. 351–355, 1967.

[163] C.C. Koch, "Structural nanocrystalline materials: an overview", *Journal of Materials Science*, vol. 42, pp. 1403–1414, 2007.

[164] C.D. Beachem, "An electron fractographic study of the influence of plastic strain conditions upon ductile rupture processes in metals", *Transactions of ASM*, vol. 56, pp. 318–334, 1963.

[165] Z.F. Zhang and J. Eckert, "Unified tensile fracture criterion", *Physical Review Letters*, vol. 94, p. 09430194311, 2005.

[166] C. Fan and A. Inoue, "Ductility of bulk nanocrystalline composites and metallic glasses at room temperature", *Applied Physics Letters*, vol. 77, pp. 46–48, 2000.

[167] L.C. Zhang, B.C. Wei, D.M. Xing, T.H. Zhang, W.H. Li, and Y. Liu, "The characterization of plastic deformation in Ce-based bulk metallic glasses", *Intermetallics*, vol. 15, pp. 791–795, 2007.

[168] S.B. Biner, "Ductility of bulk metallic glasses and their composites with ductile reinforcement: A numerical study", *Acta Materialia*, vol. 54, pp. 139–1150, 2006.

[169] F. Szuecs, C.P. Kim, and W.L. Johnson, "Mechanical properties of $Zr_{56.2}Ti_{13.8}Nb_{5.0}Cu_{6.9}Ni_{5.6}Be_{12.5}$ ductile phase reinforced bulk metallic glass composite", *Acta Materialia*, vol. 49, pp. 1507–1513, 2001.

[170] X.H. Du, J.C. Huang, K.C. Hsieh, Y.H. Lai, H.M. Chen, J.S.C. Jang, and P.K. Liaw, "Two-glassy-phase bulk metallic glass with remarkable plasticity", *Applied Physics Letters*, vol. 91, p. 131901, 2007.

[171] W.J. Ma, Y.R. Wang, B.C. Wei, and Y.F. Sun, "Microstructure and mechanical properties of Zr-Cu-Al bulk metallic glasses", *Transactions of Nonferrous Metals Society of China*, vol. 17, pp. 929–933, 2007.

[172] N.K. Mukhopadhyay, A. Belger, P. Paufler, and D.H. Kim, "Nanoindentation studies on Cu-Ti-Zr-Ni-Si-Sn bulk metallic glasses", *Materials Science and Engineering A*, vol. 449-451, pp. 954–957, 2007.

[173] A.V.D. Beukel and J. Sietsma, "The Glass Transition as a Free Volume Related kinetic phenomenon", *Acta Metallurgica et Materialia*, vol. 38, pp. 383–389, 1990.

[174] K.M. Flores, D. Suh, P. Asoka-Kumar, P.A. Sterne, R.H. Howell, and R.H. Dauskardt, "Characterization of free volume in a bulk metallic glass using positron annihilation spectroscopy", *Journal of Materials Research*, vol. 17, pp. 1153–1161, 2002.

[175] Q.P. Cao, J.F. Li, Y.H. Zhou, A. Horsewell, and J.Z. Jiang, "Effect of rolling deformation on the microstructure of bulk $Cu_{60}Zr_{20}Ti_{20}$ metallic glass and its crystallization", *Acta Materialia*, vol. 54, pp. 4373–4383, 2006.

Publications

- J.W. Tian, J.C. Villegas, W. Yuan, et al , "A study of the effect of nanostructured surface layers on the fatigue behaviors of a C-2000 superalloy", Materials Science and Engineering: A, 468-470(11), 2007, pp.164-170
- J.W. Tian, K. Dai, J.C. Villegas, et al, "Tensile properties of a nickel-base alloy subjected to surface severe plastic deformation", Materials Science and Engineering: A, 493(1-2), 2008, pp.176-183
- J.W. Tian, L. Shaw, P.K. Liaw, K. Dai, "On the ductility of a surface severely plastically deformed nickel alloy", Materials Science and Engineering: A, 498(1-2), 2008, pp. 216-224
- J.W. Tian, L.L. Shaw, Y.D. Wang, et al, "A Study on the Surface-Severe-Plastic Deformation Behavior of a Zr-based Bulk-Metallic Glass (BMG)", (Submitted to Intermetallics)
- A.L. Ortiz, J.W. Tian, J.C. Villegas, et al, "Interrogation of the microstructure and residual stress of a nickel-base alloy subjected to surface severe plastic deformation" Acta Materialia, 56(3), 2008, pp. 413-426
- B. Winiarski, J.W. Tian, R.M. Langford, P.K. Liaw, P.J. Withers, "Residual-stress measurements of amorphous materials using a focused ion beam",(in preparation)

Vita

Jiawan Tian was born in Xiaogan, Hubei Province, China, on March 26, 1976, the son of Huilan Qiu and Chuanbiao Tian. After graduating in 1995 from Xiaogan No.1 high school, Hubei Province, he attended Shanghai Jiaotong University, Shanghai, China, where he received both a Bachelor of Science degree in 1999 and a Master of Science degree in 2002 from the department of materials science and engineering. In the spring of 2002, Jiawan entered Shanghai Belling Corp., ltd, a semiconductor manufacturing company, as a process engineer in Shanghai, China. In January 2004, he again returned to the academic world as a doctoral student at the University of Tennessee in materials science and engineering, where he worked as a graduate research assistant. During his PhD studies in materials science, Jiawan also finished the main courses in the department of statistics, and in 2008, he completed his Doctor of Philosophy degree in materials science and Master of Science degree in statistics.